DEVELOPMENT OF FRICTION STIR WELDING FOR AEROSPACE MANUFACTURING: DERIVATIVE PROCESSES AND NOVEL APPLICATIONS

by

Connor Strawn

Dissertation
Submitted to the Faculty of the
Graduate School of Vanderbilt University
in partial fulfillment of the requirements
for the degree of

DOCTOR OF PHILOSOPHY
in
Mechanical Engineering

May 12, 2023
Nashville, Tennessee

Committee:
Alvin Strauss, Ph.D.
Kenneth Frampton, Ph.D.
Kevin Galloway, Ph.D.
Kenneth Pence, Ph.D.
Thomas Withrow, Ph.D.

ACKNOWLEDGEMENTS

This dissertation would not have been possible without the support of many individuals and organizations. I would first like to thank Dr. Alvin Strauss for inviting me to join his lab and advising me during my time at Vanderbilt. Next, I would like to thank my committee members: Drs. Kenneth Frampton, Kevin Galloway, Kenneth Pence, and Thomas Withrow. Your guidance was invaluable as I navigated through the rigors of graduate school. I would also like to thank the NASA Tennessee Space Grant Consortium and Vanderbilt University for providing research funding.

My relationships with other students greatly enriched my time at Vanderbilt. The people I worked with directly in the Vanderbilt University Welding Automation Lab have been great colleagues and friends. I would like to thank Lucas Wilkins, Brayden Terry, Ben Snyder, Henry Gunner, Kelsay Neely, Adam Jarrell, Austen Shelton, Ben Firestone, Hayden Jenkins, Devany Sweitzer, Todd Evans, and Jeremy Trujillo. Thanks to you all, I will never forget what happened at 52º 7’ 0”, 0º 13’ 34” in December 1991. Other past and present Vanderbilt community members I would like to thank include Phil Davis, Mark Thelen, David Ziemnicki, Darren Tinker, Garrett Marshall, and Victoria Vest. All my Vanderbilt University colleagues have provided advice and support through my ups and downs in graduate school. You encouraged me to do my best while keeping me humble through ceaseless banter. I truly could not have done this without all of you.

Finally, I would like to thank my family. My mother, Debbie Strawn, has supported me every step of the way while supplying an endless amount of love. My sister, Kelly Strawn, has been a lifelong friend with whom I have shared incredible adventures and our fair share of mischief. My father and stepmother, Doug Strawn and Linda Strawn, have been there to provide an escape from the day-to-day with exciting travel and excellent food. Lastly, I would like to thank Hannah Black. You have been endlessly supportive through one of the most challenging periods of my life. You have pushed me to be my best while ensuring that I never forget my value.

TABLE OF CONTENTS

LIST OF TABLES

LIST OF FIGURES

NOMENCLATURE

List of Abbreviations

ALE	-	Arbitrary Lagrangian Eulerian
AS	-	Advancing side
BFSF	-	Butted friction stir forming
CEL	-	Coupled Eulerian Lagrangian
DT	-	Destructive testing
EDM	-	Electron discharge machining
EDS	-	Electron dispersive spectroscopy
FSD	-	Friction stir dovetailing
FSE	-	Friction stir extrusion
FSF	-	Friction stir forming
FSP	-	Friction stir processing
FSW	-	Friction stir welding
HAZ	-	Heat affected zone
NDT	-	Non-destructive testing
RS	-	Retreating side
SEM	-	Scanning electron microscope
SRFSW	-	Self-reacting friction stir welding
TMAZ	-	Thermomechanically affected zone
TWI	-	The Welding Institute

Symbols

$\vec{t}$	-	Tool position vector
θ	-	Tool tilt angle
$\vec{v}$	-	Tool velocity vector
$\dot{x}$	-	Tool velocity component in x direction
$\dot{y}$	-	Tool velocity component in y direction
θ_{eq}	-	Equivalent tilt angle
d	-	Tool offset
r	-	Radius of curved workpiece
q''_{rad}	-	Radiation heat flux
α_{sol}	-	Absorption coefficient for solar radiation
G_{sol}	-	Solar constant, $1362\, W/m^2$
ε	-	Emissivity
σ	-	Stefan-Boltzmann constant, $5.67 * 10^{-8}\, W/m^2K^4$
T_s	-	Surface temperature
T	-	Temperature
P	-	Power
τ	-	Tool torque
ω	-	Tool rotational speed
$\dot{E_{in}}$	-	Energy into the system
$\dot{E_g}$	-	Energy generated in the system
$\dot{E_{out}}$	-	Energy out of the system
$\dot{E_{st}}$	-	Energy stored in the system
Q	-	Energy
m	-	Mass
c_p	-	Specific heat capacity
t	-	Time
A_s	-	Surface area
T_i	-	Initial temperature

CHAPTER I:
INTRODUCTION

This dissertation contributes to the field of friction stir welding (FSW). FSW is a joining method spanning several industries, including aerospace, automotive, maritime, and rail. While FSW impacts all these fields, the scope of this dissertation focuses on using FSW and its derivative processes to advance aerospace manufacturing. Aerospace-focused FSW benefits include the ability to join unique material combinations, improve structural integrity, and reduce vehicle weight, all of which are discussed in more depth in this dissertation.

FSW shows significant potential as a joining methodology. While FSW is an application-proven aerospace technology, competition with well-established methods like conventional welding and fasteners limits the expansion of this technology. Advancement and greater utilization of aerospace FSW require further research and experimental validation. Potential novel applications of FSW in the aerospace industry motivated this work.

To put the dissertation results in context with the field, Chapter 2 presents a literature review. A better understanding of the FSW field shows the state-of-the-art and potential improvements. Chapter 3 provides a proof-of-concept for an aluminum-to-graphite friction stir extrusion (FSE) composite joint. Chapter 4 introduces the butted friction stir forming (BFSF) method, which joins two butted aluminum pieces to a lapped third workpiece. Chapter 5 describes the adaptation of BFSF to curved surfaces. Chapter 6 expands upon established FSW research for implementation to lunar applications. Finally, Chapter 7 concludes this dissertation.

Overview of Work

Chapter 3 of this dissertation discusses FSE and its potential applications in ablative aerospace vehicle shielding. FSE is a derivative FSW process that joins two workpieces through a mechanical interlock. Through this process, materials with significantly different properties are joinable. This research used FSE to join an aluminum alloy with graphite plates. Graphite selection for this work is due to its excellent chemical resistance, stable high-temperature behavior, and resistance to thermal shock. While ablative materials with better properties than graphite exist, graphite was a relatively inexpensive option to perform a first-order

approximation of FSE with brittle materials. Traditional joining methods for graphite to metal use brazing, fasteners, or adhesives. Each method has shortcomings, leading to metal-graphite FSE joining as an alternative. The results of this study validated metal-graphite FSE joints for low-load applications.

Chapter 4 proposes BFSF for joining aircraft exterior surfaces to structural members. BFSF is a novel process that joins two pieces of material in a traditional FSW butt weld while extruding a screw geometry into a tertiary workpiece. This work uses butted sections of aluminum alloy lapped over a steel plate with a preformed threaded hole. The FSW tool joins the workpieces as it traverses along the aluminum-aluminum seam. When the tool path crosses the threaded hole, the elevated material temperature and FSW tool pressure extrude aluminum into the screw hole like a forming die. Post-welding, thermal contraction of the formed screw applies a preload that keeps the aluminum pieces attached to the lapped steel. While butt welding and friction stir forming (FSF) of screw geometries are well studied individually, the combination is novel. This study showed a proof of concept for BFSF, a new FSW derivative process.

In Chapter 5, the BFSF method develops further. Previous BFSF work only discussed joining flat structures, but many aerospace vehicles have curved geometries such as those in wings or fuselages. To remedy this, optimization of tooling, operating parameters, and workpiece orientations allowed the successful joining of three workpieces through the BFSF process. Two aluminum alloy pipe sections were butted together and concentrically mated with an internal steel pipe. Threaded holes in the steel allowed joining with the aluminum pieces in one operation. This workpiece geometry approximates the small-radius curvatures present in an aerospace structure. The creation of successful joints shows that the BFSF process is valid for small radius, large radius, and flat workpieces.

The research in Chapter 6 investigates FSW as a potential lunar technology. FSW has no process consumables, is a solid-state process, and does not rely on an atmosphere, which supports it as an in-space manufacturing technology. These attributes make FSW a candidate for welding in lunar conditions, but there are practical concerns about the process's efficacy. Barriers to implementation include thermal management and the resulting material property changes. Through calculations, simulation, and experimentation, this work investigated the applicability of FSW in a lunar environment. Heat transfer calculations and simulations produced expected temperature trends for weld samples in a lunar environment. Since convective heat

transfer will be negligible on the moon, FSW workpieces will take much longer to cool than in a similar terrestrial environment. In experimentation, a temperature-controlled tube furnace allowed post-weld samples to cool at the calculated rate. Aluminum alloy samples were butt welded and immediately placed under simulated lunar heating conditions. This testing procedure showed the effects of prolonged cooling on FSW samples through mechanical testing and microscopy. The experimental results and lunar conditions literature review support FSW for lunar applications.

CHAPTER II:
LITERATURE REVIEW

Friction stir welding (FSW) is a solid-state joining process developed and patented by Thomas et al. in 1991 at The Welding Institute (TWI) [1]. Initial applications of the FSW process focused on joining aluminum alloys in a butted configuration [1] and have since expanded to a broad range of weldable materials and workpiece configurations. FSW can join metals, polymers, and composites, with the number of joinable materials continually growing through proof-of-concept and application-based research.

Applications of FSW span several industries, including aerospace, automotive, maritime, and rail. While extensive current uses and future applications exist, a few notable examples stand out. Aerospace applications of FSW include rocket fuel tanks [2–4], aircraft [5,6], and potentially in-space manufacturing [7]. The automotive industry uses FSW to assemble car bodies [8,9] and fabricate engine parts [8]. Maritime uses of FSW include superstructure fabrication in shipbuilding [6,8]. The rail industry employs FSW for locomotives, freight cars, and passenger cars [8].

Process Overview

FSW relies on a rotating tool to generate frictional heat and material stirring. The tool's rapid rotations generate heat through friction and plastic deformation, causing the material to soften [10]. Tool motion causes the material to flow around the tool, which allows the material to mix and reconsolidate along the tool path. Stirring continues as the tool traverses along the weld path. The stirred material reconsolidates on the tool path to create a weld between the workpieces. The heated and softened material does not exceed its solidus temperature, remaining solid throughout the process. Since the process does not melt the material, the joints are stronger than a comparable fusion-welded joint by, on average, 30% [6]. Figure 1 shows a diagram of the FSW process.

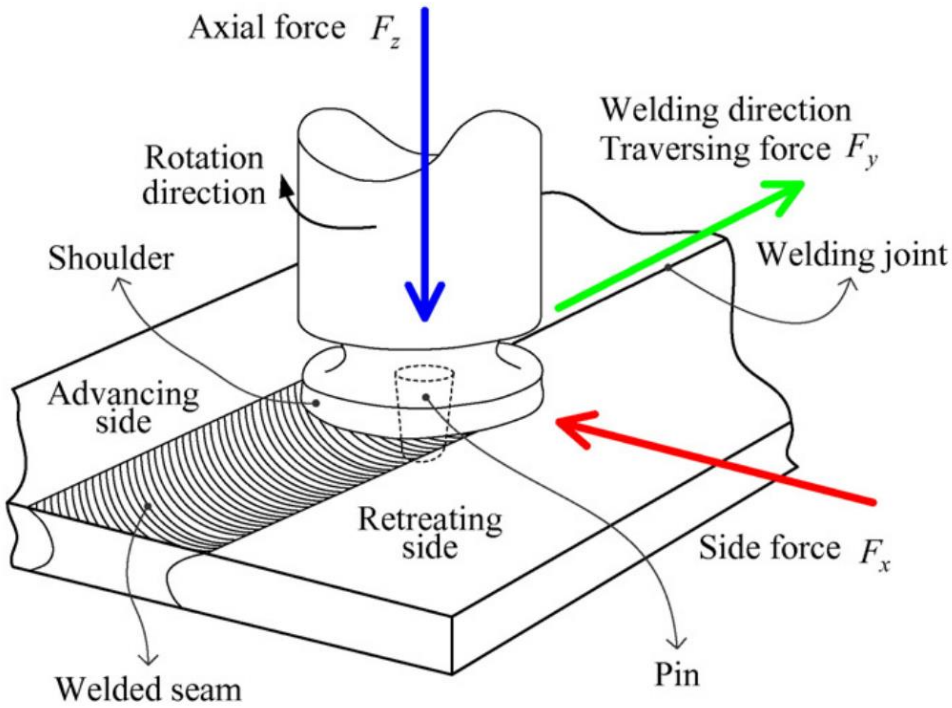

Figure 1. Friction stir welding (FSW) diagram. Adapted from [8].

There are several common weld configurations performed in traditional FSW. These include butt welds, lap welds, and T-joints [11]. The type of weld depends on the application, workpiece dimensions, part design, and material. Figure 2 shows typical welds for each joint configuration.

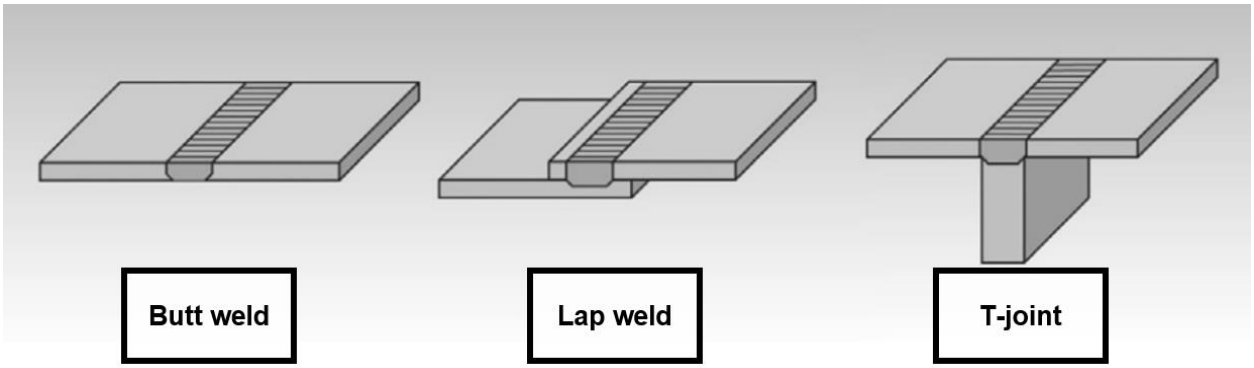

Figure 2. FSW workpiece configurations. Adapted from [6].

Machines used in FSW literature fall into three categories [8]. The first type of welder involves the modification of existing machining equipment, such as the conversion of a milling machine. This type of machine is suited for research or low-volume production [8]. The second type of welding equipment is either custom-built or dedicated machinery for FSW, such as units designed for specific structures or commercially available FSW machines [8]. The third classification of FSW equipment encompasses industrial robotic welders. Robotic FSW can meet high production volumes but often requires advanced control systems to account for manipulator arm joint deflection due to high FSW loading [8].

Material Properties

The joining process creates several unique zones in the workpiece with distinct material properties. Four distinct microstructural zones are used in FSW literature [12]: the parent material, the heat affected zone (HAZ), the thermomechanically affected zone (TMAZ), and the nugget. Figure 3 shows a diagram of zone location and descriptions with respect to the weld path.

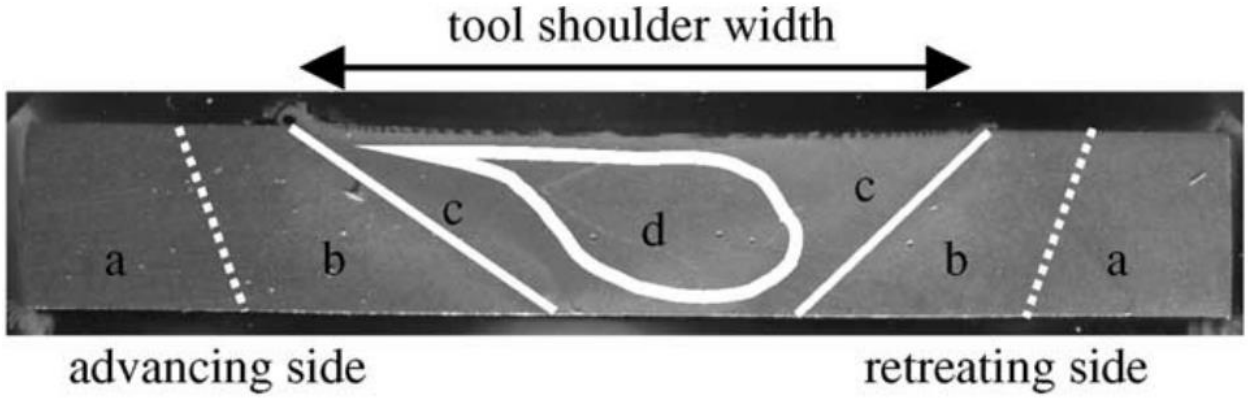

Figure 3. FSW sample cross-section with zones labeled. Advancing side and retreating side reference the tool's direction of rotation. a) Parent material. b) Heat affected zone. c) Thermomechanically affected zone. d) Nugget. Adapted from [13].

The parent material (also called the base material or virgin material) is unchanged by the FSW process. Workpiece parent material is far enough away from the weld zone that no material property changes occur due to thermal or mechanical interactions with the FSW tool. Since the

parent material properties are unchanged, it is the strongest region of the weld. Next to the base material is the HAZ, which experiences microstructural changes due to FSW heating but is not mechanically deformed. The parent material-HAZ boundary depends on the material used. For example, the boundary for heat-treatable aluminum alloys is located where the material is maintained above 250 ºC [14]. Welding parameters and tooling geometry affect heat input and material interaction, which influences the size and shape of each zone. The grain structure of the HAZ is the same as the parent material, but the thermal cycling affects alloying element precipitates [15]. The HAZ experiences coarsening of precipitates, which contributes to it being the weakest zone in an FSW joint. When mechanically tested, most sample strain occurs in the HAZ at over double what is experienced in the nugget zone [15]. The HAZ ductility leads to necking and fracture. Weld failures are most likely to occur within the HAZ or along the HAZ/TMAZ boundary, but this depends on the material [10].

The TMAZ and the nugget make up the weld stir zone where extreme plastic deformation occurs. The strain and high temperatures in the TMAZ lead to a change in grain boundaries, but the strain and temperature contributions are not significant enough to cause complete recrystallization [16]. Within the TMAZ, the degree of grain deformation depends on proximity and interaction with the tool. The grains generally become smaller the more they are deformed. The thermal and mechanical effects of the FSW process are most extreme towards the interior of the TMAZ where the material completely recrystallizes. This region is called the nugget [6]. The nugget is also called the dynamically recrystallized zone [12].

Additional complexity in weld zone definition is introduced by the inherent asymmetry caused by the unidirectional rotation of the tool [15]. The side of the tool that has a tangential velocity parallel to the tool's traversal movement has a relatively faster tool movement than the other side of the tool due to the additive nature of the tangential velocity and the traversal velocity. This side of the tool is called the advancing side (AS). The higher velocity leads to increased frictional heat generation on this side of the tool. The other side of the tool, called the retreating side (RS), has a subtractive effect relationship between the tool's tangential velocity and traversal velocity [15].

Tool Design

An FSW machine uses a metal and/or ceramic tool to heat and plastically deform workpiece materials [17]. As a broad, general description, FSW tools are rotating cylinders with features on the workpiece-contacting side to encourage optimal weld quality. Figure 4 shows a typical FSW tool. The types of metal and the features used on the tool vary significantly depending on the application and joint materials. Tools are considered non-consumable except when joining particularly abrasive materials [18,19].

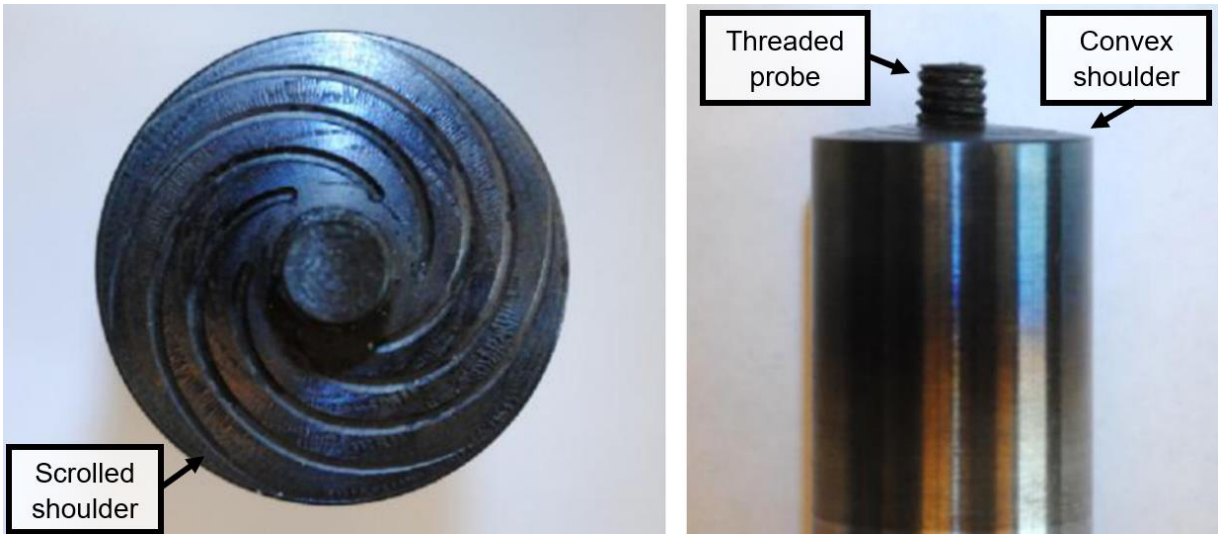

Figure 4. Typical FSW tool with a scrolled, convex shoulder and a threaded probe. Adapted from [6].

Tool design adjusts the dimensions and geometries of two main features: the tool shoulder and the tool probe. The shoulder is the bottom face of the tool that contacts the top surface of the workpiece, and ranges in diameter from 10 mm to 32 mm [20]. Friction from the tool shoulder generates most of the heat in FSW [21]. Additionally, the shoulder shape affects the forces applied and the direction of its resultant in the FSW process. Shoulders can be concave, convex, or flat. Concave tool geometries consolidate the material inward while forcing it into the workpiece [2]. Convex tools generally produce less flash and defects than concave shoulders [22]. Flat tools are less common and cause weld conditions different than concave and convex tooling [23]. Generally, flat tools produce lower strengths than a comparable joint with a concave or convex tool [24]. Shoulder surface features are compatible with concave, convex, or

flat tools. These features encourage material flow. Shoulder features include scrolls, knurling, ridges, grooves, and concentric circles [25]. The most common surface features are scrolls, which are grooves that spiral from the tool edge to the probe. Figure 4 shows shoulder scrolls on a typical FSW tool.

The shoulder provides significant heat contribution in FSW while the tool probe improves material mixing and reduces internal defects. Tool probe design depends on the workpiece material and size. Potential probe shapes include threaded and unthreaded cylinders, rectangular or triangular prisms, and frustums (pyramidal and conical) [22]. Many combinations and variations of these geometries are employed depending on the desired material deformation and reconsolidation behavior. Depending on the application and material size, welders can also use tools either without a shoulder (probe only) [26] or without a probe (shoulder only) [27].

FSW tool material is also an important consideration. For use in aluminum alloys and polymers, hardened tool steel is adequate [28]. FSW with harder materials, such as steel alloys or titanium alloys, requires tools that endure high temperatures while maintaining sufficient mechanical strength. High-temperature tool materials are generally tungsten-based. Commonly used tungsten alloy FSW tools include tungsten carbide, tungsten rhenium, tungsten lanthanum, and tungsten tantalum [3].

Operating Parameters

For successful FSW, several separate process parameters need precise calibration. The main parameters are tool rotation speed (RPM), welding speed (mm/min or in/min), plunge depth (mm or in), tilt angle, and sideways angle [12]. These parameters determine tool engagement, heat generation, and material deformation. Parameters are highly variable when considering different materials, tooling geometry, joint configurations, and workpiece thickness.

The welding environment can adjust to affect operating parameters. For example, the temperature of workpieces during welding is a key consideration. Welded material can get hotter than desired or not cool at a desired rate, in which case in-process cooling would be beneficial [29]. Similarly, the material may not reach the desired temperature through welding, requiring additional heating to improve weld quality [30]. Workpiece thermal management and system parameters can be static throughout the welding process or adjusted based on control systems monitoring in-process feedback.

In-process Controls

An FSW control system allows for fewer defects, higher joint strength, and improved joint path tracking that is difficult to achieve in an open-loop system. Feedback measurements vary depending on the instrumentation the specific welding equipment uses. The most common feedback sources include position control, weld speed control, tool force, and tool torque. These signals allow the controller to update system parameters, such as tool rotation speed, weld speed, and tool penetration, to improve the weld quality. A proper FSW control system can detect and correct potential defects in the joint.

Position and Weld Speed Control

Position and weld speed control systems are the most straightforward FSW control schemes. The systems can operate with or without feedback, and the position instrumentation is likely already present in the FSW machine. Knowing the position and the time elapsed allows for speed control. The simplicity of position weld speed control makes it attractive in research settings [9]. However, this control scheme does have limitations when not used with another control method. Position and speed control does not account for and correct for weld quality, meaning that the parameters need to be verified empirically to ensure adequate weld quality.

Force and Torque Control

In contrast to position and weld speed control, force-controlled systems have improved weld quality and are more robust [31]. By maintaining the correct position and keeping a constant axial force, force control reduces the likelihood of weld flaws [32]. Force and torque monitoring during FSW can use a dynamometer on the tool spindle or calculations converting motor current to torque [33].

Using torque as a feedback signal is the natural next step to force control. Torque provides a more accurate indication of tool plunge depth than force, making torque invaluable when maintaining tool engagement [32]. Longhurst et al. developed a control system using torque control of plunge depth [32]. They concluded that torque control allows the adjustment of more process variables than force control, including plunge depth, rotation speed, and traverse speed.

In a study by Gibson et al., torque control accounted for changes in tool behavior due to FSW tool wear [34]. FSW tools are generally considered non-consumable, but welding hard or abrasive materials like metal matrix composites can wear a tool down relatively quickly [35]. A change in tool geometry, such as the tool pin losing its threading, can affect weld quality. Torque control enabled in-process adjustments for tool changes.

Force and torque control can be combined, as was done by Fleming et al. [36]. They used these two signals to track a seam during the welding process. The tool weaved back and forth while measuring the force and torque signals. Proximity to the weld seam produced unique feedback that matched known values for proper alignment.

Alternative Control Schemes

Unique feedback measurement techniques are also possible. For example, some instrumentation measures magnetic or electrical properties to predict weld quality. Comparing the measurements to known successful welds allows for the adjustment of system parameters [37]. Other potential feedback signals could come from the material temperature, which indicates the temperature-dependent material properties. By measuring this, the tool's traverse rate or rotation speed adjust accordingly to optimize weld quality [30,38].

Weld Analysis

Post completion of a friction stir weld, joint analysis assesses weld quality. FSW research and industry development use several destructive and non-destructive testing methods (DT and NDT, respectively). Various testing methods show the joint integrity and the material properties of samples, which is essential to determine if the resultant joints are viable for the intended application. The tests used in FSW sample evaluation are broad, but most testing aims to determine material properties, mechanical strength, and defect formation.

Material property determination of samples often uses microscopy. Electron microscopy of FSW samples highlight material flow and element distribution. Images show the degree of mixing and occurrence of heating effects. By using electron dispersive spectroscopy (EDS), information on precipitates can be obtained. As previously discussed, the FSW process will cause changes in precipitates and material properties.

Mechanical testing allows the determination of the strength of samples and the corresponding joint efficiencies. Methods such as tensile testing, hardness testing, and bending tests show how the welding process has changed the material properties of the parent material. Property identification allows for more accurate comparisons of FSW to competing technologies.

Defect formation in FSW creates potential failure initiation points in the weld zone. When developing new welding configurations, tools, and materials, defects are even more likely to exist. Some FSW defects form on the top or bottom of the workpiece surface, making their identification easier. Common surface-level defects include excess material flashing [39], surface voids [12], and root flaws [40]. Internal to the weld, there can be voids/wormholes [39]. These volumetric flaws are difficult to detect without imaging a sample cross-section [12].

Derivative Processes

FSW is a derivative of the broader field of friction welding. Through development of application-specific processes, FSW further derives into several other technologies. This section highlights the most impactful derivative processes.

The processes with the most similarities to traditional FSW are friction stir spot welding (FSSW) and self-reacting FSW (SRFSW) [6]. These methods still use the basic theory of FSW but have slight modifications to tool trajectory, tool design, and weld configuration. FSSW does not have a weld path but instead has a single contact patch to join workpieces [41]. This process can either use a single tool or be fixtured to contact the workpiece from both sides [42].

SRFSW uses a bobbin tool that contacts both sides of the weld surface [43], as shown in Figure 5. The goal of this derivative process is to reduce the force requirements and rigidity of the FSW equipment by having the resultant force from the welding process reduced through the self-reacting nature of the tooling [44].

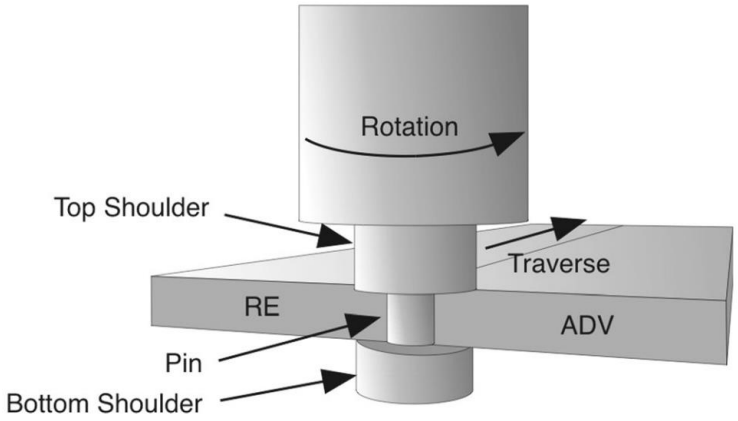

Figure 5. Self-reacting friction stir welding (SRFSW) bobbin-tool. Adapted from [44].

Friction stir processing (FSP) uses the traditional FSW process to refine material properties or incorporate a filler substance into the workpiece substrate [45]. Microstructural changes from FSP enable adjustment of localized material properties, such as creating high-strain rate superplasticity regions in a workpiece [15]. FSP can embed particles into a substrate from powders [46] or colloids [47].

The plastic deformation in FSW extends beyond the weld zone. Several derivative processes use the deformation and forces of FSW to extrude material, as shown in Figure 6. Friction stir forming (FSF) [48] and friction stir extrusion (FSE) [49] operate with similar mechanisms, where the welded material extrudes into a preformed geometry. The formed extrusions create a mechanical joint. Friction stir dovetailing (FSD) is similar; however, the interaction of a tungsten carbide tool insert creates metallurgical bonding at the interface between the material with the preformed geometry and the material being welded [50]. The benefit of these three processes is the ability to join dissimilar materials while only penetrating one of the workpieces, generally the material more suited for FSW. Tool wear and power requirements reduce due to working with a readily weldable material.

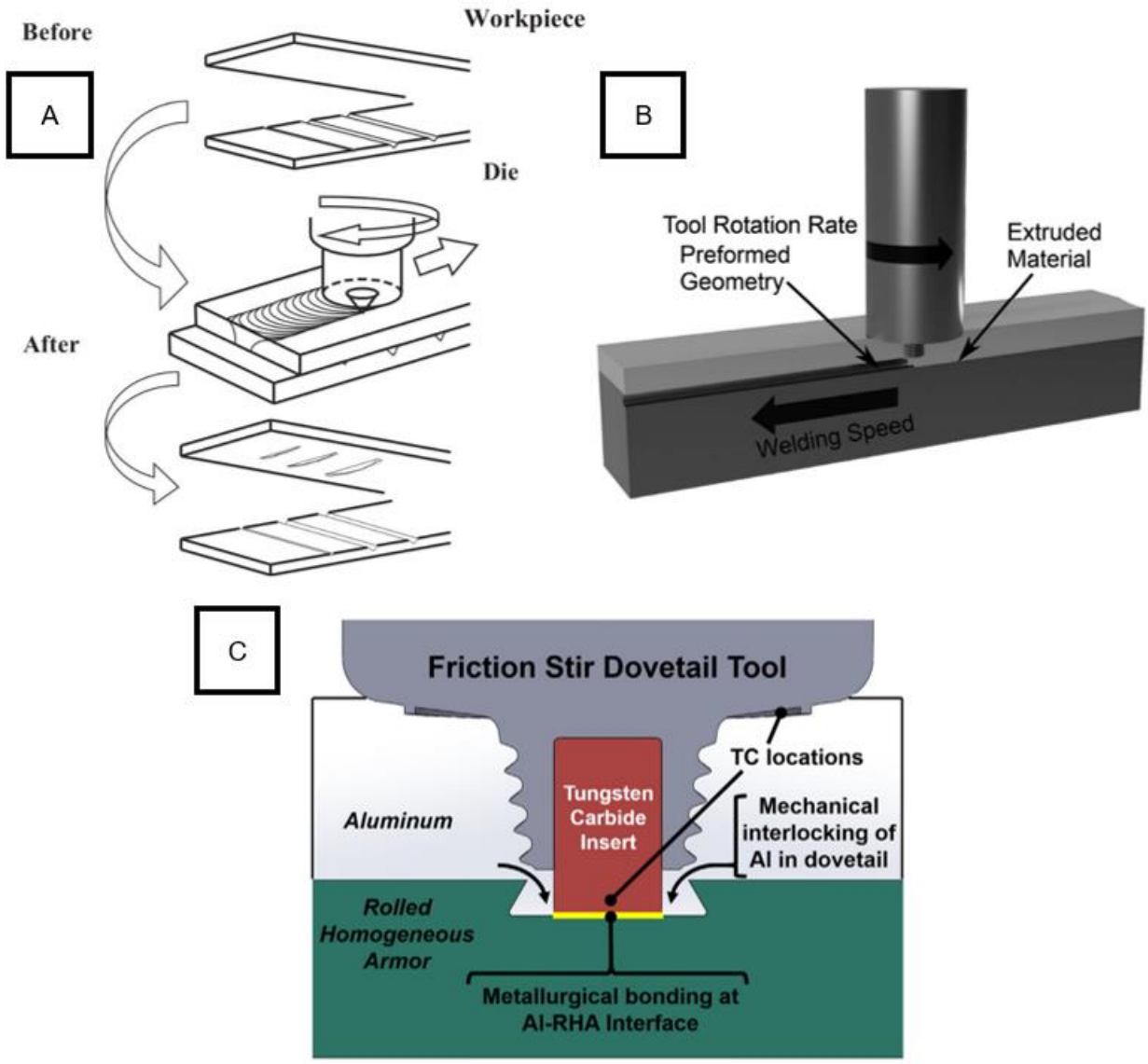

Figure 6. FSW derivative processes. A: Friction stir forming (FSF) [51]. B: Friction stir extrusion (FSE) [52]. C: Friction stir dovetailing (FSD) [50].

Modeling and Simulation

Modeling and simulation of FSW highlight the complexity inherent to the welding process. The temperature gradients and extreme plastic deformation cause material properties such as yield stress, thermal conductivity, and heat capacity to vary across the weld zone [53]. The property variations affect the amount of tool-induced deformation and frictional heating [53]. FSW interdependencies of individual components mean that an accurate model must couple

thermal and mechanical effects. The material used in FSW remains solid for the entire welding process, but the severe plastic deformation and the material flow behavior more closely match a fluid. As such, the material in FSW is generally modeled as a non-Newtonian fluid with viscoplastic properties [53–55].

FSW modeling employs Eulerian and Lagrangian methods to account for the multi-physics nature of the process [54]. The Eulerian method models a control volume of particles and their concentration within that volume [56,57]. Lagrangian methods capture discrete particles and are more interested in their trajectory than a control volume [56,57]. For context with FSW, the Eulerian domain captures material movement within the workpiece, while the Lagrangian domain models discrete material element interaction with the tool [54]. One formulation for the combination of Eulerian and Lagrangian methods is called the Arbitrary Lagrangian Eulerian (ALE) approach [58]. This model remeshes the workpiece to account for the mesh distortion caused by plastic deformation. However, one shortcoming of the ALE approach is its inability to simulate material void defects [59].

A method that improves on the ALE approach is the Coupled Eulerian Lagrangian (CEL) [59]. CEL captures the FSW mechanical and thermal interactions while modeling defects formed during the simulations [59]. This method couples Eulerian and Lagrangian interactions with a contact condition between the two meshes [59]. Additionally, this method uses a secondary Eulerian region above the workpiece to measure any material displaced through flashing.

Modeling and simulation of FSW are beneficial in several ways. Modeling the process enables a greater understanding of the occurring physical interactions [60], which predicts weld flaws and material properties. Additionally, modeling quantifies tool-workpiece interactions, such as which tool features and surfaces contribute the most to heating or material deformation [53]. Modeling tool designs and the resulting weld quality allows for an improved tool design workflow over a mainly empirical approach.

Comparison to Competing Technologies

FSW needs validation of its improvements and benefits compared to competing technologies for industry adoption. In metal joining applications, the main competitors with this process are fusion welding and fasteners. These competing processes are well-established in

industry, requiring FSW to present a marked improvement over them. While FSW does have shortcomings, its benefits show it to be a valuable alternative to other methods.

While fusion welding has had a long and successful history in manufacturing, it is not without flaws. The melting and resolidification in fusion welding lead to residual stress buildup and workpiece distortion [61]. Solidification cracking and porosity defects can also be present. When compared to fusion welding, FSW has several advantages. FSW enables dissimilar material joining that is difficult or impossible with fusion welding techniques. In a fusion welded joint, dissimilar materials will likely experience metallurgical and thermal expansion differences that cause joint defects. Since FSW operates at a lower temperature and does not rely on metallurgical bonding, dissimilar welding with FSW is easier and more successful [15]. The joints formed through FSW are often stronger in static and fatigue loadings than their fusion welded counterparts due to more favorable heating conditions and the lack of melting [61]. Without the high temperatures and material melting of fusion welding, oxidation and hydrogen embrittlement are not significant. Due to this, FSW does not generally require shielding gas [15]. The lack of shielding gas, the use of non-consumable tools, and the inherently lower energy requirement of FSW make it a more sustainable process than fusion welding [61]. Compared to a laser welding joint, an FSW joint of the same size only used 2.5% of the energy [15].

Fasteners are the other main competitor with FSW. The most applicable fastener is the rivet. In applications such as aerospace or automotive, rivets enable the joining of lapped materials efficiently, but FSW provides notable advantages. FSW is up to six times faster than automated riveting and up to 60 times faster than manual riveting [5]. Additionally, an FSW joint is stronger than a single row of rivets [5]. Without using these fasteners, there is a weight reduction. Designs can reduce the size of mounting flanges or remove them entirely.

As with any technology, FSW is not without drawbacks. Due to the high forces experienced during joining, FSW equipment is generally quite large compared to a fusion welding setup of similar capability [61]. Equipment size and the workholding requirements make manufacturing implementation of FSW have a higher upfront cost than comparable technologies. Even considering the shortcomings of FSW, the potential weight reduction, material property improvements, energy efficiency, and demonstrated versatility of the process has motivated a significant body of research and potential applications.

CHAPTER III:
FRICTION STIR EXTRUSION OF ALUMINUM AA6061 INTO ISOSTATICALLY MOLDED GRAPHITE

Connor Strawn, Alvin M. Strauss

This chapter is published in the *Journal of Manufacturing Processes* as:

C. Strawn, A.M. Strauss, Friction stir extrusion of aluminum AA6061 into isostatically molded graphite, J. Manuf. Process. 69 (2021) 391–397. https://doi.org/10.1016/j.jmapro.2021.07.052.

Abstract

This work investigates existing metal-graphite joining methods with friction stir extrusion (FSE) proposed as a viable alternative joining process. Current joining methods for these materials, including adhesives, mechanical fastening, and brazing, all have shortcomings that are desired to be avoided. Aluminum AA6061-T6 is used with isostatically molded graphite to establish a proof-of-concept for metal-graphite FSE. Empirically determined operating conditions were established that reduced force spikes, vibration, and FSE flaws while preventing significant defects in the final product. Successful metal-graphite FSE joints were created and tested in lap shear compression loading. A comparison of the FSE joint strength to the strength of brazed joints is presented. Metal-graphite FSE is concluded as a viable joining technique in low-load applications. Process optimization for future work and methods of joint strength enhancement are discussed.

Introduction

Expansion into harsh environments, like the inside of nuclear reactors or outer space, requires materials with unique properties. One such material is graphite, which has a low thermal expansion, resistance to thermal shock, high compressive strength, high corrosion resistance, and the ability to absorb free neutrons. While graphite exhibits high compressive strength, it has low tensile strength and is brittle. Improved mechanical performance of this material could lead to wider adaptation. To augment graphite's mechanical properties, it is often employed in a composite.

Graphite composites come in several forms. Graphite can be in a matrix with other materials, such as a metal matrix composite [47,62], a ceramic matrix composite [62,63], or a polymer matrix composite [64,65]. Melt infiltration, powder processing, and polymer carbonization (among other techniques) are all compositing methods currently employed. Instead of a matrix, graphite sections can be layered with other materials. Multi-layer graphite composites are of particular interest for this research. Layering premanufactured materials such as bulk graphite and aluminum alloys allow for simplified joining compared to matrix formation. Bulk graphite is generally easier to machine and join as it is not abrasive like many matrix composites, particularly ones that include ceramics. Graphite also does not raise concerns of fiber pullout from milling. On a more practical note, graphite is generally cheaper and more readily available than advanced material composites. Due to these factors, a multi-layer graphite composite is best suited for this proof-of-concept research in metal-graphite joining.

Existing techniques to create metal-graphite joints with molded graphite sections include adhesives, mechanical fastening, and brazing. The porous nature of graphite allows a liquid adhesive to penetrate the surface to create a graphite-graphite joint demonstrated by Wang et al. [66]. When used in a metal-graphite joint, adhesives face issues with binder wetting, mechanical strength, and thermal properties. Pramanik et al. used mechanical fastening, specifically bolts and rivets, to join graphite materials to aluminum alloys [64]. They also used adhesives with mechanical fastening to create hybrid joints. This hybridization allowed for stronger joints than the individual methodologies but adding adhesive and fasteners can increase weight, expense, defects, and complexity of the assembly. Additionally, fasteners to graphite necessitate pre-existing holes in the workpieces, leading to an increase in stress concentrations and spalling.

When adhesives and mechanical fasteners are not appropriate for the intended application, brazing is often used.

Brazing is the most common method of joining graphite to metal [7-18]. The vastly different material properties, including thermal expansion mismatch and wettability with molten metals, require an active metal like titanium in the brazing filler alloy [68]. Active metals tend to react with graphite, causing carbide layers to form that readily braze to metals. Brazing methods vary, from preformed carbide layers on the graphite to laser brazing.

Even though brazing is a widely accepted method of joining metal and graphite, there are notable shortcomings of the process. Graphite has a low coefficient of thermal expansion when compared to common metals like aluminum and copper. High brazing temperatures cause material expansion, which is problematic after bonding occurs and the joint cools causing the material to contract. Residual stress is present, as was shown by Mao et al. with their copper-graphite joint [75]. These residual stresses can be reduced by using materials with coefficients of thermal expansion similar to graphite, such as molybdenum [72] and tungsten [71]. An additional concern during the brazing process is that graphite can burn in standard atmospheric conditions at temperatures as low as 500°C [79]. Oxidation concerns led to graphite brazing occurring in vacuum conditions as used by Ray et al. [68] or in an inert atmosphere like the argon gas used by Pattee et al. [72]. Creating a vacuum or using a shielding gas adds additional complexity and cost to the brazing process.

Shortcomings of existing joining methods have led to research into alternative joining technologies. This research proposes such a method: friction stir extrusion (FSE). FSE is a derivative process of friction stir welding (FSW) used to create mechanical joints between dissimilar materials. The mixing of separate workpieces and metallurgical bonding in traditional FSW is avoided as FSE plastically deforms one workpiece into a pre-cut groove of another, thereby forming a mechanical joint with minimal intermetallic compounds. Groove cross-sectional geometries in FSE can vary. Dovetails are often used due to ease of manufacturing and FSE effectiveness demonstrated by Evans et al. [49] and Snyder and Strauss [29]. FSE only requires tool contact with one material. This is advantageous when considering materials that are more difficult to join with traditional FSW and/or are abrasive. These materials can lead to significant FSW tool wear as shown in work by Prater [4]. The FSE process is shown in Figure 7.

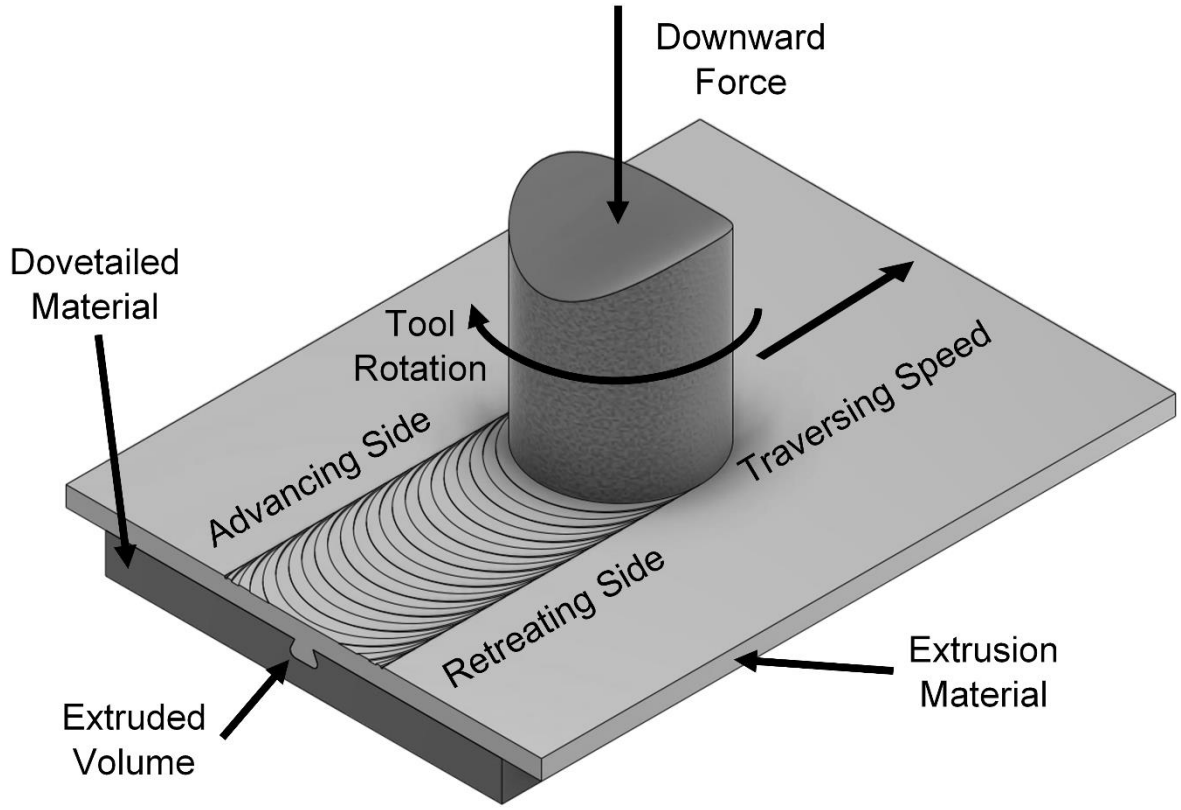

Figure 7. Friction stir extrusion process.

The FSE process can be applied to create a metal-graphite joint. FSE offers several improvements over existing joining methods. Unlike adhesives, FSE does not rely on a surface-level chemical or mechanical bond between graphite and metal. FSE also does not require the added assembly weight that is introduced by mechanical fasteners. Perhaps the greatest advantages are seen when comparing FSE to brazing.

The need for a vacuum chamber or shielding gas is negated when using FSE in place of brazing. With aluminum alloys, FSE temperatures stay below the oxidation point of graphite. FSE and FSW both exhibit improvements when compared to high-temperature joining techniques like brazing [6,15]. Notable benefits include low distortion due to heat, little to no surface preparation required, and savings in consumables such as filler metals and gas. These advantages could allow metal-graphite FSE to create a joint comparable to existing methods with higher mechanical strength, lower weight, increased manufacturability, better thermal properties, and more resilient chemical properties.

While metal-graphite FSE presents advantages, the process also has potential joint difficulties. Weak van der Waals forces, which contribute to graphite's excellent tribological properties, also allow the material to fracture depending on the material's crystalline plane orientation with respect to the loading direction [80]. Forces in FSE reach thousands of Newtons depending on the process parameters. In isolation, this force is not enough to break the graphite, but vibrations, cyclical loading, and flexure during the process can all contribute to material failure. The characteristics of the FSE process must be tuned to allow for a successful joint. Optimizing the process is difficult due to the coupled nature of parameters in FSE that is not yet fully understood.

Once metal-graphite FSE is optimized, beneficial material characteristics suggest that metal-graphite FSE can find applications in several fields. For instance, graphite is frequently used in the construction of rocket nozzles, such as the ones studied by Acharya and Kuo [81]. These types of nozzles are often joined to the rocket body with a gasket or a lap joint flange retainer, and FSE could be an alternative joining method. A circumferential FSE path around the rocket body could allow material extrusion into a grooved nozzle, thereby creating a mechanical joint between the two workpieces. A metal-graphite joint application in the nuclear field is thermal management in the first wall of nuclear fusion reactors. Tabares and Perlado [73] discuss a multilayer brazing technique for joining graphite to stainless steel as a plasma-facing material. FSE could be better suited for this application than brazing due to the above reasons. Joints such as these showcase graphite's properties while shielding structural materials. The FSE process could also improve electrical components. The high electrical conductivity of graphite enables use in a variety of applications such as electrical discharge machining (EDM) electrodes. Graphite is a common material used for EDM electrodes, however, FSE could allow for improved function and an increase in manufacturability. One structural use for graphite is sliding bearing plates. Countersunk screws are often employed, but they could be replaced with FSE. Bearing plates assembled with FSE could see improved function due to the absence of fastener holes.

This list of applications only highlights a select few uses of metal-graphite FSE. The potential applications are numerous and span several fields, making it impractical to develop a list of every application. Applications of metal-graphite FSE as well as the improvements it offers over current joining methods suggest that the technology is valuable. This work aims to

develop a novel metal-graphite joining technique that maintains the beneficial properties of its constituents while also discussing how to mitigate potential difficulties associated with graphite.

Materials and Methods

Materials

Machined plates of isostatically molded grade GM-10 (Graphtek LLC) graphite were used in this work. The chosen grade had high compressive strength, isotropic properties, and a fine grain structure. The plates' dimensions were 6.35 mm (0.25 inches) thick, 63.5 mm (2.5 inches) wide, and 101.6 mm (4 inches) long. The dimensions allowed for adequate workholding and a weld length sufficient to isolate tool plunge and retraction from the process data. The plate had a 2.54 mm (0.1 inches) deep dovetail groove in the longitudinal direction. Dovetail dimensions were chosen to match previous work done by Evans et al. [49]. A graphite sample used is shown in Figure 8.

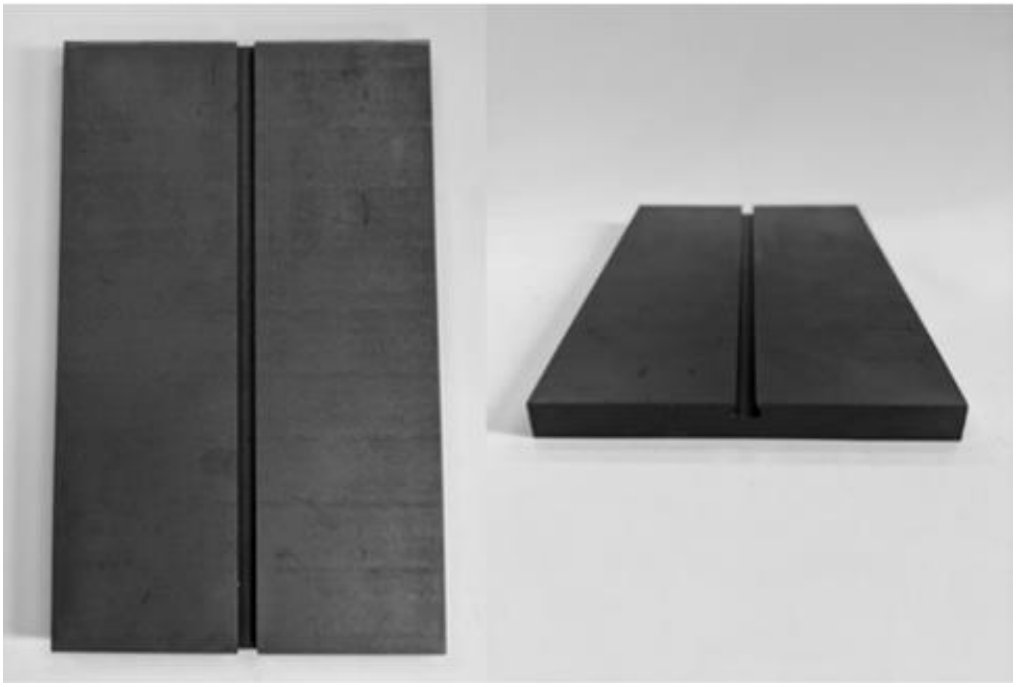

Figure 8. Graphite plate.

This study used aluminum AA6061-T6 for extrusion. While most graphite applications require materials with low coefficients of thermal expansion, aluminum AA6061-T6 was chosen

due to being well documented in FSW and FSE. Additionally, this medium strength grade is commonly used in making lightweight structures, making it a valuable proof-of-concept material [82].

Facility and Apparatus

FSE for this project was performed with a modified 1944 Kearney & Trecker Model K Mill. The mill was altered for fully automated operation. Cartesian position, cartesian forces, and torque about the tool's axis of rotation were recorded during operation by auxiliary instrumentation. A Kistler 9123C piezoelectric dynamometer measured forces and torque. Optical encoders, linear encoders, and string potentiometers determined position. MATLAB, Simulink, and C# code were used in the machine's operation, allowing full customization of the control systems. An open-loop speed controller was used in this work.

FSE Parameters

Due to the highly coupled nature of process parameters and difficulties with metal-graphite FSE, extensive testing had to be performed to produce a repeatable, successful joint. Tooling, fixturing, and operating conditions were iteratively improved to determine an optimal setup. Initial parameters were based on previous work in the Vanderbilt University Welding Automation Lab's FSE research by Evans et al. [49].

The first aluminum-graphite extrusion used a 6.35 mm (0.25 inches) thick aluminum AA6061-T6 plate that was extruded into graphite. A scrolled, convex shoulder FSW tool with a threaded pin was used. Using these parameters and tooling, FSE produced an aluminum extrusion into the graphite, as shown in Figure 9. The dovetail edge on the advancing side (AS) was broken and pushed into the dovetail while the retreating side (RS) remained mostly intact. Additionally, the bottom surface of the graphite was cracked. Despite the cracking, the workpieces remained attached upon removal of the samples from the clamping configuration and during subsequent sample preparation.

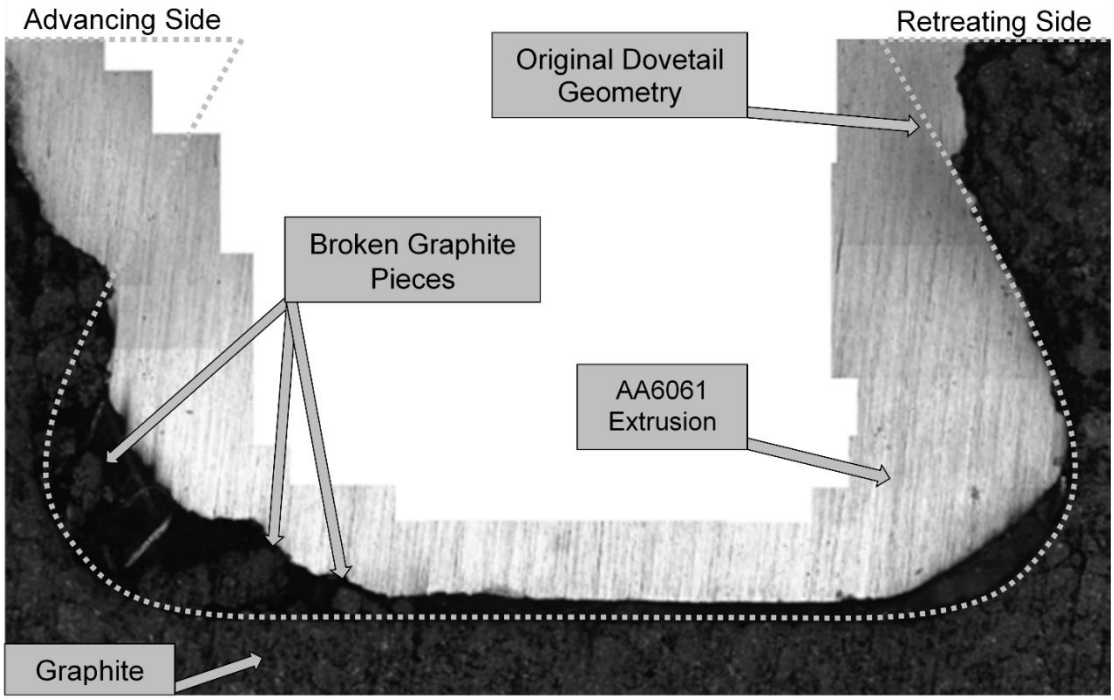

Figure 9. Initial extrusion optical microscope (5x magnification) image composite of aluminum extrusion in graphite

The first metal-graphite extrusion highlighted several key areas of potential process improvement. A crack spanning the length of the graphite propagated along the bottom of the dovetail, with cracking being the worst directly under the FSE tool plunge location. Cracking was assumed to be from the z-force peak observed during the FSE tool plunge. To reduce a pressure spike from the FSE tool pin, a pinless tool was used instead. It was hypothesized that the plunging forces would be applied more gradually due to the lack of a pin. The pinless tool required a thinner aluminum plate, so a 3.18 mm (0.125 inches) thick plate of the same grade of aluminum was used. Additionally, lead-on and lead-off tabs were employed to avoid tool plunge directly above the graphite. The tabs are grooved to allow extrusion and reduce in-process forces.

To better understand the in-process forces and subsequent cracking, a study was done with different FSE parameters to measure the produced z-forces. The testing apparatus was a steel plate with an adjustable-width square groove set to 3.18 mm (0.125 inches), the same width as the dovetail groove. The fixture's groove had a sufficient depth that the extrusion would not contact the bottom. Operating parameters were changed between trials. Traversing speed, RPM,

and plunge depth were the experimental variables. Under the chosen parameters, as plunge depth increased, so does the extruded volume and z-forces.

The volume of aluminum extrusion was critical as attempting to extrude too much material could have caused a large load inside the dovetail groove, potentially leading to cracking. Too little extrusion negatively affects joint strength due to an incomplete mechanical interlock. The dovetail cross-sectional area was approximately 9.7 mm^2 (0.015 in^2). After FSE on the test fixture, the aluminum extrusion cross-sectional area was approximated. Experimentation led to the tuning of process parameters to ensure that the extrusion was not large enough to cause cracking or significantly smaller than the cross-sectional area of the dovetail.

To minimize the z-force while still allowing for proper extrusion, the chosen operational parameters were 76 mm per min (3 inches per min) traversing speed, 1,500 RPM, and a 0.635 mm (0.025 inches) tool plunge depth. A pinless FSW tool with a convex, scrolled shoulder was used on a 3.18 mm (0.125 inches) thick aluminum AA6061-T6 plate. Using these operational parameters and tooling, six extrusions were performed. Clamping for the extrusion welds is shown in Figure 10.

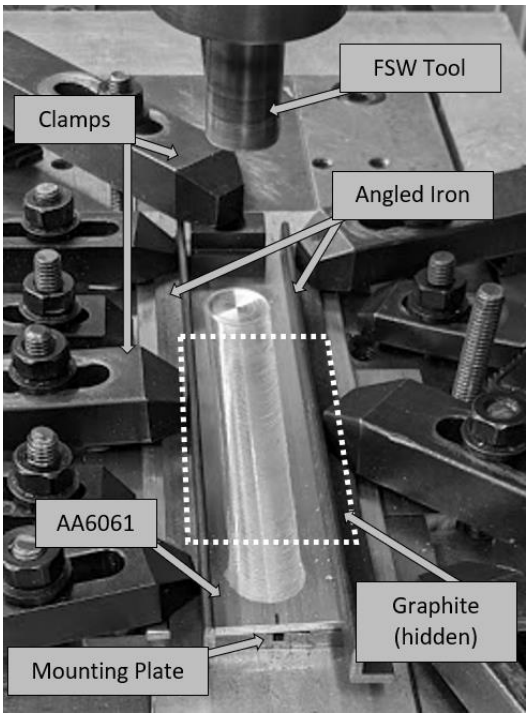

Figure 10. Extrusion clamping setup.

Testing Procedure

As extruded, the graphite plates were 101.6 mm (4 inches) long. Graphite extrusions were sectioned into three 25.4 mm (1 inch) wide samples, allowing for 12.7 mm (0.5 inches) sections on each end to be ignored as transient effects from the lead-on and lead-off tabs could have been present.

For metal-graphite FSE joints to show promise as a potential joining method, a measurable value of joint strength needed to be found. The intended applications for this configuration were expected to be in either compression or lap shear perpendicular to the weld path. To this end, the experimental methodology was developed to exclusively test lap shear. Other experimentation methods were considered but were ultimately decided against. Cross tensile testing of the joint would likely not provide useful data. Isostatically molded graphite does not plastically deform at ambient temperatures, which makes measurements of tensile strength unreliable [80]. Peel testing was likewise removed from consideration due to graphite's low ductility and inconsistent behavior in tension. Testing for lap shear is generally done with tensile testing per ASTM standards, however, due to graphite's previously described response to this loading configuration, the sample's shear strength was tested in compression. There are not any established ASTM standards for this joint configuration. Instead, ASTM D5379, "Shear Test for V-notched Beam" and ASTM A264-12, "Test Shear for Clad Plate" were used as starting points in the development of a fixture. The test fixture was used in an Instron universal testing machine under compressive loading, shown in Figure 11.

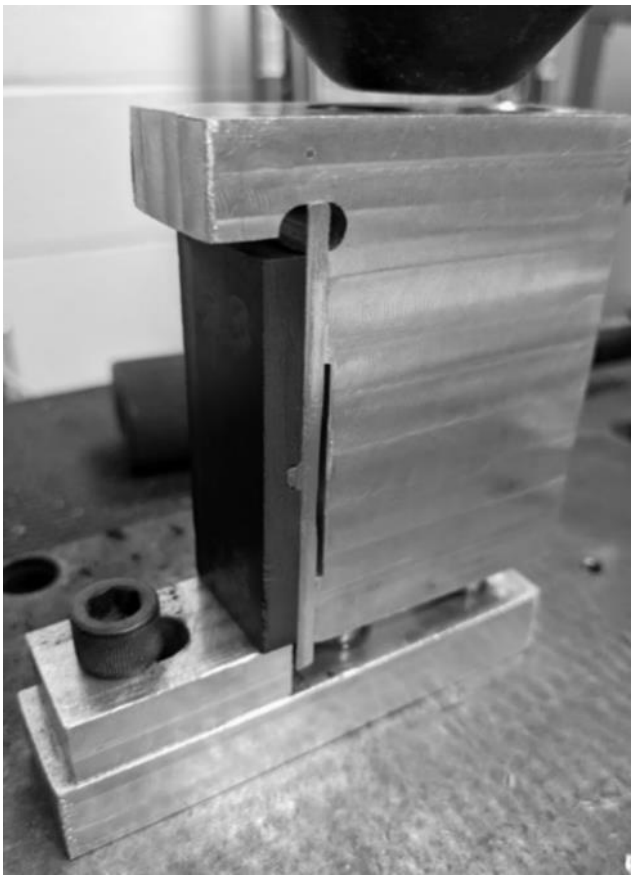

Figure 11. Compression testing fixture in the Instron universal testing machine.

Results

In total, 18 extrusion samples from six different extrusions were used. An extrusion is shown in Figure 12 along with a microscope image of the same sample. Figure 12.B presents several notable features of the extrusion process. There is a gap of 0.15 mm (0.005 inches) on the extrusion extremity caused by post-FSE thermal contraction. This can be verified by examining the geometries at the bottom of the groove, which have matching features. The other voids in the extrusion originally were filled with broken graphite sections and powder where the dovetail edges were eroded from FSE. Cutting the samples into sections and polishing lifted the loose pieces from the dovetail groove. One large section in the top right of the groove remained intact, which shows how the aluminum extruded in and around the graphite pieces. The dovetail extrusion and the captured graphite fragments allow the mechanical interlock to remain attached.

Another interesting feature is the top left portion of the groove where the dovetail edge was completely broken off. This trend is present in the majority of samples.

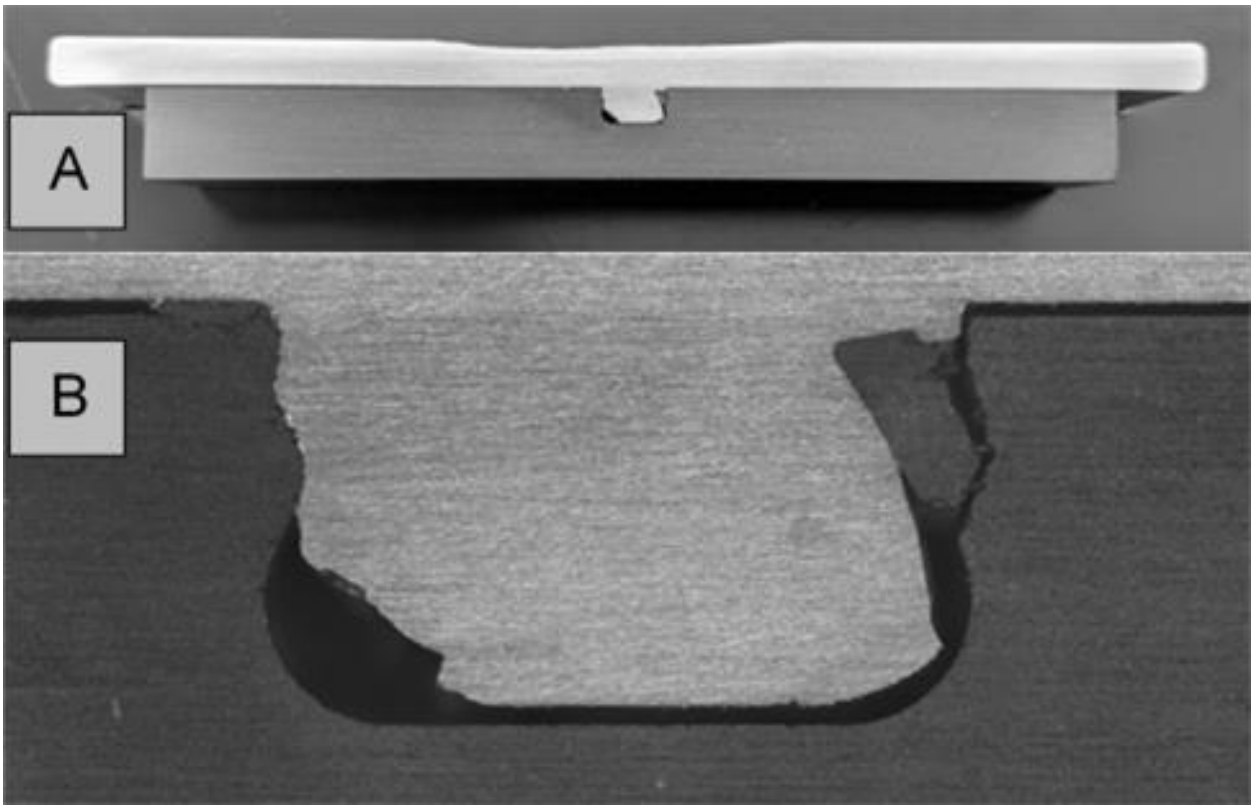

Figure 12. A: Example extrusion sample with AS on left. B: Optical microscope (5x magnification) image composite of aluminum extrusion in graphite.

Some joints failed when creating cross-sectional cuts, causing the aluminum and graphite to separate. Four samples, approximately 22%, were separated this way. One of these samples is portrayed in Figure 13. Even though this failure occurred, the graphite and aluminum still had an interlocking geometry in every direction except separation perpendicular to the workpiece interface. The samples with failed dovetails were noted and underwent the same lap shear testing as the other samples.

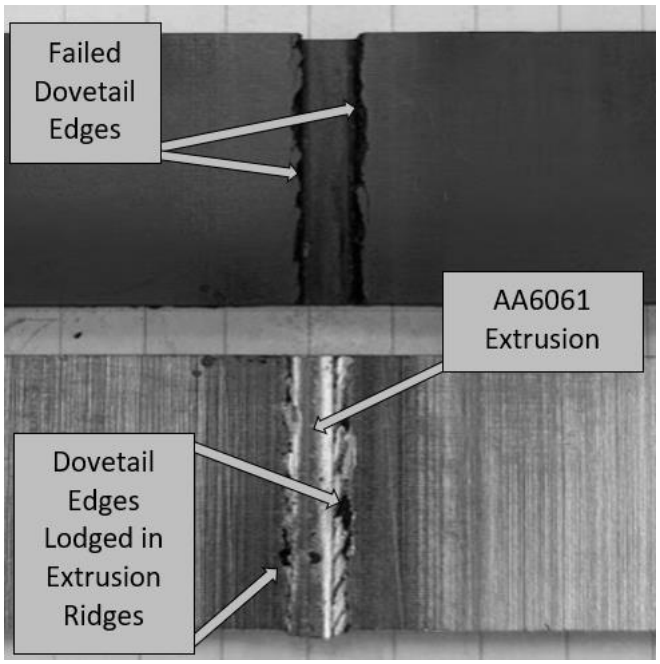

Figure 13. Failed dovetail joint.

Z-force

Z-force data from the extrusions are combined in Figure 14. This plot represents the phenomena that occurred during the process and provides further insight. At around 40 s, the z-force rapidly increased to a peak of approximately 5,000 N. This represents the initial contact of the FSE with the aluminum. Afterward, the z-force temporarily decreased as the aluminum temperature rose and plastic deformation began. The second increase in z-force represents when the transverse tool travel began. The transition to graphite from the lead-on tab showed a decrease in z-force, but it gradually increased over the length of the graphite plate. After traveling the full length of the graphite plate, the force decreased as tool retraction began. The section of greatest interest is when the tool traveled over the graphite segment. The z-force increased along the weld path in all trials. This is different than the extrusions performed with steel backing for determining process parameters that did not experience a z-force increase during extrusion.

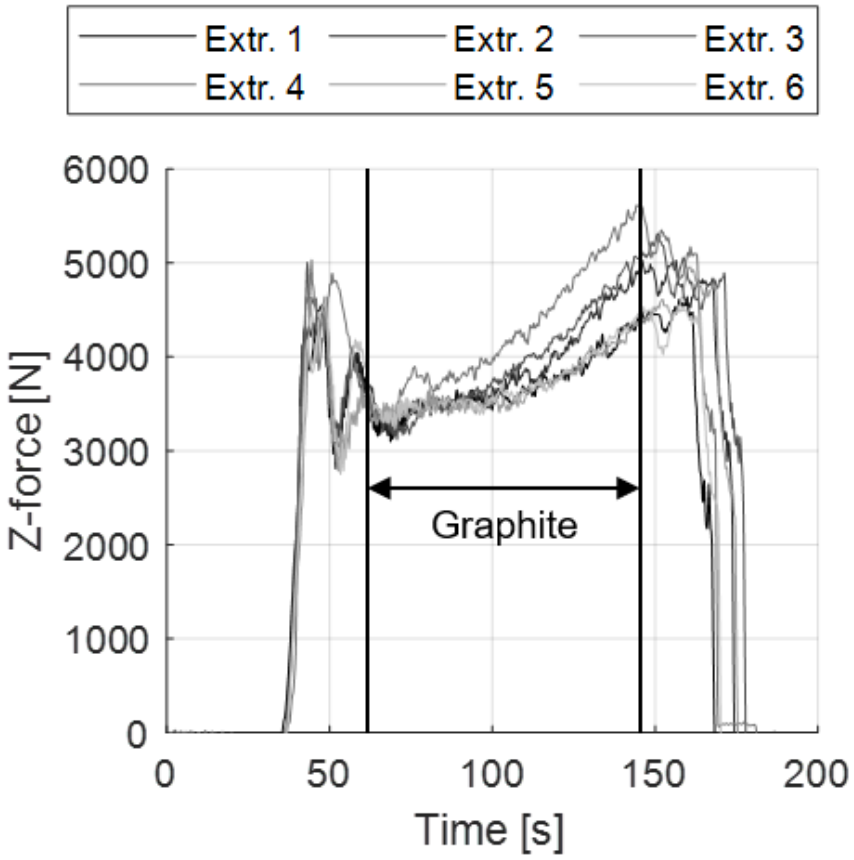

Figure 14. Extrusion z-force data.

Shear Strength

Due to the asymmetry of the extrusion shown in Figure 12, half of the samples were biased with loading on the RS of the graphite and the others with loading on the AS. Statistical analysis is shown in Table 1. Each sample populations represent a different grouping of results, where the first number in the sample name represents the extrusion and the second number represents the extrusion sample location.

Table 1. Extrusion sample analysis

Sample Population	Min Failure Load (N)	Max Failure Load (N)	Avg. Failure Load (N)	Standard Deviation (N)	Coeff. of Variation (%)
1.X	99.30	2908.28	1077.09	1295.84	120.31
2.X	1633.36	2093.82	1822.48	196.76	10.80
3.X	803.55	3665.98	2488.40	1222.39	49.12
4.X	988.31	1418.79	1167.56	182.96	15.67
5.X	264.81	3529.02	1749.94	1348.72	77.07
6.X	1499.12	2334.11	1846.78	354.90	19.22
X.1	223.69	2093.82	1085.29	708.28	65.26
X.2	99.30	2995.68	1620.16	915.73	56.52
X.3	988.31	3665.98	2370.68	1042.65	43.98
RS Loading	99.30	3665.98	1771.81	1412.93	79.75
AS Loading	988.31	2334.11	1612.27	406.24	25.20
Failed Joint	99.30	1418.79	636.33	524.14	82.37
Successful Joint	264.81	3665.98	1993.67	953.81	47.84
All Samples	99.30	3665.98	1692.04	1042.63	61.62

From Table 1, the high coefficients of variation show that the failure loads are not normally distributed. However, there seems to be a trend when looking at the AS and RS individually. While this trend cannot be empirically proven due to the small number of samples, it suggests some conclusions about joint strength. These trends are visualized in Figure 15.

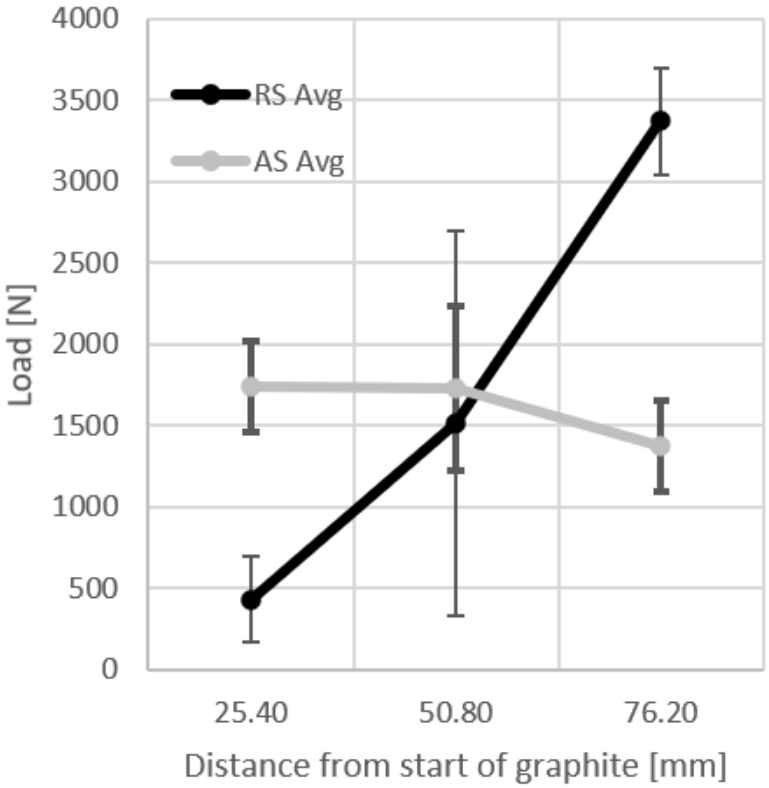

Figure 15. Average failure distributions by orientation.

The data suggests that joint strength is highly dependent on the direction of shear on the joint. Even considering variability, the strength of the RS increased significantly along the FSE path. The AS side has a more consistent failure load, with a slight decrease in strength along the length of the extrusion. The failure data measured in this study are qualitatively consistent with crack size, as seen in Figure 16. More visible damage along the dovetail region corresponds to a higher failure load.

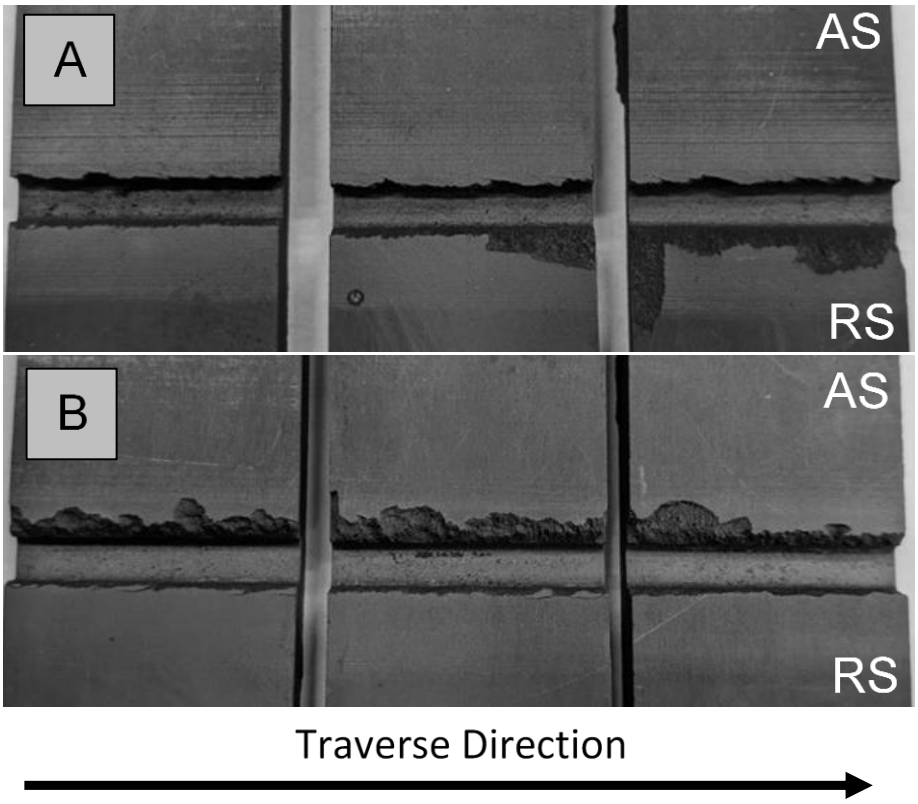

Figure 16. Graphite failures of two extrusions. A: RS test orientation, extrusion sample 5. The cracking on the bottom edge of the dovetail worsened as the FSE tool progressed. B: AS test orientation, extrusion sample 6. Cracking patterns were consistent along the dovetail edge.

As seen in Figure 16, the joints failed with the graphite breaking from the bottom of the dovetail to the faying surface. Only one sample failed with the graphite piece breaking in half. Sample 3.3, the sample with the highest failure load, broke in half from the bottom of the dovetail to the bottom of the graphite piece as shown in Figure 17.

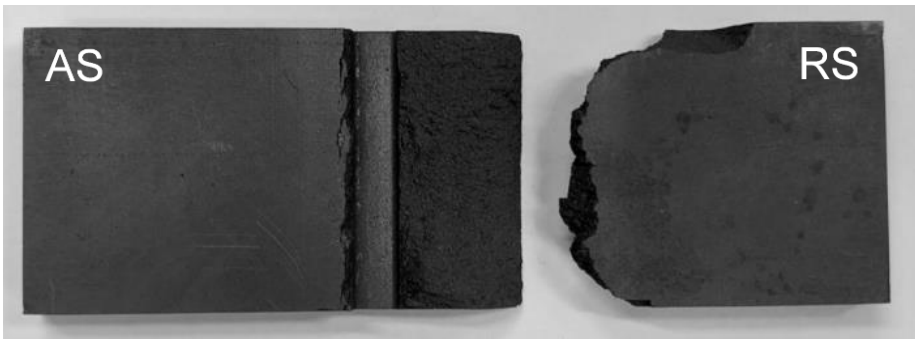

Figure 17. Sample 3.3 graphite failure.

Discussion

Metal-graphite FSE created successful joints. The graphite and aluminum remained attached even when the dovetail edges fractured in-process. From previously shown optical microscopy images (Figure 9 and Figure 12), there was still an interlocking geometry despite the minimal edge failure of the grove along the extrusion. Since the cracked graphite edges were displaced into the dovetail groove, they were still part of the joining mechanism. Figure 13 shows an interesting pattern on the edges of the aluminum dovetail. Rib-like ridges appeared along the extrusion path. These ridges simultaneously chipped away at the groove edges while aluminum extruded into and around the graphite fragments. The combination of these two actions enabled the graphite and aluminum to stay attached, even though the dovetail features became partially compromised.

Joint Strength

As seen in Figure 15, there were noticeable differences in strength with respect to the orientation of AS and RS within the testing fixture and with respect to the weld location. The error bars shown cover a wide range of values, the largest of which is the RS orientation. It is believed that this is due to the fixturing of the graphite during FSE. Graphite's brittleness means care must be taken to prevent cracking due to clamping loads. Fixturing for all tests minimized clamping above the graphite, a byproduct of which was aluminum forming a slight hump over the graphite. The highest point on the FSE path was 0.178 mm (0.007 inches) above the initial weld height. When considering that the FSW tool plunge depth was only 0.635 mm (0.025 inches), this caused approximately a 28% change in plunge depth. These differences can cause

noticeable changes in tool engagement, variability in extrusion, and joint strength. Like the RS orientation, the variability in the center of the extrusion for the AS orientation was also highest, suggesting that the height variability played a role in joint strength.

The increase in aluminum height also contributed to z-force variation. As the weld surface changed in height, the tool engagement and plunge depth also varied, which could explain the increasing z-forces in Figure 14. The increasing forces coincide with the increase in shear strength represented in Figure 15. It is hypothesized that these two events have a causal relationship. The z-force increases could represent an increase in aluminum extrusion. Cross-sectional changes in extrusion as seen in Figure 18 follow this trend. When considering the RS, the joint strength increased significantly from the beginning to the end of the extrusion. Analysis of the dovetail throughout the extrusion showed that the extrusion geometry changed, which might explain the change in strength on the RS side. The extrusion increasingly resembled a dovetail on the RS along the weld path. The change correlated with the increasing strength of the joint in the RS orientation.

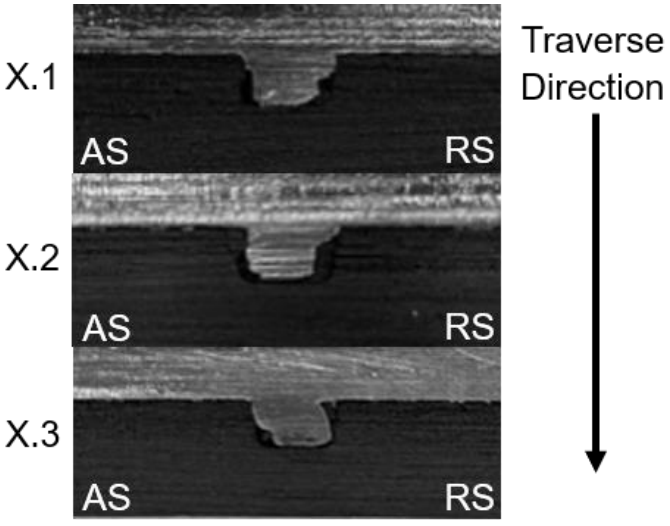

Figure 18. Extrusion cross-section change.

Conversely, the strength of the AS orientation held a somewhat constant failure load with a potential for a decrease in strength along the extrusion, likely due to the geometry differences in the dovetail's asymmetry. Initially, the AS geometry was nearly vertical from the top of the graphite to the bottom of the dovetail. The AS side changed slightly near the end of the extrusion

to have a downward slope from the edge to the bottom of the dovetail, potentially accounting for the slight decrease in AS strength shown in Figure 15.

The changing cross-sectional geometries and the correlating joint strengths suggest that different geometries could create stronger joints. When made of graphite, thin features like dovetail edges are inherently weak. By using a different groove geometry, a stronger joint might be possible. When looking at the joint strengths in Figure 15, the strength in the RS direction increased over the length of the extrusion. A longer section could allow this to reach a peak value, indicating optimal operating parameters.

Comparison with Brazing

A functional evaluation of FSE requires a comparison to an existing process. Since brazing is currently the most common method for joining graphite to metal, shear strength values of brazing allow a direct comparison. A comparable aluminum-graphite brazed joint was created by Yu et al., but no strength values were reported [75]. Instead, the measured joint strengths will be compared to a range of braze strengths for different material combinations. Braze strengths are highly dependent on the materials used, meaning that a broad range of literature values was found. Some reported values are 14 MPa (2030 psi) for a WC-Co alloy and Ag-Cu-Ti filler [70], 19.8 MPa (2871 psi) for copper and (Cu-50TiH_2)+B filler [75], 26 MPa (3770 psi) for Hastelloy N with Au filler [77], 34 MPa (4930 psi) for stainless steel with multilayer brazing [73], and 34 MPa (4930 psi) for steel with a BCu-1 filler [71]. These values form a range representing comparable strength to brazing. Normalized with the measured FSE area of 645 mm^2 (1 in^2), a failure load range of approximately 9000 N to 22000 N was found for literature values.

From Table 1, the maximum load of all the samples was 3665.98 N while the minimum was only 99.30 N. The coefficient of variation for all samples was 61.6%, showing high variability in the load at failure. The current maximum load of an aluminum-graphite FSE joint is less than a comparable brazed joint. However, the FSE process is not yet optimized. Joint strength is assumed to increase as this process is further developed.

Conclusions

Metal-graphite FSE was shown to be a repeatable joining process. As the first research to show this, the groundwork for FSE with graphite was formed. Various phenomena that occur were evaluated, with suggested causes and paths for future improvements discussed. A brief comparison of the joint strengths with brazing show that the failure loads are significantly lower than comparable brazing; however, even low shear strength is promising as a proof-of-concept. This suggests that through optimization of process parameters and graphite groove geometry a stronger joint could be created. Additionally, there could be more consistency in strength. While this process is repeatable, much still needs to be learned about FSE with graphite to allow expansion into varying applications and fields.

CHAPTER IV:
BUTTED FRICTION STIR FORMING OF AA6061-T6 TO LOW CARBON STEEL

Connor Strawn, Alvin M. Strauss

This chapter is published in the *Proceedings of the Institution of Mechanical Engineers, Part B: Journal of Engineering Manufacture* as:

C. Strawn, A.M. Strauss, Butted friction stir forming of AA6061-T6 to low carbon steel, Proc. Inst. Mech. Eng. Part B J. Eng. Manuf. (2022) 1–6. https://doi.org/10.1177/09544054221109085.

Abstract

Friction stir welding (FSW) is a popular method for creating dissimilar material joints in the aerospace and automotive industries. This work proposes a new FSW derivative process: butted friction stir forming (BFSF). BFSF has the distinction of joining two abutting workpieces to a lapped third workpiece. Additionally, the process does not require modification to traditional FSW equipment and tooling. In this study, BFSF combines two workpieces of aluminum alloy 6061-T6 in a butt weld configuration throughout the process. As the FSW tool traverses, it travels over preformed, threaded holes in low carbon ASTM A36 hot rolled steel at regular spacing. Downward force combined with the stirring action of the tool displaces material into the hole, filling the threads and forming a mechanical interlock. Testing of various screw sizes and thread pitches allowed the determination of the optimal joint configuration. Aluminum die-cut bolts of each size established a point of comparison for base material strength. Of the sizes tested, the ANSI metric M profile M9-1.25 screw had the highest mechanical strength. In cross-tensile testing, the average failure load was 3,915 N. Shear testing produced a failure load of 5,749 N. The M9-1.25 formed screws had a 33.6% decrease in strength compared to the die-cut bolts. While this strength reduction is higher than is often experienced in traditional FSW, the results of this study are a valid proof of concept for further development in BFSF methods.

Introduction

Benefits of friction stir welding (FSW), such as low workpiece distortion, low residual stresses, and the ability to join dissimilar materials, make it an attractive technology for further research and development [6]. FSW is particularly well-suited for dissimilar material joints, often difficult or impossible to produce with fusion welding techniques [83]. Dissimilar material structures are a valuable design option due to flexibility in desired material properties, such as optimizing desired strength to allowable weight. FSW expands on the possibilities of dissimilar material combinations by joining workpieces that are difficult or impossible to perform with more traditional methods. Previous FSW research shows joinable dissimilar material pairs, such as metals [50,83–87], polymers [88] ,and composites [64,89], Traditional and derivative FSW processes can weld this wide range of materials. General-use FSW configurations include butt welding, lap welding, and spot welding. Less commonly, FSW can create a mechanical joint by plastically deforming welded material into a separate, non-welded workpiece. Several derivative processes rely on this phenomenon: friction stir forming [90,91], friction stir extrusion [49], the friction stir scribe technique [92], and friction stir dovetailing [50]. These processes use one workpiece to fill a void in a separate workpiece and form an interlocking geometry. Intermetallic compounds can be encouraged or suppressed depending on tooling, materials, and operating parameters. These forming processes mainly use aluminum alloys, including AA5083 [51], AA6022 [92], and AA6061 [93]. Butt welding and friction stir forming are well-documented processes; however, no published examples of butt welds combined with a forming process exist. Combining these two methods allows for a joint of three separate workpieces with a single operation. Minimizing operations leads to a reduction of assembly time and weight compared to traditional fasteners. This novel process was named butted friction stir forming (BFSF).

BFSF is well-suited for aerospace and automotive applications. In aircraft construction, exterior skin attaches via fasteners, rivets, and fusion welding, but FSW and its derivatives have the opportunity to replace these traditional techniques [94]. The Eclipse 500 is one such example where FSW was used instead of 7,378 conventional fasteners [5]. Switching to BFSF enables multiple skin section combinations and joining with wing structural members like ribs, stringers, or spars. Replacing fasteners, riveting flanges, and lapped skin material through BFSF will reduce the weight of the assembled structure.

The automotive industry would also benefit from BFSF. Switching from exclusively steel construction to a hybridization with aluminum leads to weight reduction. Numerous methods can join these two materials, including self-pierce riveting, mechanical clinching, hemming, and FSW [95]. Dissimilar material FSW has been employed in production vehicles, for example, the aluminum-steel engine cradle in the Honda Accord [6]. Additionally, friction stir forming research has been performed focused on the automotive industry [9]. Since BFSF is a modified friction stir forming method, automotive applications of this technology are a natural next step.

BFSF is a promising alternative to current joining techniques. The novel FSW and friction stir forming combination allows for unique workpiece configurations that use fewer fasteners and operations than fusion welding, FSW, and friction stir forming. The FSW element of BFSF enables the joining of two workpieces that readily FSW, like the AA6061 used in this work, while the friction stir forming element enables simultaneous joining to a material that is more difficult to FSW, such as low carbon steel. This dissimilar material joining process has the potential for advancement in the aerospace and automotive industries via otherwise unfeasible joint configurations or faster fabrication of existing joint configurations. The purpose of this study encompasses validating BFSF as a capable process and establishing a foundation for future research.

Materials and Methods

FSW performed for this study employed a modified Kearney & Trecker Model K mill outfitted for fully automated operation. Instrumentation allowed for in-process force, torque, and position measurements. The modularity of the welder setup enabled easy changes in tooling, controls, and instrumentation depending on the desired FSW setup. Due to the straightforward weld configuration, an open-loop speed controller was adequate for this work.

Testing various hole sizes and thread pitches helped determine optimal joint configuration performance. ASTM A36 hot rolled low carbon steel 3.175 mm (0.125 in.) thick, 50.8 mm (2 in.) wide, and 152.4 mm (6 in.) long was pre-drilled for 75% thread engagement and tapped for ANSI metric M profile screws at M5-0.8, M6-1.0, M7-1.0, M8-1.25, M9-1.25, M10-1.5, and M12-1.75. The formed and welded material in this study is AA6061-T6. Workpiece orientation and step clamps ensured that the seam between the butted aluminum pieces bisects

the threaded hole in the steel. Figure 19 contains the chosen configuration before and after welding. A convex scrolled-shoulder pinless H13 tool steel FSW tool, successful in thin sheet friction stir extrusion [27], was used. The weld path was centered on the aluminum seam line and directly above the threaded hole. Previous friction stir forming research showed that this tool path leads to a high fill rate in the formed region [96].

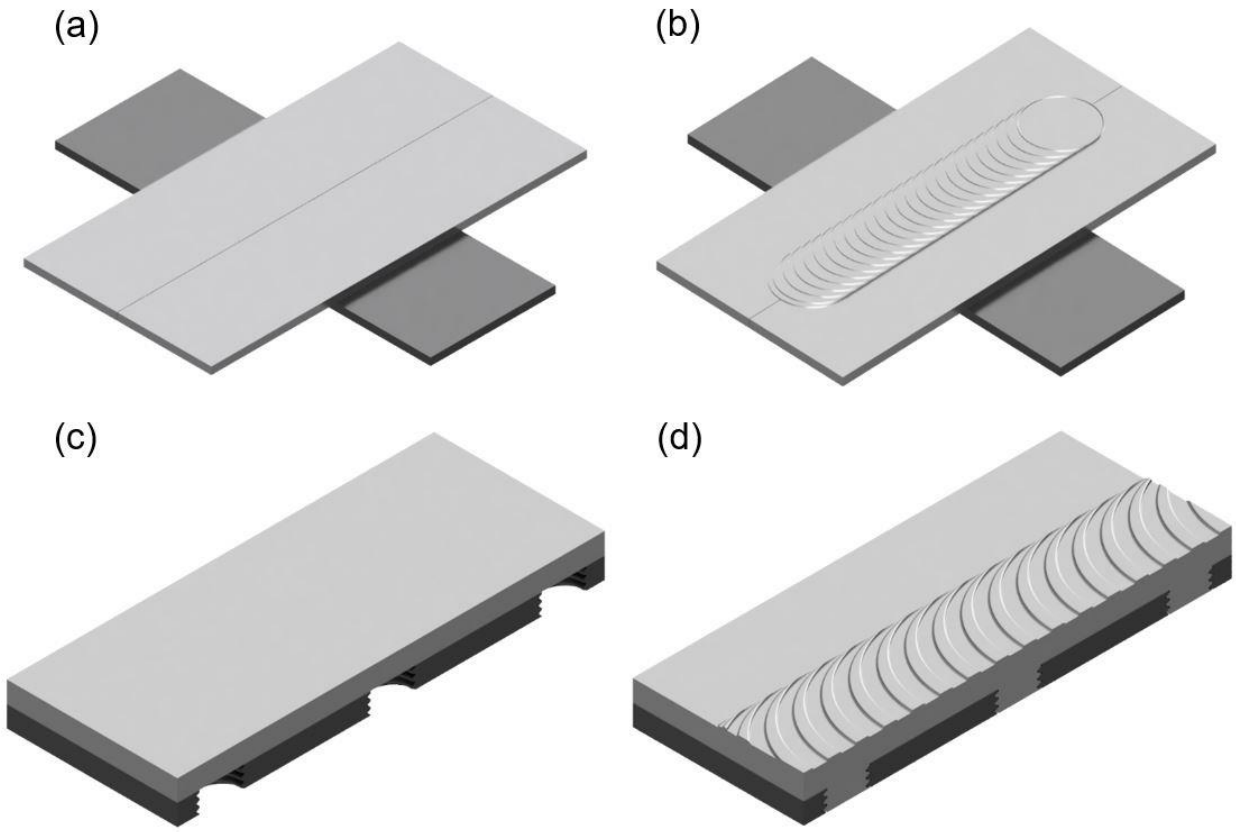

Figure 19. Weld configurations with AA6061 sections above low carbon steel. Holes were drilled and tapped before joint assembly. Sample (a) before and (b) after BFSF. A cross-section of a potential BFSF application with multiple holes along the weld path (c) before and (d) after welding.

Multiple preliminary welds (three per hole size) determined the optimal candidate parameters and configurations by using surface defects and hole fill as evaluation metrics. Of the parameters tested, the best performance for surface finish and hole fill came from a plunge depth of 0.762 mm (0.030 in.), a tool rotation speed of 1500 RPM, and a welding speed of 76.2

mm/min (3 in./min). The amount of deformed material differed between hole size, directly relating to the amount of material displaced from the top of the welded joint. If there is complete fill, a larger formed screw will have greater shear strength with a tradeoff of thinning and weakening the butted section near the formed joint. Cross-tensile testing determined the sample failure loads.

The three BFSF joints with the best performance were reproduced (three per hole size) and tested in shear loading. Testing used 15 mm (0.6 in.) wide sections from the welded samples. Threaded hole sections were tested by clamping the retreating edge of the butt-welded aluminum and the steel on the advancing side. Aluminum-only sections from other locations in the weld path were tensile tested. Samples from immediately before and after the formed screw allowed evaluation of joint strength by location. Additionally, die-cut aluminum bolts enabled a strength comparison of the formed screw material with the base material.

Results

The BFSF process produced successful joints. Figure 20 shows axial and lateral cross-sections as well as an unscrewed image of the formed screw exterior. The crack-like feature in the axial cross-section is a root flaw caused by improper penetration and mixing [97]. Except for M5, M10, and M12, the small and large extremes, the fill was nearly complete in all samples.

Cross-tensile testing helped to determine the optimal BFSF joint configuration(s). Excluding M5, which fractured at the minor diameter cross-section, all formed sections experienced aluminum thread failure. While shear strength is generally a better metric for evaluating mechanical properties, the slight fill variability and exact thread surface area uncertainty led to the use of failure loads instead as a point of comparison. The average failure load for each set of samples, as plotted in Figure 21(a), shows that the highest cross-tensile failure load occurred with the M9 joint at an average failure load of 3,915 N (880.1 lbf). The M9 joint was the largest size that experienced complete fill. Even though the M10 formed screw had a strength of 3,788 N (851.6 lbf), the incomplete fill prevented further study for that size. The M12 joint similarly showed incomplete filling. Excluding incomplete fill, the three sizes with the highest failure load were M7, M8, and M9.

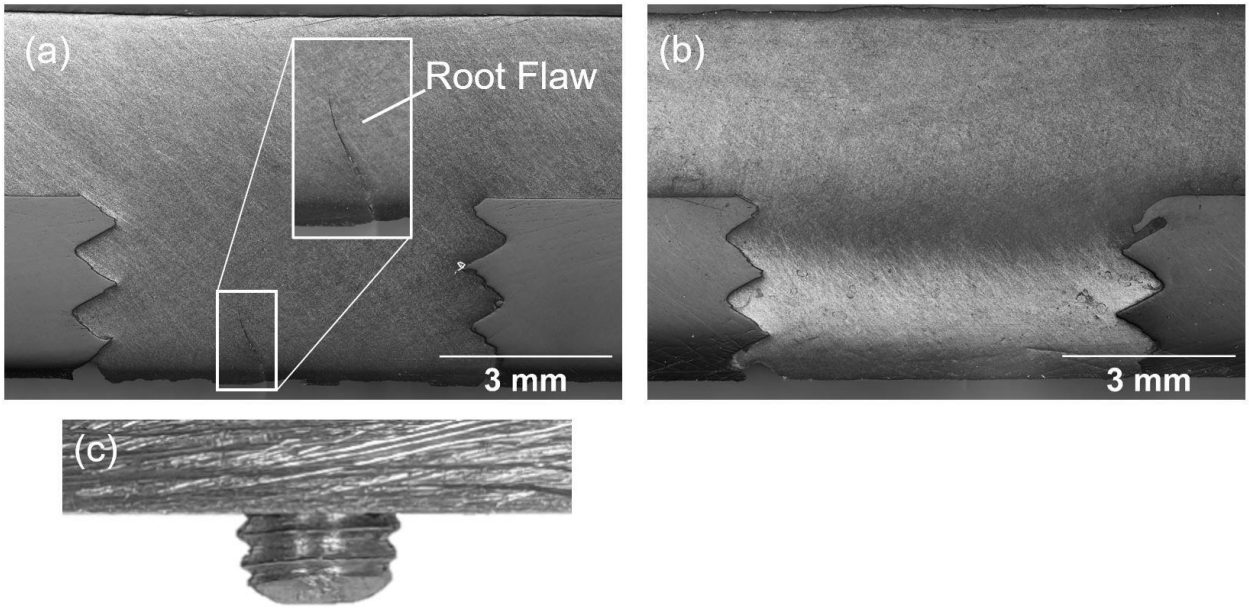

Figure 20. BFSF Images. (a) M7-1.0 axial cross-section with the advancing side on the right side of the image, root flaw emphasized, (b) M7-1.0 lateral cross-section with the weld advancing from right-to-left, and (c) formed aluminum unscrewed from steel.

Additional testing required more BFSF welds of the chosen sizes. The formed screw shear failure loads of M7, M8, and M9 are, respectively, 4,329 N (973.2 lbf), 5,000 N (1,124 lbf), and 5,749 N (1,292 lbf). Comparing these values to the die-cut bolts from Figure 21(b), the formed screws for M7, M8, and M9 had a strength reduction of 22.5%, 27.1%, and 33.6%, respectively. Evaluating failure loads along the weld showed that strength is dependent on location with respect to the formed screw. Figure 21(b) shows how the failure load 15 mm (0.6 in.) before the formed screw was weaker than 15 mm (0.6 in.) after. Before (-15 mm) and after (15 mm) the formed screw along the weld path, the M7, M8, and M9 failure loads increased by 37.9%, 61.8%, and 48.4%, respectively. The force discrepancy led to an investigation of the in-process z-force, shown in Figure 22. Z-force was measured using a Kistler 9123C piezoelectric dynamometer. The initial drop in z-force occurred when the leading edge of the tool reached the edge of the threaded hole.

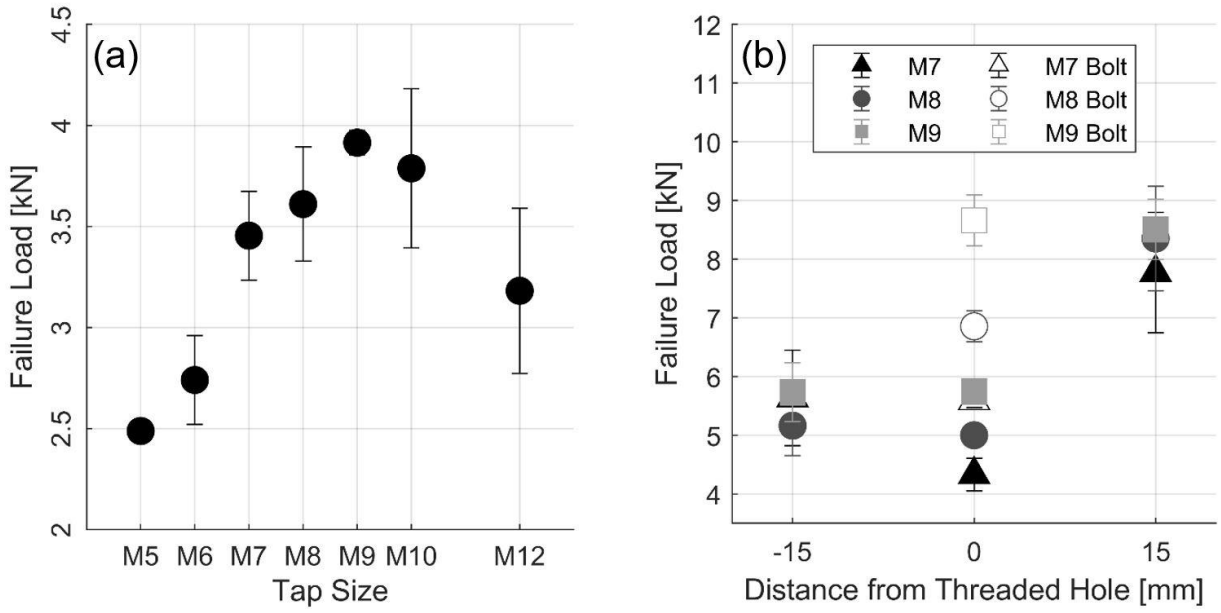

Figure 21. BFSF joint failure loads. Each point is the average of three replicates with error bars showing sample standard deviations. (a) Preliminary cross-tensile testing. (b) Tensile failure load by location and comparison to die-cut bolts shear strength.

Discussion

Results show that BFSF produces sound joints. Defects were minimal, with the only observed mode in all samples being root flaws. Root flaw defects propagated along the vertical butted plane, shown in Figure 20(a). Adjustment of weld parameters may mitigate the presence of defects in the samples. The parameters (listed in Materials and Methods) stayed constant throughout each weld, regardless of the threaded hole location. The highly coupled nature of these parameters makes it difficult to predict which parameter change(s) would have the greatest impact on weld quality. When considering the parameters individually, welding speed and tool plunge depth are likely the most impactful. Decreasing the welding speed allows for extended interaction with the formed volume and increased plastic deformation. A deeper tool plunge would raise the z-force and maintain shoulder contact as the material forms into the hole.

An alternative optimization technique to parameter variation includes changing the workpiece configuration. Testing a range of tap sizes demonstrated that M9 had the highest failure load in a cross-tensile test. M9 threaded holes were also the largest diameter size which

experienced complete fill. The fill and coarse thread pitch show that the M9 formed screws have the highest contact area, a useful metric for joint integrity. In shear testing, the M9 hole size had the highest strength for all tested configurations. From these results, M9 was shown to be the optimal size.

Comparing the formed screws with the die-cut bolts, the shear strength of the die-cut bolts was noticeably higher, likely due to the inherent weakening of material that occurs during FSW. FSW aluminum alloys generally experience a strength reduction between 10% and 34% compared to the base material [98,99]. Results show the largest reduction from bolt strength to formed screw joint strength as 33.6%. This value is on the high end of values reported from literature [98,99]; however, die-cut bolts are not an exact analog to roll threaded bolts or parent material due to weakening from thread cutting. Regardless, the level of retained strength is notable, especially since the samples produced from this study had root flaws in the formed screws.

Another notable result from shear testing is the strength found before and after the formed screw location. Displacing material from the weld path into the threaded hole led to localized thinning of the butted section near the forming region. FSW and its derivative processes, such as BFSF, are often classified as an extrusion process, extruding material from the tool's leading edge to the trailing edge [18,100]. This phenomenon affects the strength of the material before and after the threaded hole in the weld path. When deformation occurs in the threaded hole, there is less material available to sweep behind the tool. Less material leads to a reduction in shoulder engagement and forging forces. The strength immediately before the formed joint is lower than the strength after, as seen in Figure 21(b). After the forming location, the material strength noticeably increased across all trials. BFSF does not affect the failure load after forming since extruded material travels from the front to the back of the tool. In this scenario, the same volume of material in the BFSF path is present before and after the FSW tool, allowing for consistent tool engagement and strength.

The plot in Figure 22 provides further evidence of reduced shoulder engagement. The z-force decreased more for the larger holes and over a longer period. As the material flowed into the hole, there was less material for engagement, resulting in the shown force variations. The M5 formed screws experienced the lowest and shortest drop in z-force, while the M12 formed screws

experienced the largest and longest dip in z-force. Increasing hole size and decreasing z-force are present in all trials at every tested hole size.

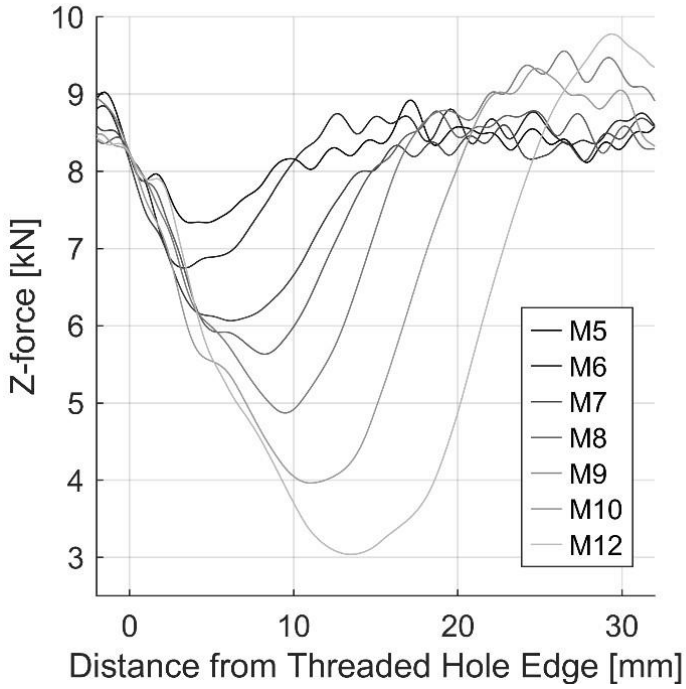

Figure 22. Measured z-force along the weld with respect to the threaded hole.

Conclusions

This work introduced and validated a method of dissimilar material joining called butted friction stir forming. This method is an efficient method of joining multiple aluminum sheets to steel structures that uses existing FSW tooling and may have applications in several industries. The optimal size for the selected parameters is M9-1.25. In cross-tensile testing, the M9-1.25 joints failed at an average of 3,915 N (880.1 lbf). During shear testing, the M9-1.25 joints failed at an average of 5,749 N (1,292 lbf). The testing of aluminum die-cut bolts showed that the formed screws had a 33.6% decrease in strength. While weaker than traditional FSW, the percentage of base material strength that BFSF retains is a promising proof of concept. Further study is needed to determine ideal parameters and joint setup for a given application. Additionally, the strength discrepancy before and after the formed screw has implications in any forming FSW process.

CHAPTER V:
ADAPTING BUTTED FRICTION STIR FORMING TO CURVED SURFACES

Connor Strawn, E. Jeremy Trujillo, Alvin M. Strauss

This chapter is under review at the *Journal of Manufacturing Processes.*

Abstract

Novel friction stir welding (FSW) derivative processes are continually developed, including butted friction stir forming (BFSF). The present work aims to expand the BFSF technology to curved surfaces. Curved BFSF has potential applications in the aerospace, automotive, and piping industry, such as joining multiple skin sections to a rib, body panels to a frame, or pipe sections to each other. A modified pipe FSW apparatus approximates curvilinear surfaces via partial circumferential welds. This work used a pair of butted aluminum alloy 6061 pipe rings (114 mm OD) lapped over an A500 steel pipe ring (102 mm OD) with four blind holes in each steel ring for BFSF extrusions. The holes were hand-threaded with 1/4-20 UNC taps. Each set of rings accommodated four welds with an arc length of approximately 100 mm. The tool offset range from radial alignment with the rings is 0 mm to 9 mm. The offsets are specific to the size of the workpieces, so the development of a more generalized term would expand the applicability of the results. The tool tilt angle, tool offset, and ring diameter are variables for calculating an equivalent tilt angle term describing the tool-workpiece orientations. The offset range corresponds to an equivalent tilt angle range of 0º to 9º. An angle of 6º had the best overall performance with a tensile strength of 156.0 MPa and a shear strength of 133.5 MPa. The observed weld integrity and measured joint strength validates BFSF for curved surfaces.

Introduction

Friction stir welding (FSW) is an increasingly employed advanced manufacturing process for joining materials through plastic deformation. A significant body of research exists on this process, spanning over thirty years since its inception at TWI in 1991 [1]. Most of this research focuses on flat or nearly flat surfaces. In manufacturing, non-linear and non-planar tool paths are often necessary for joining operations.

Curved surface FSW is a well-established field of research, with a focus on pipe joining [101–104], pressure vessels [2,3], and more general-use complex curved surfaces [58,105]. When shifting from planar FSW to curvilinear FSW, several parameters require consideration: the radii of surface curvature, tool geometry, and tool tilt angle. Of these, the radii of the surface curvature constrain the final product design. Design components are changeable, but generally, they have specified dimensions for the intended application. As such, the surface curvature is likely unable to be altered significantly for the initial adoption of curved FSW. However, the tool geometry is adjustable to accommodate some curvature [3,106]. Tools operate well in a specific design range of operating parameters [2], but the surface curvature will have varying radii. Due to curvature variability, the tool geometry must be compatible with the tilt angle to accommodate as many surface geometries as possible.

In standard FSW terminology, the tilt angle is the angle the tool's central axis makes perpendicular to the workpiece. Tilt angles generally vary from 0º to 4º [3,55,107]. For flat plate FSW, the tool maintains a consistent or nearly consistent angle throughout the process. Tilt angles contribute to deeper penetration on the tool trailing edge, also called the tool heel [12]. When the workpiece surface curvature varies, the relative tool angle to the workpiece changes depending on the tool's location and angle of attack. As the tilt angle changes, operating conditions for the workpiece surface change, meaning that the new set of conditions may be suboptimal for tool engagement, forging forces, and surface appearance. Without proper penetration and alignment, the joining process efficacy will suffer. Variable surface curvature can lead to inconsistent weld surfaces, strengths, and defects along the weld path. Weld consistency of curved surfaces also impacts derivative FSW processes.

Butted Friction Stir Forming

Curved surface FSW is adaptable to other derivative processes, such as butted friction stir forming (BFSF). BFSF could benefit the aerospace and automotive fields due to its ability to join dissimilar materials. Two aluminum sections can be joined with a butt weld while being joined to another piece through forming, such as steel or even a different aluminum alloy. The butted sections could be dissimilar aluminum alloys, enabling a joint of three distinct materials. Joining materials this way does have disadvantages, such as galvanic corrosion (a problem in many dissimilar material combinations/techniques), but that is beyond the scope of this work.

The BFSF material extrusion forms a threaded pin profile, allowing a mechanical interlock of the aluminum butt weld with a third steel member. This work aims to expand the technology by testing it on a curved surface. A potential application of this process is on aircraft to join wing skin sections to spars, ribs, or stringers. This proposed configuration is a curved BFSF version of the T-joint skin-stringer welds used by Mustafa et al. [108]. Instead of the currently used rivets, BFSF could join the materials without the weight of rivets and the flanges required for attachment [5,61]. While it is secondary to the present work, it is notable that curved BFSF has applications in industries other than aerospace and automotive. In pipe welding, joint creation does not require a fitting or valve. As such, there is less of a concern with bacteria ingress. Potential applications include food or pharmaceutical production.

Materials and Methods

The intended application of curved BFSF as an aerospace or automotive technology encouraged the use of a lightweight alloy commonly used in both industries: AA6061-T6 [98]. The curvilinear workpieces used in this study were AA6061-T6 rings cut from a pipe with an outer diameter of 114 mm (4.5 inches) and a wall thickness of 5.8 mm (0.23 inches). The aluminum rings were 38 mm (1.5 inches) wide. Inside the aluminum rings was a 38 mm (1.5 inches) wide low-carbon A500 structural steel ring cut from 102 mm (4.0 inches) outer diameter pipe with a wall thickness of 5.3 mm (0.21 inches). Figure 23 shows these workpieces and how they mate together. The figure also shows how the drilled and tapped holes line up with the aluminum-aluminum faying surface. Machining four holes around the outer face of the steel before mating with the aluminum rings allowed for forming locations in experimentation. The

FSW machine work envelope and mechanical testing equipment limitations constrained the workpiece dimensions.

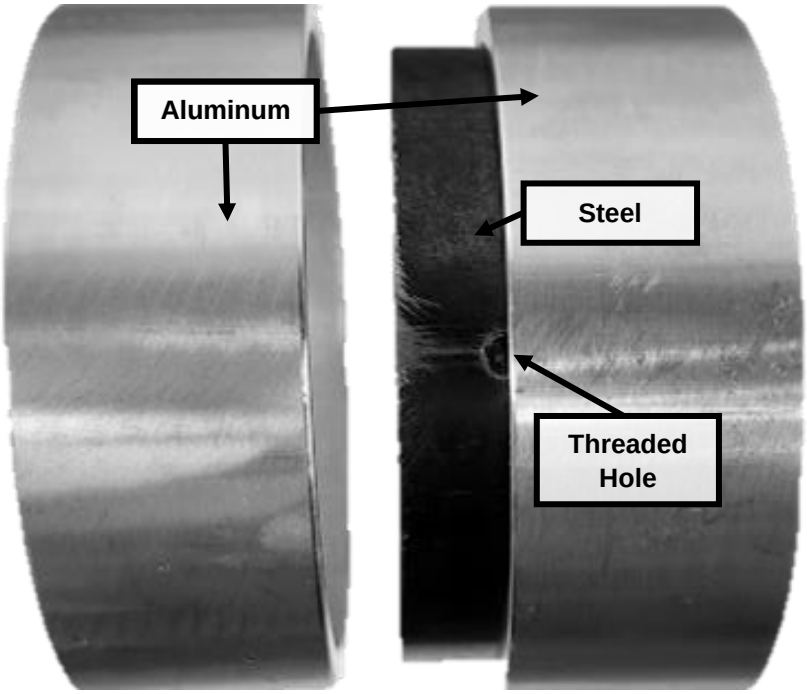

Figure 23. Workpiece assembly. The internal steel ring has four threaded holes on its circumference. Two aluminum rings slide over the steel concentrically and butt against each other.

Previous BFSF research showed that ANSI metric M profile M9-1.25 had the best performance when compared to a range of M5 to M12 [109]. The work used 3.175 mm (0.125 inches) thick workpieces of both AA6061 and low carbon steel with a pinless FSW tool. Since the present work is a preliminary investigation into curved BFSF, it used a more conservative hole and thread size of 1/4-20 UNC to ensure a proper fill. The selected thread size has a large enough minor diameter to allow extrusion but not wide enough to leave significant voids on the workpiece surface [109]. The coarse thread pitch of 20 threads per inch improves aluminum extrudability during welding.

Process optimization required testing through holes and blind holes in the steel workpieces. Experimentation demonstrated that through holes allowed too much material displacement, leaving voids on the top of the workpiece and having poor fill in the threaded

holes. Without having a reacting force on the bottom of the hole, the aluminum did not form into the threads. The extrusion was effectively a cylinder of the minor diameter of the screw. Blind holes had the best performance since they created a die to which the extruded material could conform. The aluminum takes the form of threaded holes in reaction to the welding forces. Testing of multiple hole depths showed that 4.75 mm (0.188 inches) allows for an optimized balance between the number of complete threads and depth. This optimized threading and depth encourage a solidly formed screw shank with adequate thread fill.

Apparatus

To prepare the workpiece, the aluminum rings were press-fit onto endcaps that provide workholding while reducing eccentricity that may have been present from material manufacturing. When mated concentrically, the steel outer surface and the aluminum inner surface had a small gap of approximately 0.5 mm (0.02 inches). Gaps could allow the aluminum rings to deform and become more eccentric. A tapered inner mandrel expanded cut steel rings to prevent gaps. A bandsaw cut one side of the rings to allow expandability. The split ring with the mandrel allowed for complete, concentric contact between the steel and aluminum pipes. The aluminum ring joint line bisected the prepared screw holes in the steel rings.

BFSF on a curved surface requires a method to perform circumferential welds on pipe sections. A rotary table supported the aluminum and steel ring assembly. The setup is a modified version of the pipe welding setup used by Lammlein et al. [104] and is similar to the apparatus used by Akbari and Asadi [102]. A modified milling machine equipped for FSW performed the curved BFSF for this study, shown in Figure 24. While the configuration is a pipe welding apparatus, the rings do not represent pipe sections but serve as an analog for small radii curvature in a structural application. The weld conditions are clarified further in the experimental procedure later in this section.

The tooling used is another consideration when switching from planar FSW to a curved surface. Successful welding requires an adequate balance between shoulder contact, pin penetration, and surface features. Tool testing involved trials with various FSW tool geometries, including a conical tool, a flat-shoulder tool with a pin, a pinless parabolic-shoulder tool, and parabolic-shoulder tools with different probe lengths. The best-performing FSW tool had a 3 mm

(0.12 inches) pin to allow complete shoulder contact and a 25.4 mm (1-inch) tool diameter for an increased stirred volume.

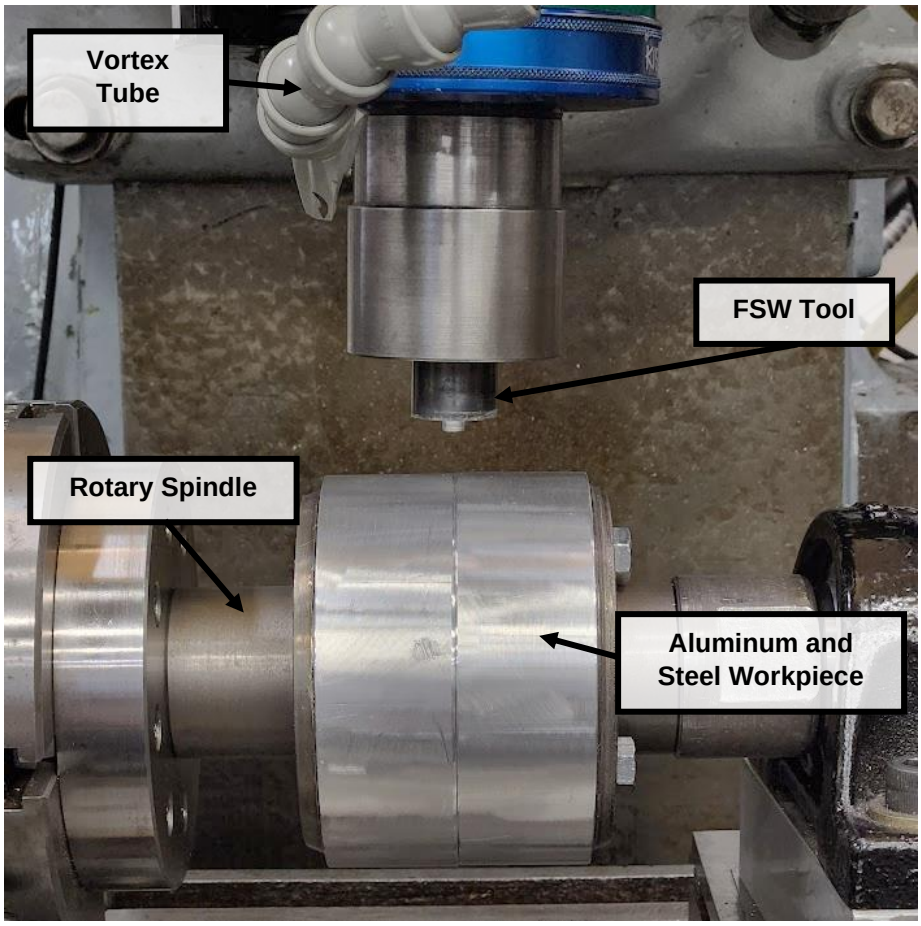

Figure 24. Pipe welding apparatus.

Equivalent Tilt Angle

FSW tooling parameters directly relate to maximizing joint strength. During FSW tool testing, the tool offset relative to the workpiece curvature contributed significantly to weld quality. Some curved surface FSW studies recommend the tool being radially aligned with the surface curvature [101], while other research showed that an offset improves the FSW of curved surfaces [104]. To determine the best conditions for the curved BFSF process, welding parameters and the distance from perpendicular to the workpiece varied.

While the FSW tool was kept vertical in the present work, the tool offset created a tilt angle with the workpiece surface. The measured offset is the lateral offset from tool's radial

alignment with the ring. Figure 25 shows the offset measurement references. Over 70 trial welds produced a range with consistent surface finishes and minimal voids: a 0 mm offset to a 9 mm offset.

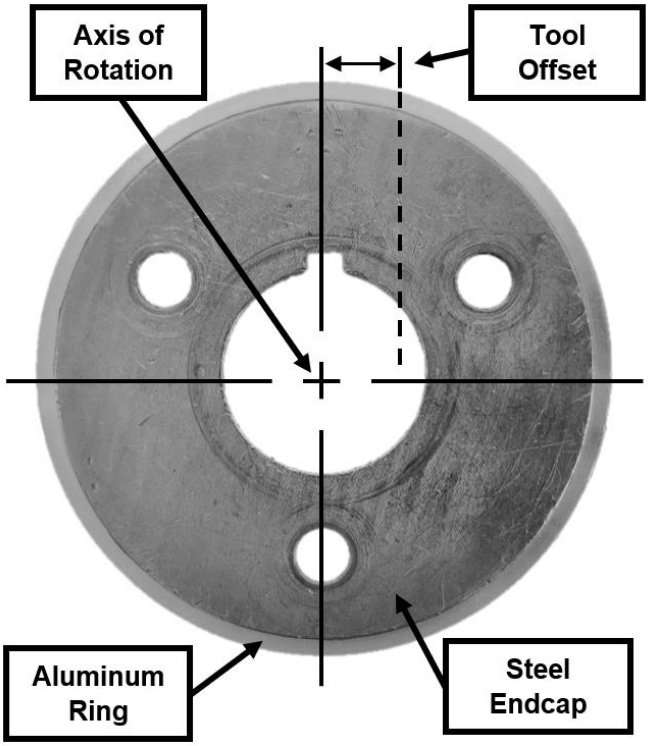

Figure 25. Ring assembly with offset measurement locations.

Offsets and corresponding weld efficacy are highly dependent on workpiece diameter. A framework for comparing offsets and diameters would expand the applicability of this work. A generalized equivalent tilt angle term enables a comparison of surfaces with different instantaneous radii. The equivalent tilt angle calculation uses the tool's direction vector, shown in Eq. (1), and the velocity vector, shown in Eq. (2).

$$\vec{t} = \langle sin(\theta)\,, cos\,(\theta)\rangle \tag{1}$$

$$\vec{v} = \langle \dot{x}, \dot{y}\rangle \tag{2}$$

The angle θ represents the tool angle with respect to the global reference frame, the velocity component in the traverse direction is $\dot{x}$, and the velocity component in the vertical direction is

$\dot{y}$. A modified dot product equation simplifies to find the equivalent tilt angle, θ_{eq}, as seen in Eq. (3).

$$\theta_{eq} = sin^{-1}\frac{\vec{v}\cdot\vec{t}}{|\vec{v}||\vec{t}|} \tag{3}$$

Equation (3) uses the curve's instantaneous velocity vector, an indicator of the radii, in the calculation, meaning that it is adaptable for several different curvatures. This work used circular rings, so the radius is constant. Assuming a constant radius and a 0º preset tool tilt, the equivalent tilt angle calculation reduces to

$$\theta_{eq} = sin^{-1}\frac{d}{r} \tag{4}$$

where d is the tool offset and r is the radius of the pipe. With a known workpiece radius, the equivalent tilt angle calculation only requires the offset used. The range of applicable offsets found in preliminary work gives an equivalent tilt angle range of approximately 0º to 9º.

Experimental Procedure

The 40 individual experiments used a single, threaded hole in the middle of an approximately 76.2 mm (3 inches) long weld. These short welds differentiate this work from pipe FSW research, meaning that some problems experienced with pipe welding are not a concern. In pipe welding, the welds are a complete circumference between the workpieces. There are concerns about unwanted preheating along the tool path and keyhole formation left by the tool pin upon weld termination. To prevent heat accumulation that would be present in pipe welding, workpieces cool for ten minutes through forced-air convection from a vortex tube. The tool keyhole is also not a concern since large structural projects could employ a retractable pin or a runoff tab. After each weld, the workpiece rotates to a section of virgin material to perform the next weld. The circumference of the rings allowed for four separate welds on each workpiece.

Evaluation Methods

Tensile and shear strength testing allows for an evaluation of the mechanical properties of the resulting joints. Tensile strength testing pulls the edges of the aluminum-aluminum joint on opposing sides of the weld path. This loading configuration shows the weld path strength with respect to the equivalent tilt angle and the volume of material extruded. As more material forms

into the threaded hole, less material is present in the aluminum-aluminum joint. Material movement creates somewhat of a tradeoff as the displaced material will improve the strength of the formed screw. Shear testing provided strength measurements of the aluminum-steel joint. A compression configuration that sheared the aluminum rings relative to the steel ring produced shear strength values.

The in-process forces of the welds can also be insightful when determining weld formation and resulting strength. The axial tool force is analyzed to compare how the different equivalent tilt angles relate to the tensile and shear strengths of the resulting welds. In-process forces are insightful for predicting void formation [28,110].

For evaluating weld appearance, specimens were cut along the aluminum-aluminum faying surface to show a cross-section of the screw hole and extrusion. Sample imaging used the equivalent tilt angle that had the highest performance. As an additional component of sample imaging, eight welds were started and run to varying levels of weld completion with respect to the tool and threaded hole location to highlight when and how forming occurs in the BFSF process. The first imaging sample had the tool edge vertically aligned with the edge of the threaded hole, at which point the weld ended. Subsequent welds terminated an additional 3 mm (0.12 inches) further along the weld path than the previous weld. Image analysis showed the percentage of fill the formed screws had in the threaded holes.

Results

Curved BFSF welds enabled the determination of the ideal equivalent tilt angle and allowed characterizing of strength and forming capabilities. Mechanical testing used four welds at each tilt angle to evaluate tensile strength and shear strength. Weld sample imaging highlights the quality and amount of the infill experienced through the welding process.

Mechanical Testing

Mechanical testing of the samples showed the capabilities of the workpieces in the designated loading configuration. The tensile strength increased from a minimum of 116.6 MPa at a tilt of 0º to a maximum of 159.6 MPa at 9º. The shear strength increased from a minimum of

115.4 MPa at 0º to a maximum of 156.0 MPa at 6º. Table 2 shows the average strength values and associated standard deviations.

Table 2. Tensile testing matrix

Equivalent Tilt Angle	Loading Orientation	Strength [MPa]	Std. Dev. [MPa]
0	Tensile	116.6	25.5
	Shear	115.4	16.1
3	Tensile	135.7	31.0
	Shear	120.5	12.9
6	Tensile	156.0	7.0
	Shear	133.5	13.3
9	Tensile	159.6	4.8
	Shear	126.0	15.0

Tensile strength across all testing parameters increased with an increasing tilt, as shown in Figure 26. Error bars of one standard deviation are higher at the lower equivalent tilt angles than the higher tilts.

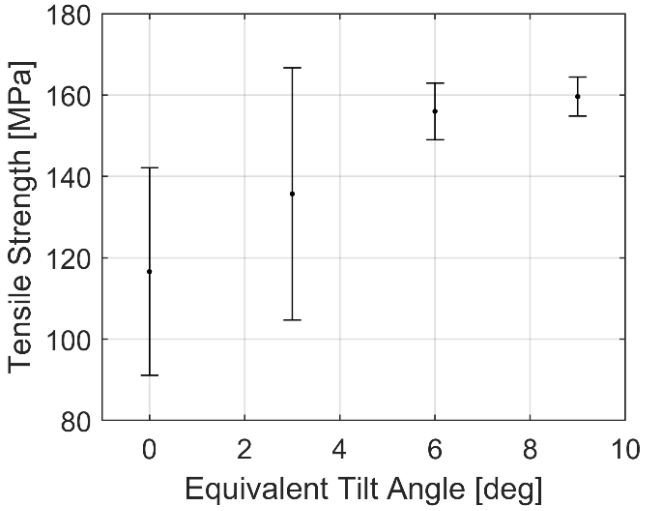

Figure 26. Tensile strength at different equivalent tilt angles. Error bars represent one standard deviation.

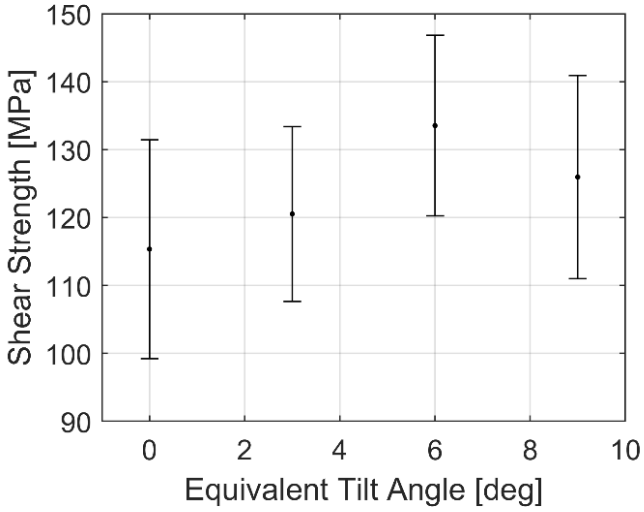

Figure 27. Shear strength at different equivalent tilt angles. Error bars represent one standard deviation.

As the butted aluminum pieces join, they simultaneously form a threaded screw shape. For formed screw evaluation, shear strength testing shows the strength and, therefore, the level of extrusion of the joint. The relationship of shear strength to tilt, shown in Figure 27, shows how the fill varies with respect to the equivalent tilt angle. The shear strength increased up to a tilt of 6º, after which the strength decreased by 5.7% when tested with a 9º tilt. The error bars for the plot are consistently large across all conditions, showing high variability.

Evaluation of In-process Forces

Axial force data, shown in Figure 28, provides insight into the in-process behavior of aluminum forming and associated strengths. The time axis for each plot shifted to align the forming section of the weld for a clearer comparison. The forming period is the time it takes the FSW tool to travel along the weld path one tool radius before the threaded hole to one tool radius after crossing the threaded hole, for a total of 32 mm (1.26 inches). This distance corresponds to about 37 s.

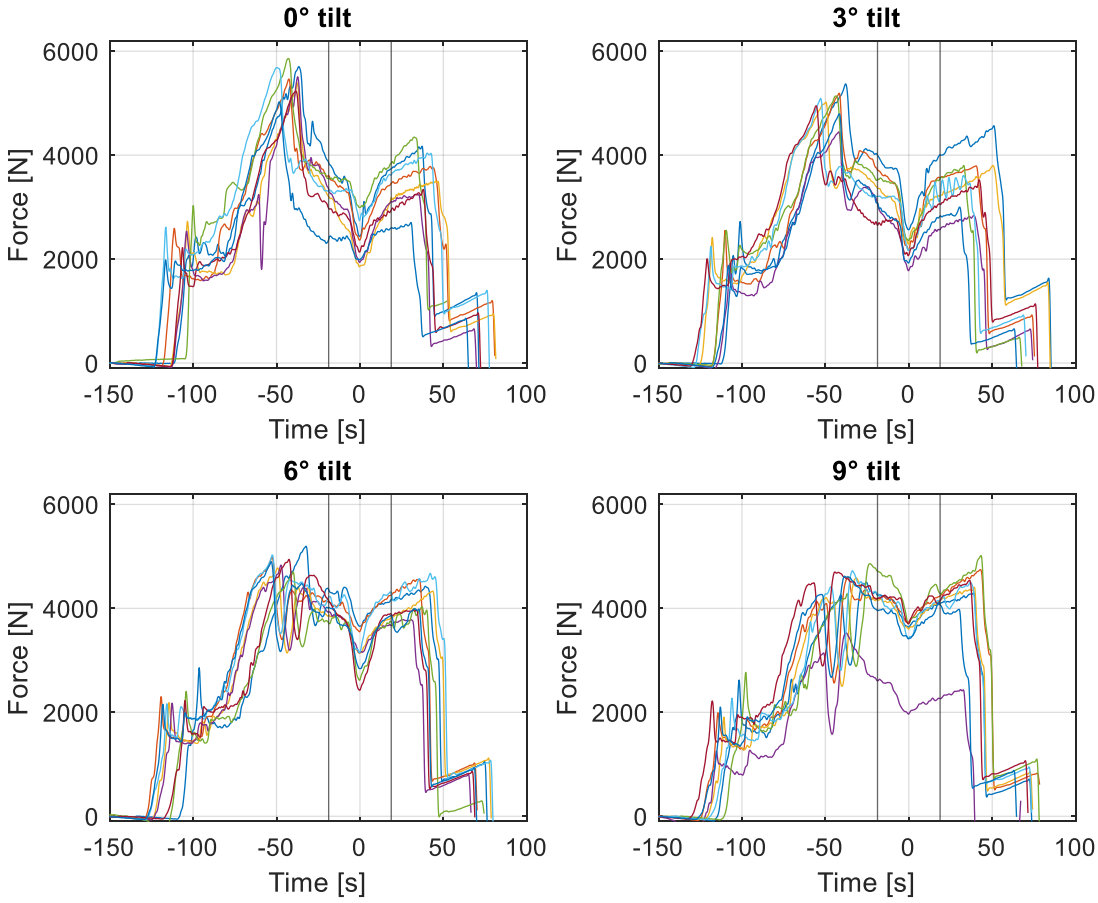

Figure 28. Axial force plots of curved BFSF welds. The time axis shifted to align the forming period of the weld. Vertical black lines denote the forming time starting at t = -18.5 s and ending at t = 18.5 s for a total of 37.0 s. Note: Further analysis excludes the bottommost force trial in the 9º Tilt plot due to incorrectly zeroing the tool's vertical axis, leading to incorrect force measurements.

The forces most relevant in this work are the forces that occur directly before the forming region and the minimum forces experienced due to forming, shown in Figure 29. The forces that occur in the forming region are higher due to the influence of the steel ring backing. When the weld path crosses the threaded hole, there is less reaction force since some material extrudes into the hole. Both the pre-forming forces and the forming forces show an overall upward trend with the tilt angle. The forming dip, the difference between the pre-forming and forming forces,

highlights the welds' forming behaviors. The forming dip is highest at a tilt of 3º and a minimum at 9º.

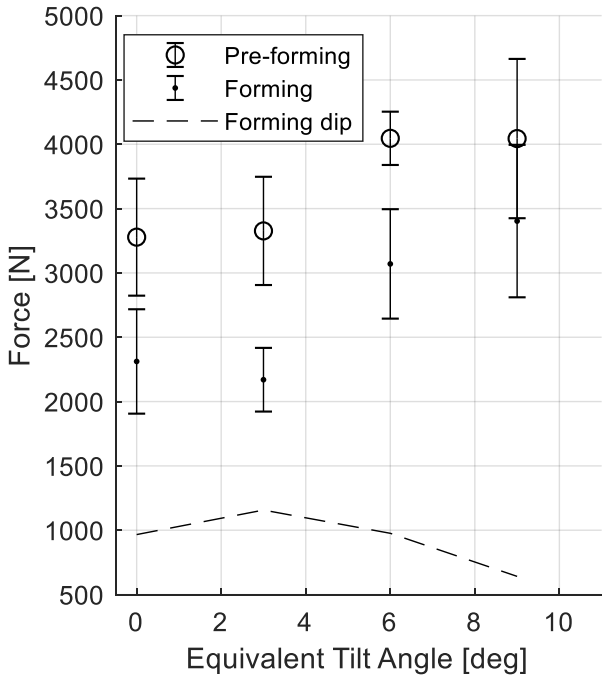

Figure 29. Forces at different equivalent tilt angles during different locations over the weld.

Threaded Hole Fill

The shear strength data showed that a 6º tilt was the strongest, which suggested the best fill. This motivated imaging of this equivalent tilt angle to show how well the aluminum formed inside the threaded hole during the welding process. Figure 30 shows an image of a formed screw with the relative tool motion going from right to left. The formed screw in Figure 30 has a fill of 98.0% comparing the aluminum to the threaded hole. Analyzing images from six different formed screws resulted in an average fill of 98.1%.

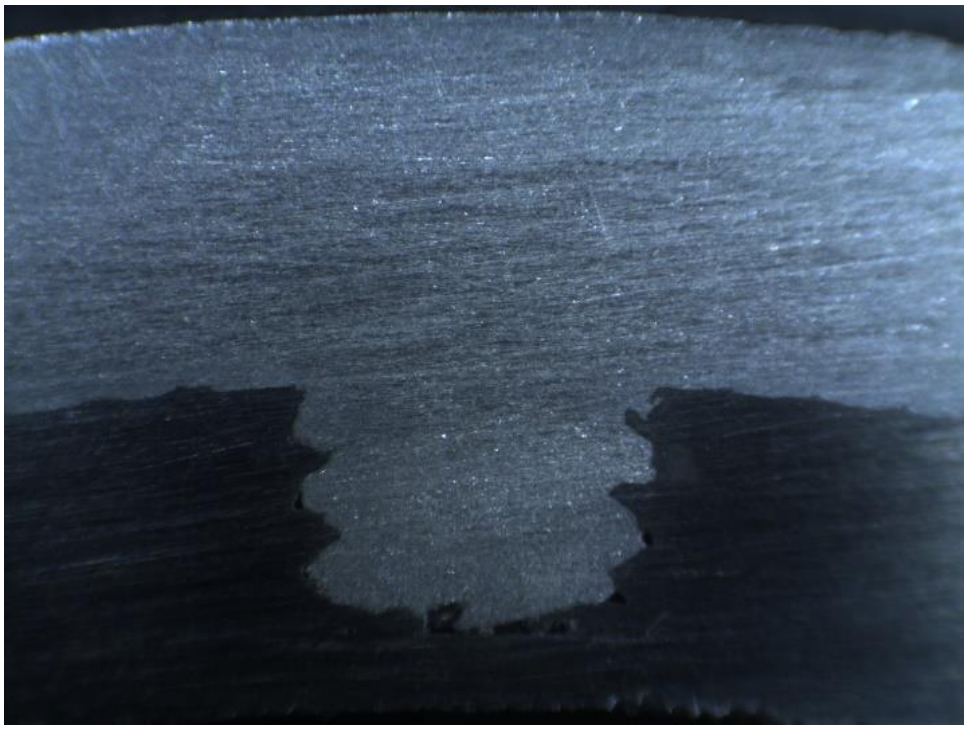

Figure 30. Cross-section of a formed screw at a 6º equivalent tilt angle with relative tool motion going from right to left. The edges of the steel threads deformed due to the high localized forces from the aluminum.

Flow Development

Early-termination weld images of workpiece cross-sections showed how the formed region changed with respect to the tool location. Figure 30 and Figure 31 show extrusion progress at different tool locations. Forming was not observed in the samples until the tool pin had traveled over the centerline of the threaded hole, as shown in Figure 31. The weld sample immediately before the one shown in Figure 31 had no fill, meaning that the entirety of the forming occurred in 3 mm (0.118 inches) of tool travel. At the welding speed used in this work, extruded screw formation took no more than 3.5 seconds between no extrusion and complete extrusion.

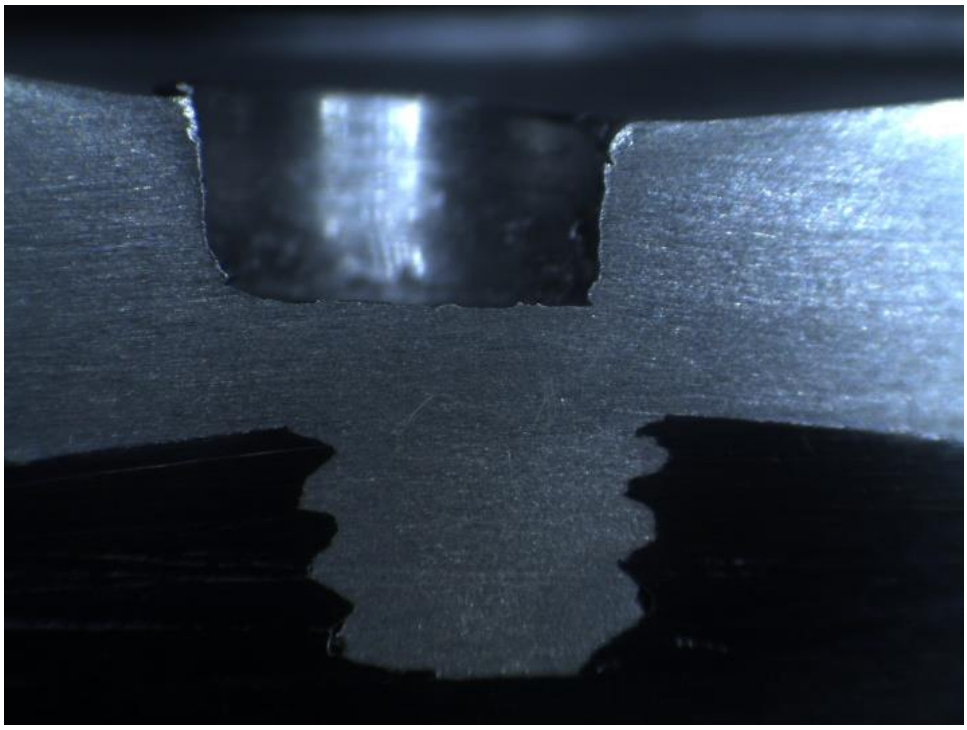

Figure 31. Cross-section of a formed screw at a 6-degree equivalent tilt angle with relative tool motion going from right to left.

Discussion

Tensile strength increased as the tilt angle became more extreme. As the tool angle increases, the tool heel engagement and penetration increase. The improved tool contact increases the forces, as is evident when observing the force plots in Figure 28. Literature shows that weld strength and defect reduction can occur due to relatively higher in-process forces [111]. Tensile strength also positively correlates with tilt angle due to reduced defect formation.

Lower tilt angles produced more surface defects. For the 0º tilt, 7 out of 8 welds had defects. The defects decreased to 4 out of 8 for the 3º tilt and to 1 out of 8 for the 6º tilt. Finally, the 9º tilt had no defects out of 8 trials. All these defects were surface voids at or near the forming location of the threaded hole.

The lower tilts also had higher variability in the measured strength values. The 0º and 3º tilts had coefficients of variability of 21.9% and 22.9%, respectively. The 6º degree and 9º tilts had coefficients of variation of 4.5% and 3.0%, respectively. This reduction is likely due to the increased tool engagement, which steadies the tool as it traverses.

The shear strength of the formed screw follows a different trend than the tensile strength. The shear strength reaches a maximum value at a 6º tilt. Additionally, the variability is high throughout all trials. Shear strengths at lower tilts will have the same variability issues present at the lower tilt tensile strength values. High variability exists in the two higher tilt angles not observed with the higher tilt tensile strength values. This variability likely results from difficulty aligning the aluminum-aluminum faying surface with the threaded hole. For example, a 1 mm tool bias towards either side of the threaded hole corresponds to about 15% of the hole's width. This bias is enough to create the variability shown in this work. Since the tool alignment regarding shear strength has a much greater impact compared to the tensile strength, future tool pathing for curved BFSF should prioritize proper hole alignment over the alignment of the abutting aluminum pieces. FSW butt welding offsets do not need to be as precise as with the threaded holes. Depending on the material, a bias may be advantageous [10].

Tensile and shear strength characteristics are somewhat of a trade-off between a strength reduction in the weld zone due to extrusion and the strength of the extrusion itself. Figure 32 shows the relationship of data measured in this work by normalizing tensile strength and shear strength with their respective maximum values. The figure shows the measured strengths of the samples at different tilts with linear interpolation between the data points as a simple approximation. Between the 6º equivalent tilt angle and the 9º equivalent tilt angle, the tensile strengths and shear strengths switch which one is the highest. With the linear assumption, this plot suggests an optimal equivalent tilt angle of around 7º. However, confirmation of a precise intermediary angle would require further testing and in-depth statistical analysis. Due to the uncertainty of interpolation between the two angles, this analysis only considers the 6º tilt and the 9º tilt. The 6º tilt has the highest normalized shear strength of the measured samples and a tensile strength of 97.7% of the maximum value. Alternatively, the 9º tilt has the maximum normalized tensile strength and 94.3% of the maximum shear strength. The 6º tilt angle has a higher percentage of normalized strength values than the rest of the tilt angles. As such, the 6º equivalent tilt angle was the best-performing configuration in this work.

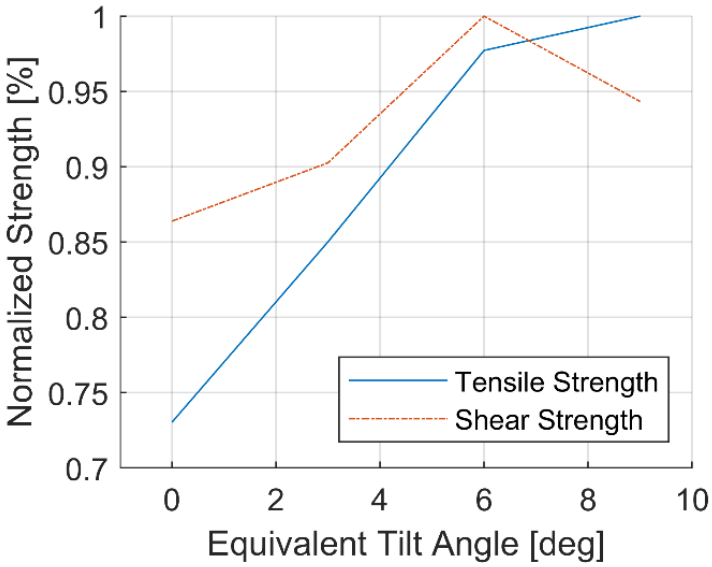

Figure 32. Normalized mechanical strengths at different equivalent tilt angles.

Poor aluminum extrusion into the steel caused the strength to decrease from the 6º tilt to the 9º tilt. The angle is likely too extreme for proper forming. The force data seen in Figure 29 supports this hypothesis. The 9º tilt forming dip force changes are the lowest of all trials. The force decrease due to forming becomes larger when more material is displaced [109]. Since the force dip is lower than in the other trials, the volume of extruded material is not as high.

Conclusions

The curved BFSF process is a viable method to join two pieces of butted aluminum 6061-T6 in a friction stir weld while simultaneously joining with a ring of low-carbon steel. Adding curvature to the BFSF process expanded the literature to include small-radius workpieces. This work validates the process for the proposed aerospace and automotive applications, with additional potential applications in pipe joining.

In experimentation, a method to express the tool offset in a more generalized form for other curvatures expands the applicability of this work. The equivalent tilt angle of 6º was the best-performing configuration in this work. However, it is worth stating that all of the joints that used a non-zero tilt angle produced viable results due to the percentage of strength retained. Depending on the FSW tool geometry, a different configuration may be more advantageous. The

tilt angles used in this work are higher than were used in other curved FSW applications, but the requirement to form the material into the threaded hole required additional forging pressure. The higher-than-normal tilt angle allowed the tool pin and heel to form material as desired.

The advantages of this process include a weight reduction due to the lack of joining flanges, a smoother outer surface for aerodynamics, and an assembly process with fewer operations. This preliminary work with curved BFSF proves the process's efficacy and provides a framework for future work with BFSF.

CHAPTER VI
INVESTIGATION OF FRICTION STIR WELDING FOR LUNAR APPLICATIONS

Connor Strawn, Alvin M. Strauss

This chapter is under review at *Acta Astronautica*.

Abstract

Novel aerospace technology research has been driven by increased interest in governmental and privatized space travel efforts. One such technology is friction stir welding (FSW), often promoted as a capable in-space manufacturing process. FSW literature currently has gaps regarding its operation in lunar conditions. As an initial approximation, this study simulated lunar cooling heat fluxes via a controlled furnace. Regulating the heating and cooling of AA6061-T6 allowed an evaluation of material property changes caused by the lunar cooling rate. Sample analysis utilizing energy dispersive spectroscopy (EDS) showed silicon, magnesium, and iron precipitate growth in the friction stir welds due to simulated lunar cooling. Mechanical testing of the samples showed a minor strength decrease of 6.8% from the ambient condition weld to the simulated lunar cooling weld. The associated in-process torque variations created by heat accumulation suggest reduced energy requirements for FSW compared to terrestrial operation. While a strength decrease was observed, it is minor. The strength and the reduction of in-situ power consumption supports FSW as a valid lunar technology and warrants future work on this subject.

Introduction

Friction stir welding (FSW) is a solid-state joining process developed by The Welding Institute in 1991 [1]. It began as a method to join light metals, such as aluminum, copper, and magnesium, but has since expanded to an extensive list of weldable materials and configurations [6]. Frictional heating and plastic deformation caused by purpose-built FSW tools enable material joining without melting. The elevated temperature does not exceed the material's solidus temperature, so the material remains solid throughout the process. A diagram of the process is shown in Figure 33.

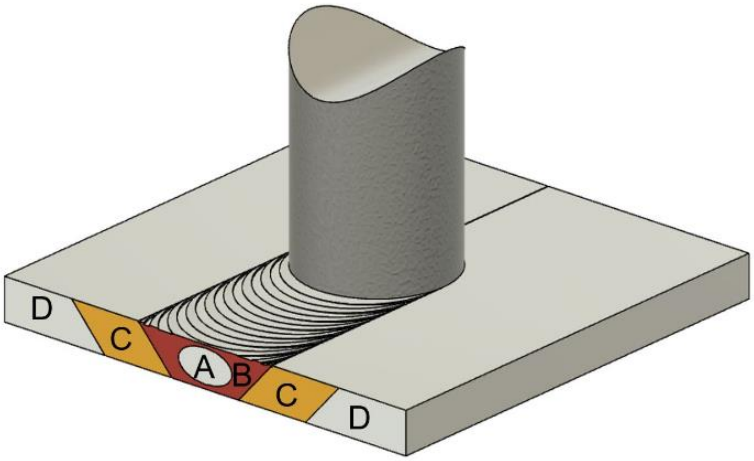

Figure 33. FSW process diagram with process zones highlighted. A: Weld nugget. B: Thermomechanically-affected zone. C: Heat-affected zone. D: Base material.

Notable advantages of FSW in the aerospace sector include joining materials that are more difficult with traditional means. For example, FSW can join aluminum alloys, such as the aluminum-lithium alloys used in the Orion crew module [4,112]. Additionally, there are little-to-no process consumables for FSW [15], eliminating the need for resources that are used in other techniques like fusion welding processes, fasteners, or adhesives. Eliminating the need for consumables also reduces the payload weight for launching FSW tools into space for lunar applications and reduces equipment scarcity concerns.

Proponents of FSW have promoted it as an in-space manufacturing method for years [7]. The in-space capabilities can be extrapolated to operation on the moon. While lunar conditions

are significantly different than Earth's, the simulation of environmental conditions related to FSW is possible through experimentation. The most relevant lunar conditions are the lack of a significant atmosphere, a fraction of Earth's gravity, and harsh thermal conditions. FSW does not require a gaseous environment. It can operate in an oxidizing atmosphere, an inert atmosphere [113], or no atmosphere [114]. The solid-state nature of FSW means that environmental pressure (or lack thereof) does not play a significant role, contrary to fusion welding and brazing that cause melting. Fusion welding without gravity can cause detrimental outcomes such as increased gas entrapment/porosity, molten metal detachment, and electric discharge [19]. Gravity does not limit FSW capabilities as the process works in any spatial orientation with respect to the direction of gravity without changing the efficacy of the process.

Difficulties with lunar FSW arise when considering the thermal effects of both the process and the environment. The moon's atmosphere is so thin as to be considered an exosphere, meaning that any convection via atmospheric gas is negligible. Cooling occurs nearly exclusively through thermal radiation. The heat transfer limitations cause the heat generated through the FSW process to have a lower heat flux leaving the material and consequently taking much longer to cool to the pre-welding temperature. While heat is difficult to quantify in a near-vacuum, the moon's surface temperature is generally between -175 ºC and 115 ºC, depending on exposure to the sun and location [115]. Terrestrial radiation, background cosmic radiation, and internal lunar heat flow have significantly lower heat fluxes than solar radiation [115], so their contribution to FSW heating is considered negligible in this work.

The lunar and FSW temperatures are expected to influence the material properties of the joined structure. Temperature cycling can cause a material to go through several different heat treatment phases, such as annealing and artificial aging, leading to undesired properties for the intended applications. This work is a preliminary experimental study of how FSW would function in a lunar environment.

Material and Methods

Material

Any material property changes due to the lunar environment are material and alloy specific, but testing every potential aerospace alloy is beyond the scope of this study. A general-

purpose aerospace alloy was chosen for this preliminary study: AA6061-T6. This aluminum alloy is prevalent in aerospace construction due to its relatively low weight and decent structural properties [82]. Table 3 shows the material composition. The main alloying components of AA6061 are magnesium, silicon, and iron.

Table 3. AA6061 composition by percent weight [116]

	Si	Fe	Cu	Mn	Mg	Cr	Zn	Ti	Al
AA6061	0.4-0.8	0.70	0.15-0.4	0.15	0.8-1.2	0.35-0.4	0.25	0.15	bal.

FSW Methodology

This FSW research was conducted with a modified milling machine with automated control. A Kistler 9123C piezoelectric dynamometer measured in-process forces and torque, key parameters in process evaluation. The welding apparatus uses an H13 tool steel 25.4 mm diameter tool with a convex, scrolled parabolic shoulder and a threaded profile pin. Welding parameters included a welding speed of 76.2 mm per minute and a rotation speed of 1500 revolutions per minute.

Experimentation results show the effects of material strength after welding in both an ambient condition and with heating to simulate the lunar environment. A tube furnace with ramp/soak control heated samples post-weld to simulate the lunar heat transfer conditions. The furnace enabled temperature tracking of the expected lunar cooling trends. The cooling rates follow calculations and simulations of lunar heat transfer established later in this work.

An FSW joint of two butted AA6061 pieces cooled under ambient conditions as a control sample. The second experimental setup observes the effect of butt welding two pieces together. Immediately after welding, the workpiece is removed from the FSW table and placed in the preheated tube furnace to simulate the reduced heat transfer in a lunar environment. Preliminary experimentation showed that in-process heating is unnecessary as it will not significantly contribute to material property change. Due to FSW's slipping/sticking conditions, the maximum temperature experienced in the weld zone will not differ regardless of the initial material temperature [117].

Testing covers four sets of conditions, including the base material, the base material with heat treatment, an FSW joint, and an FSW joint with heat treatment.

Microscopy

Various heating and cooling conditions will change material properties and appearance through precipitate growth of the alloying elements. From the previous T6 heat treatment, there has been solutionization and some precipitate formation. Further precipitate growth will potentially reduce joint strength due to overaging. Energy dispersive spectroscopy (EDS) with an Oxford EDS and EBSD detector on an FEI FEG Quanta 650 scanning electron microscope (SEM) enabled an evaluation of weld precipitates, including size and location. Data processing produced element maps of the surface that detail particle size and number.

Mechanical Testing

Tensile and hardness data show material performance changes between conditions. For tensile testing, multiple samples from each weld were machined into dog bone test specimens. An Instron load frame with an extension rate of 2 mm per minute determined sample failure load. A Rockwell hardness tester using the Rockwell A (HRA) scale indented additional specimens to show material hardness.

Theory and Calculation

Mathematical Model

An accurate model of the heating of the lunar FSW process is needed to control the secondary heating used in this study, including temperature changes due to the heat inputs and the associated heat fluxes. Since background cosmic radiation is assumed to be negligible, radiation heat fluxes will be from solar irradiance and radiation emission. The total radiation heat flux q''_{rad} can be found with the following equation:

$$q''_{rad} = \alpha_{sol} G_{sol} - \varepsilon \sigma T_s^4 \quad (1)$$

where α_{sol} is the material-dependent absorption coefficient through solar radiation, G_{sol} is the total solar irradiance constant of approximately $1361\ W/m^2$ [118], ε is the material-dependent emissivity, σ is the Stefan-Boltzmann constant of $5.67 * 10^{-8}\ W/m^2K^4$, and T_s is the temperature of the surface. Due to the relatively high thermal conductivity of aluminum alloys

and the use of thin sheets in this work, it is assumed that $T_s \approx T$. The emissivity and absorptivity values used for the material are 0.03 and 0.09, respectively [119].

Determining the heat transfer caused by FSW is difficult since it is a highly coupled physical process. The heat input is dependent on friction and plastic deformation, which is dependent on the temperature of the material. There is a theoretical and empirical maximum achievable temperature due to the slipping effects of the material at high temperatures where friction diminishes. This temperature is approximately 590º C for aluminum alloys [117], near the solidus temperature. Instead of measuring the FSW heat flux directly, calculations use an approximation from the machine energy input calculated from measured torque [120]. Torque is measured directly on the FSW tool spindle, meaning that there are minimal machine losses. The power, *P*, comes from Equation 2.

$$P = \tau\omega \tag{2}$$

The measured torque of the FSW tool is τ, and ω is the rotational speed of the tool spindle. The rotational speed is a process parameter set to a constant in this work. Some of the energy produced flows as heat into the FSW tool. Power losses through the tool ranging from 2% to as high as 25% are possible [60,120,121]. As a conservative estimate, calculations assume that 10% of the power transfers to the tool and 90% transfers to the workpiece.

Knowing the heat fluxes enables the creation of a governing equation for the system. An energy balance expressed as rates is shown in Equation 3 as a foundation for a governing equation.

$$\dot{E_{in}} + \dot{E_g} - \dot{E_{out}} = \dot{E_{st}} \tag{3}$$

$\dot{E_{in}}$ is the total energy transferred into the system, $\dot{E_g}$is the energy generated, $\dot{E_{out}}$ is the energy that leaves the system, and $\dot{E_{st}}$ is the stored energy. Energy sources, E_{in}, are solar radiation and FSW. No internal energy generation occurs. Energy leaves the system through radiation, and $\dot{E_{st}}$ is calculated with Equation 4.

$$Q = mc_p \frac{\partial T}{\partial t} \tag{4}$$

Q is the energy stored, m is the mass of the workpiece, and c_p is the specific heat capacity of the material. Using Equations 1 – 4 and the surface area of the workpiece A_s, an energy balance of the system can be found, as expressed in Equation 5.

$$\frac{\partial T}{\partial t} = \frac{A_s q''_{rad} + 0.9P}{mc_p} \tag{5}$$

To solve this equation numerically, the partial derivative is approximated as $\Delta T/\Delta t$, or the change in temperature over a timestep, t. With this consideration, the equation becomes

$$T = \Delta t \frac{A_s q''_{rad} + 0.9P}{mc_p} + T_i \tag{6}$$

where T is the updated workpiece temperature and T_i is the temperature from the last timestep. The initial temperature used in this study is the calculated maximum temperature that AA6061 will experience from exclusively solar heating. Equation 6 produced a temperature of 245 ºC. This temperature is the starting temperature in further calculations and simulations with ANSYS.

ANSYS Model

A 3D ANSYS model enables an extension of the 1D mathematical model while providing insight into the effects of localized FSW heating. Figure 34 contains the model and associated boundary conditions. The model dimensions are of arbitrary size on the scale of structural members. In the model, two 6.35 mm thick aluminum sheets, each 1.0 m x 0.5 m, are butted together. A moving heat flux model was used to represent the FSW process. The heat input used comes from the measured torque of a sample. Figure 35 shows the temperature distribution at a select frame during FSW.

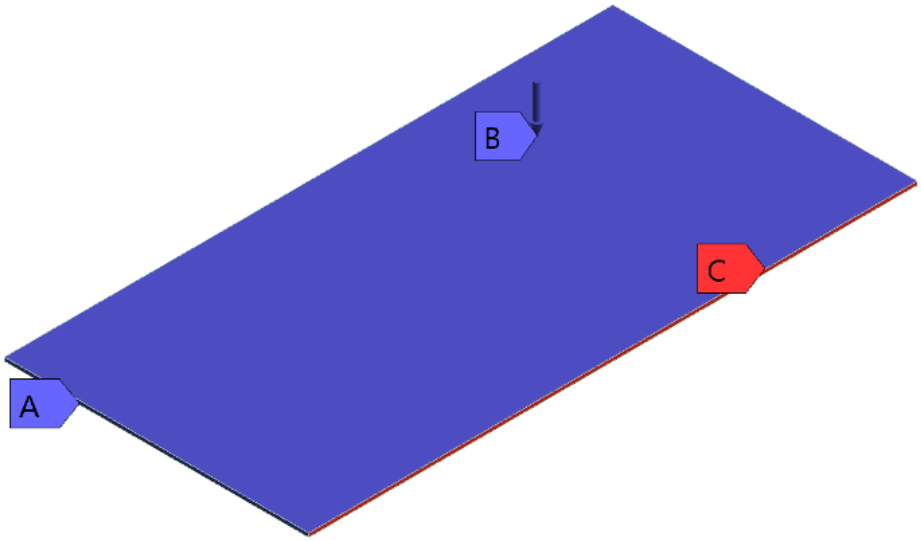

Figure 34. ANSYS model with boundary conditions labelled. A: Insulated sides and bottom. B: Radiation heat flux. C: Symmetry condition.

The mathematical model and exported data from ANSYS enabled the generation of a temperature plot. Figure 36 shows a comparison of various temperature trends. The figure shows a standard AA6061-T6 heat treatment process. The alloy is initially heated to a solution heat treatment temperature for a set time and then quenched. Afterward, it is heated for artificial aging. Artificially aging the material accelerates the formation of precipitates of the alloying constituents [122].

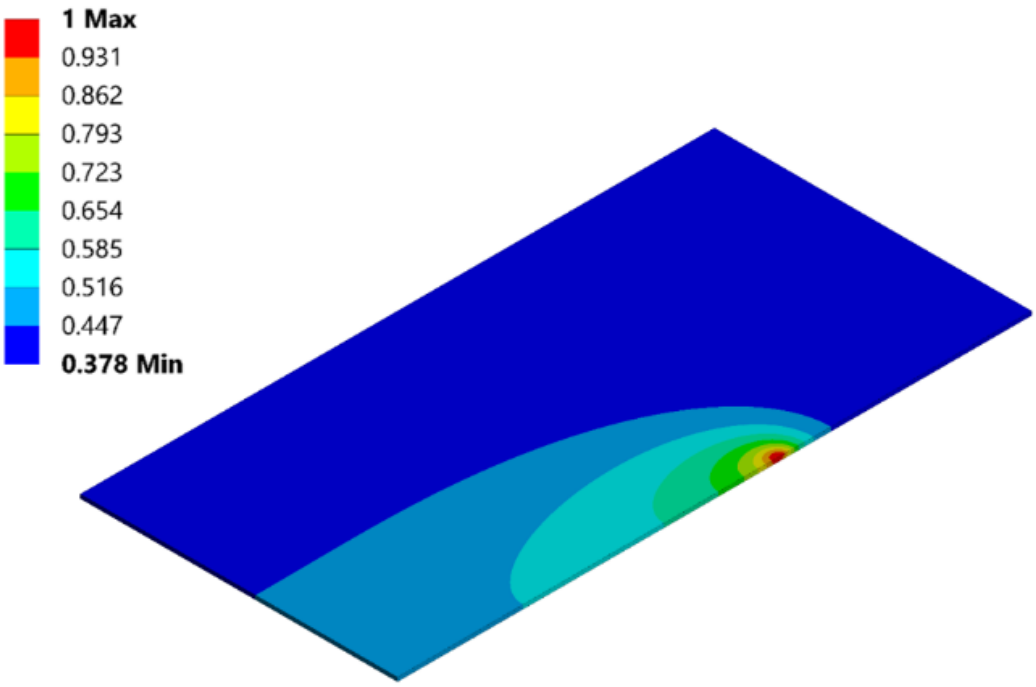

Figure 35. ANSYS FSW weld path temperature map at t = 500 s. Temperature is normalized to its maximum value.

The ANSYS and mathematical models follow a similar trend, which supports the model's validity. Figure 36 shows an initial temperature jump during the first 780 s of the simulation, which is the period that FSW occurs. After one hour in the simulation, the flux of solar irradiance is removed. Long-term exposure to the sun and the accompanying thermal cycling will be detrimental, so the model assumes the application of a cover of some type for shielding. After that point, the only effect on the material is the radiation emission. The temperature trend shown enabled the tuning of a tube furnace for a simulated cooling rate.

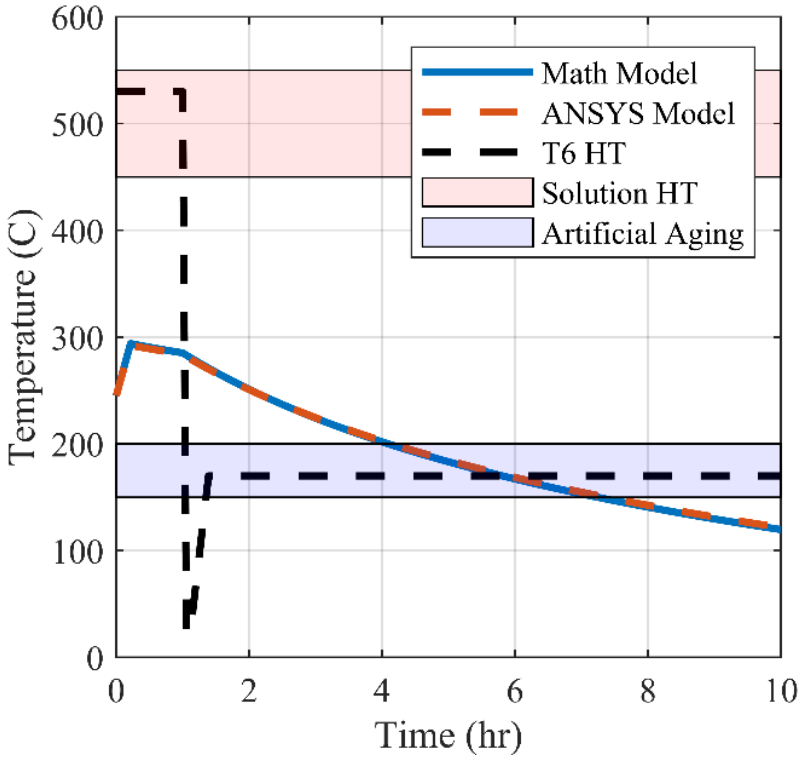

Figure 36. Plot of mathematical model and ANSYS model. For comparison, a typical AA6061-T6 heat treatment process is shown [21, 22].

Results

To properly put the results into context, validation of the workpiece temperature reaching the desired temperature is necessary. Two thermocouples were placed in the workpiece just outside the weld zone to monitor the in-process and post-weld temperatures of a post-weld heat-treated sample. Averaging data from the two thermocouples limited the effects of localized heating. Figure 37 shows a plot of the measured temperature related to the simulated temperatures for a representative sample. The measured temperature of the aluminum initially overshoots the desired temperature, but it is by a relatively small margin of less than 4%. After achieving the desired temperature, the controlled cooling in the tube furnace allowed the sample to follow the trend established in the mathematical and computational models.

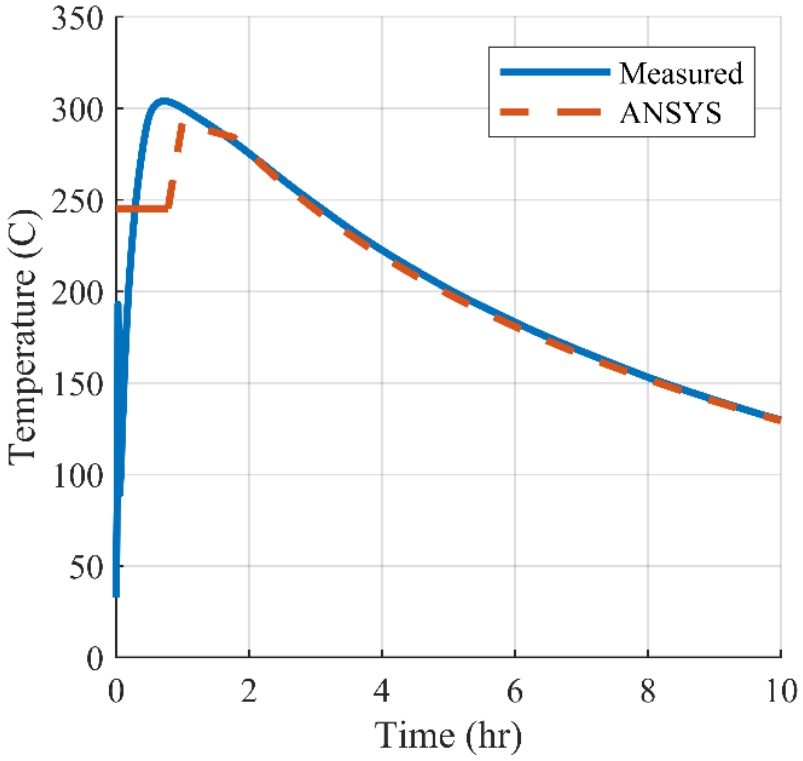

Figure 37. Measured temperature of the post-weld heat-treated sample.

Microscopy

A relatively low magnification of 1000x enabled the identification of large precipitates while getting a general idea of the percent composition of alloying elements. The exact elemental balance and phases cannot be definitively obtained from EDS at this magnitude, as other microscopy methods and magnifications are better suited for that task [124]. However, the EDS method used shows the locations and sizes of precipitates. EDS investigated the alloying elements with the highest weight percent of the alloy: iron, magnesium, and silicon. SEM images and the corresponding EDS maps are shown in Figure 38-Figure 41. Statistics from the EDS maps are presented in Table 4.

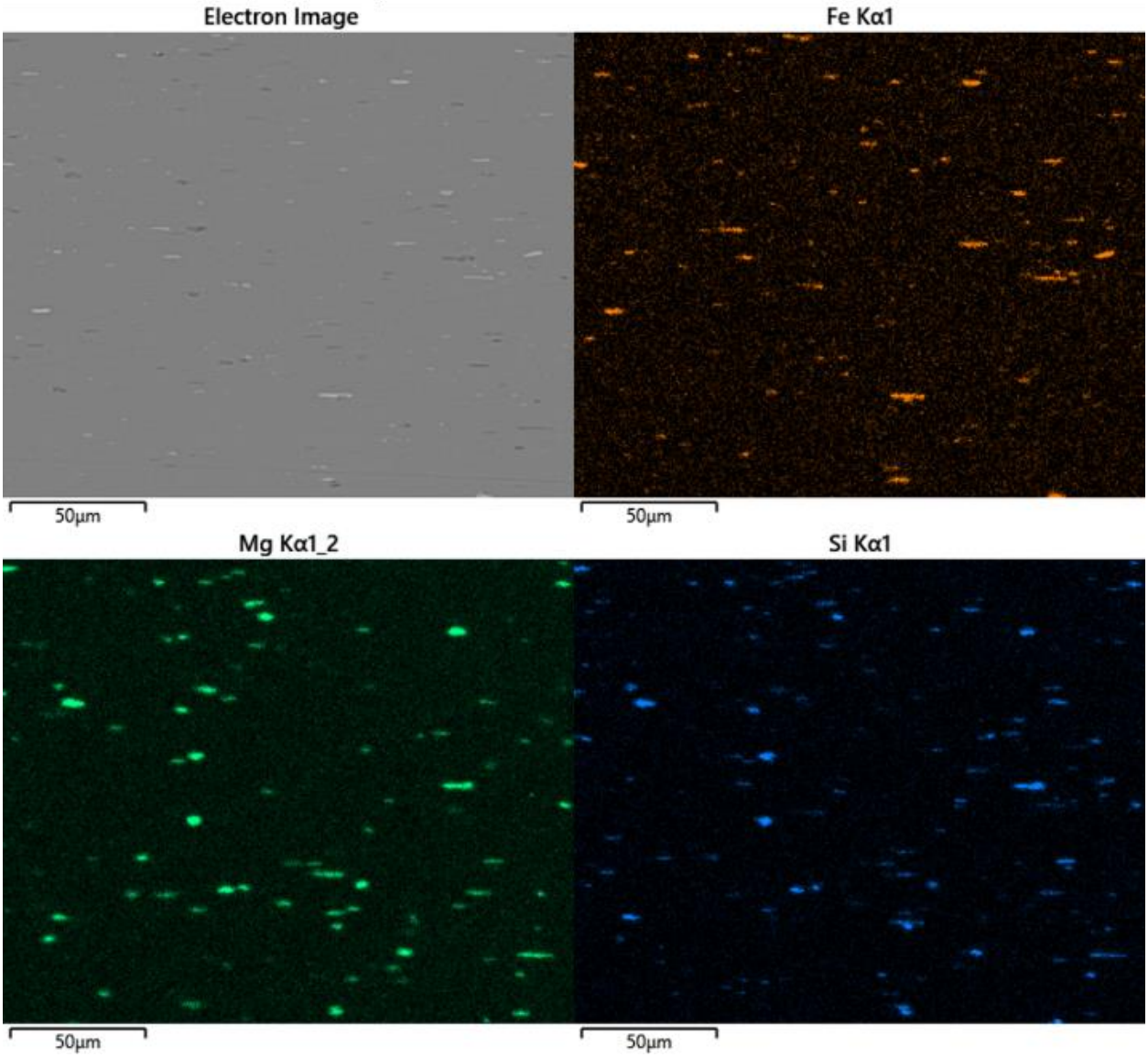

Figure 38. Base material SEM image and EDS maps.

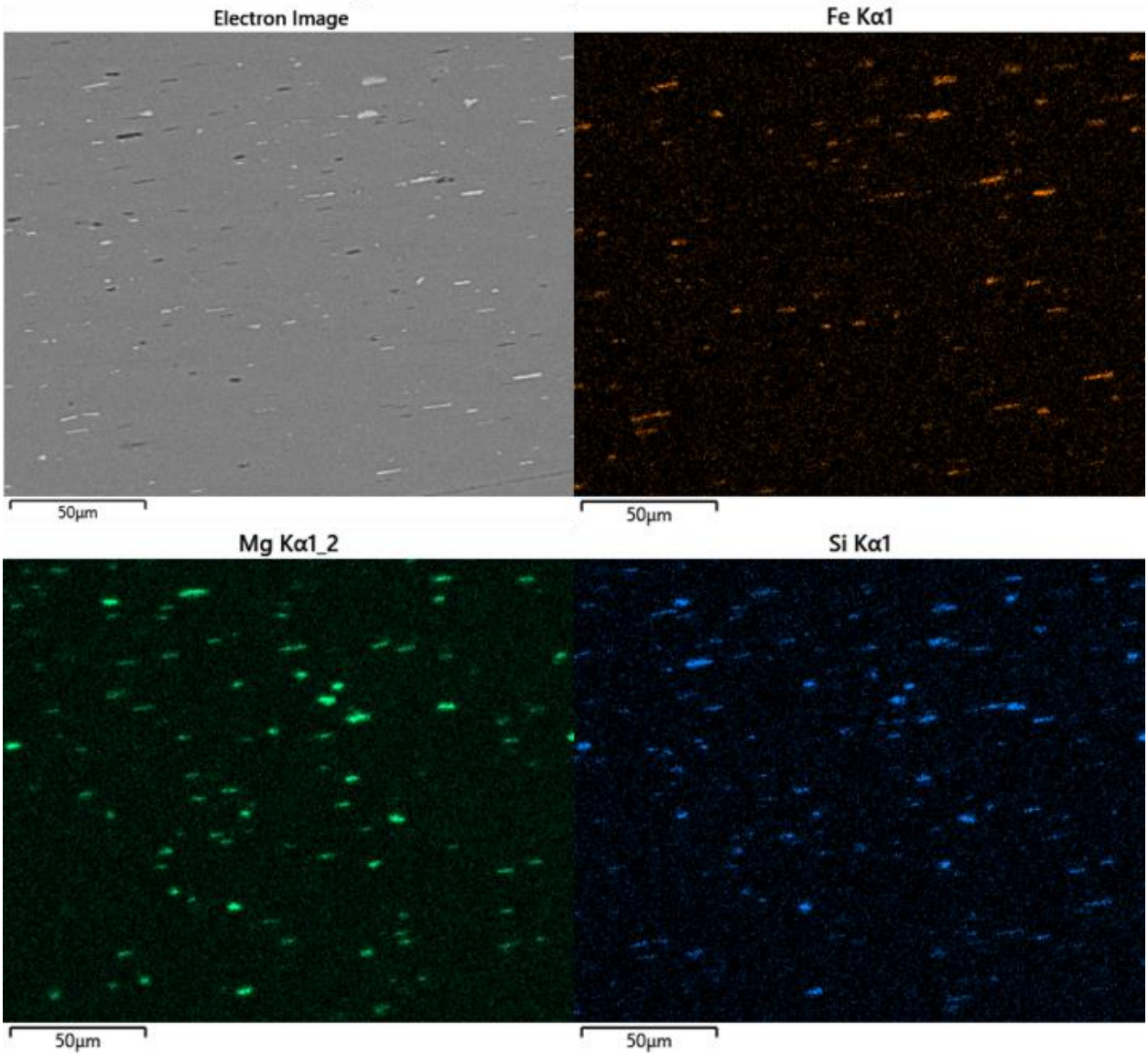

Figure 39. Base material with heat treatment SEM image and EDS maps.

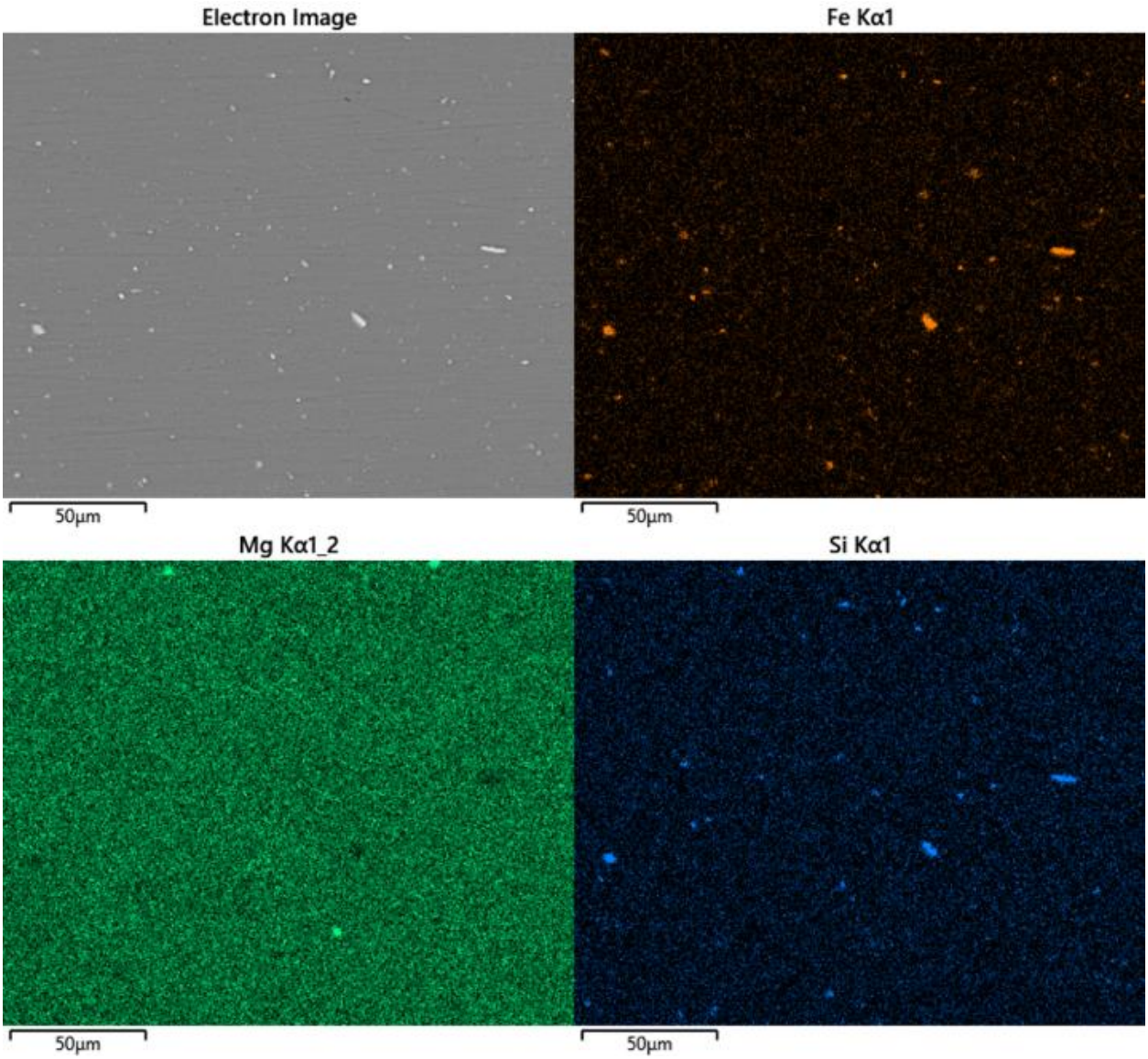

Figure 40. FSW joint in ambient conditions SEM image and EDS maps.

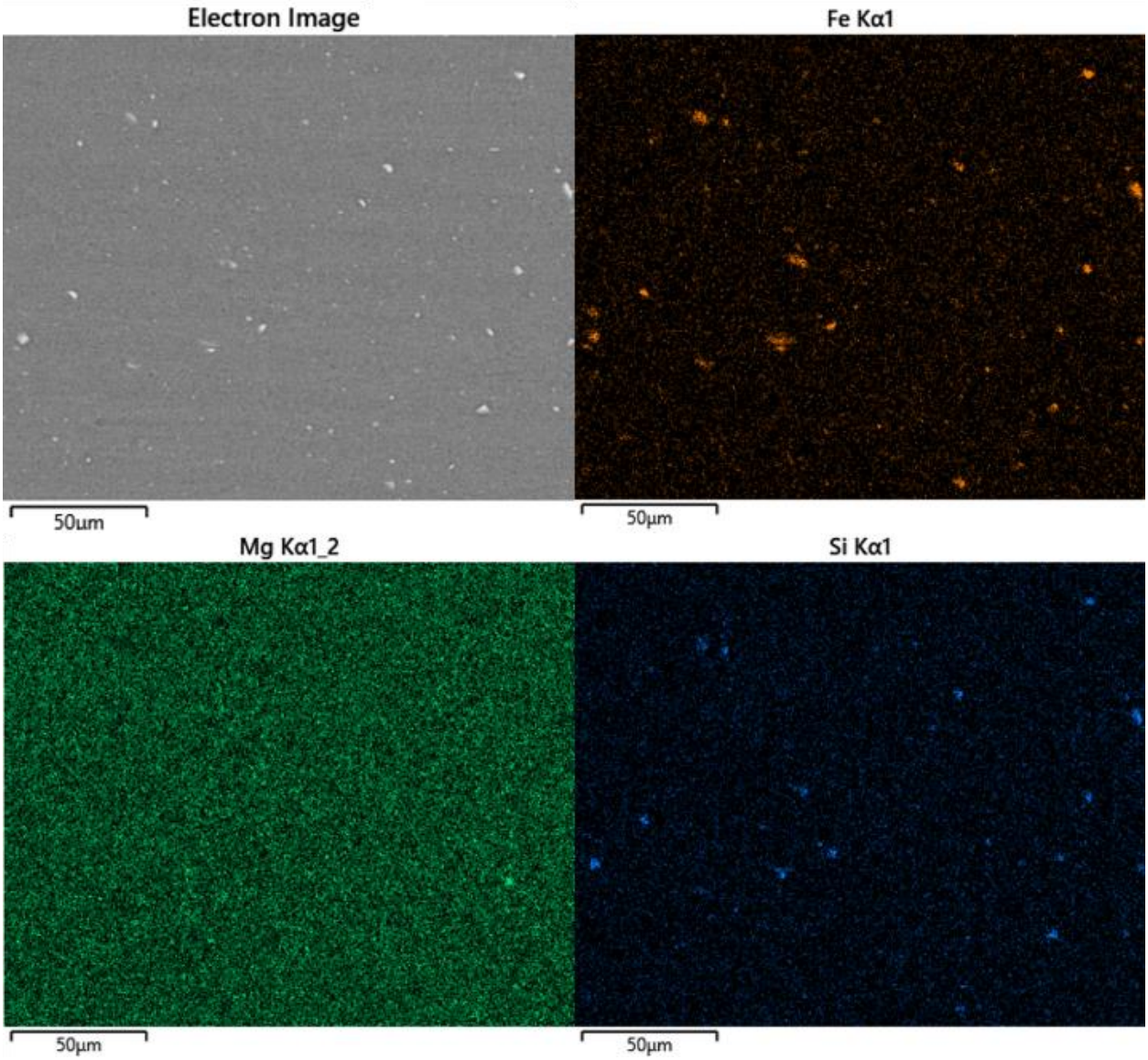

Figure 41. FSW joint with heat treatment SEM image and EDS maps.

Table 4. Precipitate statistics

Sample	Precipitate	Count	Area (μm^2)		
			Min	Max	Average
Base	Fe	345	0.043	17.038	1.893
	Mg_xSi_x	99	0.043	16.099	2.745
Base, HT	Fe	190	0.171	32.283	5.398
	Mg_xSi_x	88	0.171	17.252	3.795
Weld	Fe	722	0.043	23.529	1.217
	Mg_xSi_x	70	0.043	2.690	0.445
Weld, HT	Fe	163	0.171	25.280	3.892
	Mg_xSi_x	70	0.171	2.050	0.495

Mechanical Testing

Samples experienced mechanical testing through tensile and hardness testing. Table 5 presents the mechanical testing data. It is worth noting that the typical AA6061-T6 hardness value is about 40 HRA [123], but the tested base material workpiece only measured 33.6 HRA. Measurements occurred in the center of the cross-section for the non-welded samples and the center of the weld nugget cross-section in the FSW samples.

Table 5. Mechanical testing data

Sample	Strength (MPa)	Strength (%)	Hardness (HRA)	Hardness (%)
Base	285.6	100.0%	33.6	100.0%
Base, HT	164.5	57.6%	10.7	31.7%
Weld	157.3	55.1%	10.1	30.2%
Weld, HT	146.9	51.4%	10.0	29.8%

Each parameter set during tensile testing experienced slightly different failure modes. Within a given set of parameters, the specimens fractured the same way. The base material experienced a ductile fracture. The base material that was heat treated experienced a more extreme ductile failure. Each set of parameters had unique fracture locations. The ambient weld

failed in the heat-affected zone of the weld, while the heat-treated weld failed at the thermomechanically-affected zone/heat-affected zone interface. Figure 42 includes fracture images for each set of parameters.

Figure 42. Select specimen fracture behavior with top and side views. A: Base material. B: Base material with heat treatment. C: FSW joint in ambient conditions. D: FSW joint with heat treatment.

Power Consumption

As was introduced by Equation 2, the torque experienced by the welding tool is directly proportional to the power consumed in the process. For example, Figure 43 shows the in-process torque of one of the welds in this work. The different periods of the welds are highlighted to more clearly observe the torque trends. From 24-72 s, the tool plunge into the material occurs. Torque increases as the tool contact area increases. After the peak torque at 72 s, there is a sharp reduction where the tool dwells at the plunge location to preheat the material. There is a slight increase in torque from 100-135 s due to tool traversing and diminished heating effects from the initial dwell. From 135-195 s, the torque has a downward trend. At that time, the entire workpiece has sufficiently heated. The torque will diminish until it reaches a cyclical steady-state value, which is not seen in this figure but would be present in a longer weld.

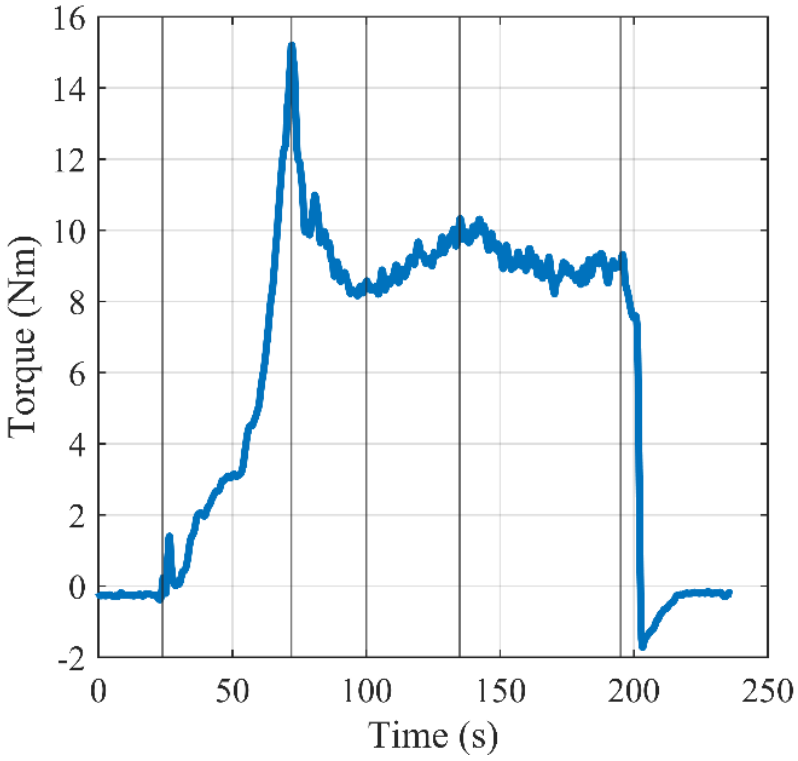

Figure 43. Torque plot for FSW with vertical line designating process phenomena.

Discussion

The EDS maps and associated data show how the precipitating elements change due to FSW and heat treatment. When comparing the base material and the weld under ambient conditions to their heat-treated counterparts, the number of precipitates generally decreases while their sizes increase. The base material went from an average precipitate size of 2.11 μm^2 for 448 precipitates to an average size of 4.89 μm^2 for 278 precipitates. The same trend occurs with the FSW joints, where the average precipitate size for the ambient weld is 1.18 μm^2 for 796 precipitates. The heat-treated weld has an average size of 2.96 μm^2 for 237 precipitates. These values are evidence of precipitate growth due to heat treatment.

The FSW images show a more evenly distributed composition with smaller precipitates than the base material under the same conditions. Figure 40 shows this phenomenon with the magnesium distribution for an ambient condition weld. The magnesium has partially gone back into solution in the aluminum matrix. This image captures the weld nugget, the weld zone that

experiences the most severe plastic deformation in the joint and reaches solutionizing temperatures [122]. The welding temperatures can create a precipitate-free zone [122], but it does not appear that these precipitates completely solutionized.

The precipitates in the weld zone grew from post-weld heat treatment. The average size of precipitates more than doubled through heat treatment, while the number of precipitates decreased by a factor of three. The increase in precipitate size is evidence of dissolution of the alloying elements, a process that weakens the material [122]. The strength change from this treatment was minimal, at only a 3.7% change compared to the base material.

Of the measured strength values, the base material had the highest tensile strength of 285.6 MPa. The heat treatment reduced the strength to 57.6% of the base material. The measured joint efficiency of the FSW joint under ambient conditions was 55.1% of the base material. When heat treatment and welding occur, the strength goes to 51.4% of the base material. The weld strength only diminishes by 6.8% (10.4 MPa) when experiencing the simulated lunar cooling rates. The minimal strength decrease from the simulated lunar cooling rates supports FSW as a capable lunar technology.

The hardness values of the samples fall off significantly from the base material. The heat-treated base material is at only 31.7% of the base material's hardness. The hardness values of the FSW joints without and with heat treatment are comparable in the weld nugget region at 30.2% and 29.8%, respectively, of the base material. The decline in hardness in the base material is due to overaging the T6 temper. Softening in the weld is due to the dissolution of precipitates in the weld zone, a process that makes the material softer and weaker [52]. This zone experienced some precipitate coarsening through post-weld heat treatment, but this did not significantly affect the hardness of the material, as seen in Table 5. This information, with the tensile strength data, suggests that the post-weld heat treatment did not significantly affect the material strength. However, FSW and heat treatment did change the failure behavior.

The different thermal histories of the materials led to varying degrees of ductile fracture. The base material failed with minimal necking and a rough surface finish. The heat-treated base material necked to a small area before fracturing, as seen in Figure 42. This fracture behavior is expected due to the reduced number of precipitates, easing material dislocation. The welded samples fractured in this same way. The FSW joints failed in the heat-affected zone. Literature shows that the welding process coarsens precipitates and grains due to overaging in the heat-

affected zone [125]. Welds under ambient conditions failed in this region, but the heat-treated welds had a slightly different fracture behavior. The heat-treated welds failed at the interface of the thermomechanically-affected zone and the heat-affected zone. More imaging and testing could clarify if this behavior is due to the strengthening of the heat-affected zone or the weakening of the interface between these two zones. It is unlikely that the heat-affected zone had improved strength, as it would only be overaged further. The elongated and un-recrystallized grains present in this zone boundary [15,16] could be susceptible to weakening due to precipitate and grain size changes. Regardless, the minimal failure load differences between the FSW joint and the FSW joint with heat treatment support FSW for a lunar application.

The power consumption, analogous to the torque in Figure 43, decreased due to the increased temperature of the material. The torque experienced in FSW is related to the Young's Modulus of the material, a factor in understanding the physics of this process [126]. Young's Modulus for aluminum decreases with increasing temperature [127], meaning that less power is required to plastically deform the material.

In a vacuum, heat will accumulate at a higher rate. Ueno and Takahashi measured FSW heat accumulation up to 3.5 times as much in a vacuum as compared to ambient conditions [114]. Additionally, heated FSW has about a 20% reduction in forces [128]. The decrease in tool power consumption shown through this work and backed up by literature suggests that FSW would be an efficient process for a lunar application.

Conclusions

Heat treated FSW joints showed a minimal strength reduction of 6.8% compared to the ambient condition weld samples despite the precipitate growth that suggests a significant reduction in strength. Additionally, the reduction in power between terrestrial and lunar FSW suggests that it would be well suited to the moon environment where resource conservation is paramount. FSW furthers the goal of resource conservation by using fewer consumables than a comparable technology.

While the present work formed a proof-of-concept, future work is needed to verify FSW use on the moon, including a more robust experimental setup. Further research on the utilization of lunar and extraterrestrial materials in FSW would improve the validity of this process as well.

While additional experimentation is needed to prove successful application, the microscopy, mechanical testing, and power analysis in this work support FSW as a capable process for lunar application.

CHAPTER VII:
CONCLUSIONS

This dissertation presents unique FSW material combinations, a novel FSW derivative process, and an investigation of lunar FSW. While the main topics covered are distinct, they all contribute to the field of FSW aerospace manufacturing. Each study in this work provided additional examples of novel FSW developments and showed how much room for improvement still exists in the field. Conducting thorough research and extensive experimentation allowed this work to make several contributions to FSW aerospace manufacturing.

Contributions

The research included in this document contributes to several subsets of FSW in the aerospace field, including ablative materials joining, aerospace structures, and extraterrestrial environments. This section highlights how the present work might contribute to FSW aerospace manufacturing.

Joining metal and graphite via FSE introduces a proof of concept for ablative material joining. Experimentation validated the process for low-load applications. This validation is notable due to the difficulty of joining metal to graphite with other methods like brazing or fasteners. Since this work showed process viability and repeatability, the metal-graphite FSE method may expand to operation with other brittle or ablative materials.

The development of BFSF for joining aerospace structures provides a new method to join three workpieces. By minimizing assembly operations and reducing or eliminating the number of fasteners, BFSF is an alternative for attaching exterior surfaces to aerospace structures. This work validated BFSF for flat workpieces and small-radius curved workpieces. Experimental validation showed BFSF joining of three workpieces on an aerospace structure under many curvature configurations.

Additional contributions come from the experimental FSW material property changes in a simulated lunar environment. FSW heat transfer and the lunar environment heat transfer effects showed how they contribute to material strength and ductility. Experimentation showed only a

minor decrease in strength over terrestrial FSW, which supports the process as a potential technology for lunar and in-space operation.

Future Work

A continuation of the FSE graphite project might follow a few different avenues. Validation with newer, advanced ablative materials would extend the impact of ablative material FSE joining. Joint geometry testing with different profiles could provide alternatives to the dovetails tested in this dissertation. Application-based environmental testing would show the technology readiness level of this joining method and potentially lead to further testing of shielding with FSE.

The BFSF process showed promise, but further testing would allow a better evaluation of its capabilities. The most significant next step would be to show that the process provides, at a minimum, comparable joint strengths with competing technologies. Potential testing methods could include fabricating and evaluating a subscale aerospace structure. For example, a small wing could be created with BFSF and tested under different loading configurations. Alternative material characterization and varied testing material configurations would also extend the impact of BFSF.

The main shortcoming of the lunar FSW analysis in this work is that it only partially approximates lunar conditions. For more accurate testing, a vacuum chamber would be necessary. Before performing vacuum testing, preliminary experimentation that applies in-process heating would allow for a better approximation of material properties due to heat buildup in the workpiece. This work used AA6061-T6, but a more realistic material for lunar application would be an aluminum-lithium alloy. Aluminum-lithium alloys currently see use in lunar-intended applications such as the Orion crew module. Understanding how these alloys interact with the thermal effects of lunar welding would be a natural next step.

Expanding the ideas presented in this dissertation would be beneficial, but the most significant future work is continuing to quantify and qualify how FSW applies to aerospace manufacturing. Even if a specific research method does not produce the desired results, it can still inspire new ideas. The proof-of-concept level research in this dissertation intends to catalyze impactful future work.

REFERENCES

[1] W.M. Thomas, E.D. Nicholas, J.C. Needham, M.G. Murch, P. Temple-Smith, C.J. Dawes, Friction welding, US5460317A, 1995. https://doi.org/10.31399/asm.hb.v06.a0001381.

[2] G. Wang, Y. Zhao, Y. Hao, Friction stir welding of high-strength aerospace aluminum alloy and application in rocket tank manufacturing, J. Mater. Sci. Technol. 34 (2018) 73–91. https://doi.org/10.1016/j.jmst.2017.11.041.

[3] W.D.P. Brassington, P.A. Colegrove, Alternative friction stir welding technology for titanium–6Al–4V propellant tanks within the space industry, Sci. Technol. Weld. Join. 22 (2017) 300–318. https://doi.org/10.1080/13621718.2016.1236002.

[4] T. Prater, Friction stir welding of metal matrix composites for use in aerospace structures, Acta Astronaut. (2014) 366–373. https://doi.org/10.1016/j.actaastro.2013.07.023.

[5] B. Christner, J. McCoury, S. Higgins, Development and testing of friction stir welding (FSW) as a joining method for primary aircraft structure, 4th Int. Symp. Frict. Stir Weld. (2003) 1–9.

[6] B.T. Gibson, D.H. Lammlein, T.J. Prater, W.R. Longhurst, C.D. Cox, M.C. Ballun, K.J. Dharmaraj, G.E. Cook, A.M. Strauss, Friction stir welding: Process, automation, and control, J. Manuf. Process. 16 (2014) 56–73. https://doi.org/10.1016/J.JMAPRO.2013.04.002.

[7] W.R. Longhurst, C.D. Cox, B.T. Gibson, G.E. Cook, A.M. Strauss, I.C. Wilbur, B.E. Osborne, Development of friction stir welding technologies for in-space manufacturing, Int. J. Adv. Manuf. Technol. 90 (2016) 81–91. https://doi.org/10.1007/s00170-016-9362-1.

[8] N. Mendes, P. Neto, A. Loureiro, A.P. Moreira, Machines and control systems for friction stir welding: A review, Mater. Des. 90 (2016) 256–265. https://doi.org/10.1016/j.matdes.2015.10.124.

[9] S. Lazarevic, S.F. Miller, J. Li, B.E. Carlson, Experimental analysis of friction stir forming for dissimilar material joining application, J. Manuf. Process. 15 (2013) 616–624. https://doi.org/10.1016/j.jmapro.2013.05.004.

[10] W. Cai, G. Daehn, A. Vivek, J. Li, H. Khan, R.S. Mishra, M. Komarasamy, A state-of-the-art review on solid-state metal joining, J. Manuf. Sci. Eng. Trans. ASME. 141 (2019).

https://doi.org/10.1115/1.4041182.

[11] A.C.F. Silva, D.F.O. Braga, M.A.V. de Figueiredo, P.M.G.P. Moreira, Ultimate tensile strength optimization of different FSW aluminium alloy joints, Int. J. Adv. Manuf. Technol. 79 (2015) 805–814. https://doi.org/10.1007/s00170-015-6871-2.

[12] P.L. Threadgill, Terminology in friction stir welding, Sci. Technol. Weld. Join. 12 (2007) 357–360. https://doi.org/10.1179/174329307X197629.

[13] L. Fratini, G. Buffa, CDRX modelling in friction stir welding of aluminium alloys, Int. J. Mach. Tools Manuf. 45 (2005) 1188–1194. https://doi.org/10.1016/j.ijmachtools.2004.12.001.

[14] M.W. Mahoney, C.G. Rhodes, J.G. Flintoff, R.A. Spurling, W.H. Bingel, Properties of friction-stir-welded 7075 T651 aluminum, Metall. Mater. Trans. A Phys. Metall. Mater. Sci. 29 (1998) 1955–1964. https://doi.org/10.1007/s11661-998-0021-5.

[15] R.S. Mishra, Z.Y. Ma, Friction stir welding and processing, Mater. Sci. Eng. R Reports. 50 (2005) 1–78. https://doi.org/10.1016/j.mser.2005.07.001.

[16] P. Zolghadr, M. Akbari, P. Asadi, Formation of thermo-mechanically affected zone in friction stir welding, Mater. Res. Express. 6 (2019). https://doi.org/10.1088/2053-1591/ab1d25.

[17] M. Kolnes, J. Kübarsepp, F. Sergejev, M. Kolnes, M. Tarraste, M. Viljus, Performance of ceramic-metal composites as potential tool materials for friction stir welding of aluminium, copper and stainless steel, Materials (Basel). 13 (2020). https://doi.org/10.3390/MA13081994.

[18] K. Colligan, Material Flow Behavior during Friction Stir Welding of Aluminum, Weld. J. 65 (1999) 229–237. https://app.aws.org/wj/supplement/july99/COLLIGAN.pdf (accessed September 27, 2019).

[19] T. Prater, Welding in Space: A Comparative Evaluation of Candidate Welding Technologies and Lessons Learned from On-Orbit Experiments, J. Br. Interplanet. Soc. Sp. Chron. 68 (2015). https://www.bis-space.com/eshop/products-page-3/magazines/chronicle/chronicle-2014-2017/space-chronicle-vol-68-supplement-1-2015/ (accessed April 13, 2018).

[20] R. Rai, A. De, H.K.D.H. Bhadeshia, T. DebRoy, Review: Friction stir welding tools, Sci. Technol. Weld. Join. 16 (2011) 325–342.

https://doi.org/10.1179/1362171811Y.0000000023.

[21] H.B. Schmidt, J.H. Hattel, Thermal modelling of friction stir welding, Scr. Mater. 58 (2008) 332–337. https://doi.org/10.1016/j.scriptamat.2007.10.008.

[22] C. Sunnapu, M. Kolli, Tool shoulder and pin geometry's effect on friction stir welding: A study of literature, Mater. Today Proc. 39 (2020) 1565–1569. https://doi.org/10.1016/j.matpr.2020.05.601.

[23] P.C. Lin, J. Pan, T. Pan, Failure modes and fatigue life estimations of spot friction welds in lap-shear specimens of aluminum 6111-T4 sheets. Part 2: Welds made by a flat tool, Int. J. Fatigue. 30 (2008) 90–105. https://doi.org/10.1016/j.ijfatigue.2007.02.017.

[24] K. Krasnowski, C. Hamilton, S. Dymek, Influence of the tool shape and weld configuration on microstructure and mechanical properties of the Al 6082 alloy FSW joints, Arch. Civ. Mech. Eng. 15 (2015) 133–141. https://doi.org/10.1016/j.acme.2014.02.001.

[25] A. Meilinger, I. Torok, the Importance of Friction Stir Welding Tool, Prod. Process. Syst. 6 (2013) 25–34.

[26] R. Kumar, R. Singh, I.P.S. Ahuja, Friction stir welding of ABS-15Al sheets by introducing compatible semi-consumable shoulder-less pin of PA6-50Al, Meas. J. Int. Meas. Confed. 131 (2019) 461–472. https://doi.org/10.1016/j.measurement.2018.09.005.

[27] A.W. Jarrell, J. Cui, A.M. Strauss, G.E. Cook, Friction stir extrusion of thin sheet stock, Manuf. Lett. 24 (2020) 38–42. https://doi.org/10.1016/j.mfglet.2020.03.008.

[28] M.A. Ansari, H. Agiwal, M. Zinn, F. Pfefferkorn, S. Rudraraju, Novel Correlations Between Process Forces and Void Morphology for Effective Detection and Minimization of Voids During Friction Stir Welding, J. Manuf. Sci. Eng. 144 (2022) 1–10. https://doi.org/10.1115/1.4054338.

[29] B. Snyder, A.M. Strauss, In-process cooling of friction stir extruded joints for increased weld performance via compressed air, water, granulated dry ice, and liquid nitrogen, J. Manuf. Process. 68 (2021) 1004–1017. https://doi.org/10.1016/j.jmapro.2021.06.021.

[30] X. Meng, Y. Huang, J. Cao, J. Shen, J.F. dos Santos, Recent progress on control strategies for inherent issues in friction stir welding, Prog. Mater. Sci. 115 (2021) 100706. https://doi.org/10.1016/j.pmatsci.2020.100706.

[31] C.B. Smith, J.F. Hinrichs, W.A. Crusan, Robotic Friction Stir Welding: The State of the

Art, in: 4th Frict. Stir Weld. Int. Symp., 2003.

[32] W.R. Longhurst, A.M. Strauss, G.E. Cook, P.A. Fleming, Torque control of friction stir welding for manufacturing and automation, Int. J. Adv. Manuf. Technol. 51 (2010) 905–913. https://doi.org/10.1007/s00170-010-2678-3.

[33] M. Mehta, K. Chatterjee, A. De, Monitoring torque and traverse force in friction stir welding from input electrical signatures of driving motors, Sci. Technol. Weld. Join. 18 (2013) 191–197. https://doi.org/10.1179/1362171812Y.0000000084.

[34] B. Gibson, G. Cook, T. Prater, W. Longhurst, A.M. Strauss, C.D. Cox, Adaptive torque control of friction stir welding for the purpose of estimating tool wear, in: Proc. Inst. Mech. Eng. Part B J. Eng. Manuf., 2011. https://doi.org/10.1177/2041297510393629.

[35] T. Prater, A. Strauss, G. Cook, B. Gibson, C. Cox, A comparative evaluation of the wear resistance of various tool materials in friction stir welding of metal matrix composites, J. Mater. Eng. Perform. 22 (2013) 1807–1813. https://doi.org/10.1007/s11665-012-0468-9.

[36] P.A. Fleming, C.E. Hendricks, G.E. Cook, D.M. Wilkes, A.M. Strauss, D.H. Lammlein, Seam-tracking for friction stir welded lap joints, J. Mater. Eng. Perform. 19 (2010) 1128–1132. https://doi.org/10.1007/s11665-010-9593-5.

[37] W.J. Arbegast, Friction Stir Conduction Controller, 2001.

[38] J. De Backer, G. Bolmsjö, A.K. Christiansson, Temperature control of robotic friction stir welding using the thermoelectric effect, Int. J. Adv. Manuf. Technol. 70 (2014) 375–383. https://doi.org/10.1007/s00170-013-5279-0.

[39] R. Crawford, G.E. Cook, A.M. Strauss, D.A. Hartman, M.A. Stremler, Experimental defect analysis and force prediction simulation of high weld pitch friction stir welding, Sci. Technol. Weld. Join. 11 (2006) 657–665. https://doi.org/10.1179/174329306X147742.

[40] T.L. Dickerson, J. Przydatek, Fatigue of friction stir welds in aluminium alloys that contain root flaws, Int. J. Fatigue. 25 (2003) 1399–1409. https://doi.org/10.1016/S0142-1123(03)00060-4.

[41] Q. Yang, S. Mironov, Y.S. Sato, K. Okamoto, Material flow during friction stir spot welding, Mater. Sci. Eng. A. 527 (2010) 4389–4398. https://doi.org/10.1016/j.msea.2010.03.082.

[42] X. Lyu, M. Li, X. Li, J. Chen, Double-sided friction stir spot welding of steel and

aluminum alloy sheets, Int. J. Adv. Manuf. Technol. 96 (2018) 2875–2884. https://doi.org/10.1007/s00170-018-1710-x.

[43] H.J. Liu, J.C. Hou, H. Guo, Effect of welding speed on microstructure and mechanical properties of self-reacting friction stir welded 6061-T6 aluminum alloy, Mater. Des. 50 (2013) 872–878. https://doi.org/10.1016/j.matdes.2013.03.105.

[44] L. Trueba, M.A. Torres, L.B. Johannes, D. Rybicki, Process optimization in the self-reacting friction stir welding of aluminum 6061-T6, Int. J. Mater. Form. 11 (2018) 559–570. https://doi.org/10.1007/s12289-017-1365-4.

[45] Z.Y. Ma, Friction stir processing technology: A review, Metall. Mater. Trans. A Phys. Metall. Mater. Sci. 39 A (2008) 642–658. https://doi.org/10.1007/s11661-007-9459-0.

[46] R.S. Mishra, Z.Y. Ma, I. Charit, Friction stir processing: A novel technique for fabrication of surface composite, Mater. Sci. Eng. A. 341 (2003) 307–310. https://doi.org/10.1016/S0921-5093(02)00199-5.

[47] C.S. Jeon, Y.H. Jeong, S.T. Hong, M.T. Hasan, H.N. Tien, S.H. Hur, Y.J. Kwon, Mechanical properties of graphite/aluminum metal matrix composite joints by friction stir spot welding, J. Mech. Sci. Technol. 28 (2014) 499–504. https://doi.org/10.1007/s12206-013-1153-0.

[48] T. Nishihara, Development of friction stir forming, Mater. Sci. Forum. 426–432 (2003) 2971–2978. https://doi.org/10.4028/www.scientific.net/msf.426-432.2971.

[49] W.T. Evans, B.T. Gibson, J.T. Reynolds, A.M. Strauss, G.E. Cook, Friction Stir Extrusion: A new process for joining dissimilar materials, Manuf. Lett. 5 (2015) 25–28. https://doi.org/10.1016/J.MFGLET.2015.07.001.

[50] M. Reza-E-Rabby, K. Ross, N.R. Overman, M.J. Olszta, M. McDonnell, S.A. Whalen, Joining thick section aluminum to steel with suppressed FeAl intermetallic formation via friction stir dovetailing, Scr. Mater. 148 (2018) 63–67. https://doi.org/10.1016/j.scriptamat.2018.01.026.

[51] T. Ohashi, H.M. Tabatabei, T. Nishihara, Cylindrical extrusions on A5083 aluminum alloy plate fabricated by friction stir forming, AIP Conf. Proc. 1896 (2017). https://doi.org/10.1063/1.5008082.

[52] A.W. Jarrell, B.C. Terry, A.M. Strauss, G.E. Cook, Development of an Aging Process for Friction Stir Extruded Joints, J. Manuf. Sci. Eng. Trans. ASME. 143 (2021) 1–8.

https://doi.org/10.1115/1.4048047.

[53] H. Su, C.S. Wu, M. Bachmann, M. Rethmeier, Numerical modeling for the effect of pin profiles on thermal and material flow characteristics in friction stir welding, Mater. Des. 77 (2015) 114–125. https://doi.org/10.1016/j.matdes.2015.04.012.

[54] D. Das, S. Bag, S. Pal, A finite element model for surface and volumetric defects in the FSW process using a coupled Eulerian–Lagrangian approach, Sci. Technol. Weld. Join. 26 (2021) 412–419. https://doi.org/10.1080/13621718.2021.1931760.

[55] H. Aghajani Derazkola, N. Kordani, H. Aghajani Derazkola, Effects of friction stir welding tool tilt angle on properties of Al-Mg-Si alloy T-joint, CIRP J. Manuf. Sci. Technol. 33 (2021) 264–276. https://doi.org/10.1016/j.cirpj.2021.03.015.

[56] M.S. Saidi, M. Rismanian, M. Monjezi, M. Zendehbad, S. Fatehiboroujeni, Comparison between Lagrangian and Eulerian approaches in predicting motion of micron-sized particles in laminar flows, Atmos. Environ. 89 (2014) 199–206. https://doi.org/10.1016/j.atmosenv.2014.01.069.

[57] Z. Zhang, Q. Chen, Comparison of the Eulerian and Lagrangian methods for predicting particle transport in enclosed spaces, Atmos. Environ. 41 (2007) 5236–5248. https://doi.org/10.1016/j.atmosenv.2006.05.086.

[58] B. Meyghani, M. Awang, C.S. Wu, Finite element modeling of friction stir welding (FSW) on a complex curved plate, J. Adv. Join. Process. 1 (2020). https://doi.org/10.1016/j.jajp.2020.100007.

[59] F. Al-Badour, N. Merah, A. Shuaib, A. Bazoune, Coupled Eulerian Lagrangian finite element modeling of friction stir welding processes, J. Mater. Process. Technol. 213 (2013) 1433–1439. https://doi.org/10.1016/j.jmatprotec.2013.02.014.

[60] H. Schmidt, J. Hattel, Modelling heat flow around tool probe in friction stir welding, Sci. Technol. Weld. Join. 10 (2005) 176–186. https://doi.org/10.1179/174329305X36070.

[61] N. Kashaev, V. Ventzke, G. Çam, Prospects of laser beam welding and friction stir welding processes for aluminum airframe structural applications, J. Manuf. Process. 36 (2018) 571–600. https://doi.org/10.1016/j.jmapro.2018.10.005.

[62] M. Rosso, Ceramic and metal matrix composites: Routes and properties, J. Mater. Process. Technol. 175 (2006) 364–375. https://doi.org/10.1016/j.jmatprotec.2005.04.038.

[63] W. Krenkel, F. Berndt, C/C-SiC composites for space applications and advanced friction

systems, Mater. Sci. Eng. A. 412 (2005) 177–181. https://doi.org/10.1016/j.msea.2005.08.204.

[64] A. Pramanik, A.K. Basak, Y. Dong, P.K. Sarker, M.S. Uddin, G. Littlefair, A.R. Dixit, S. Chattopadhyaya, Joining of carbon fibre reinforced polymer (CFRP) composites and aluminium alloys – A review, Compos. Part A Appl. Sci. Manuf. 101 (2017) 1–29. https://doi.org/10.1016/j.compositesa.2017.06.007.

[65] T. Windhorst, G. Blount, Carbon-carbon composites: A summary of recent developments and applications, Mater. Des. 18 (1997) 11–15. https://doi.org/10.1016/S0261-3069(97)00024-1.

[66] J. Wang, Q. Guo, L. Liu, J. Song, The preparation and performance of high-temperature adhesives for graphite bonding, Int. J. Adhes. Adhes. 25 (2005) 495–501. https://doi.org/10.1016/j.ijadhadh.2005.01.006.

[67] I. Fedotov, A. Suchkov, A. Sliva, P. Dzhumaev, I. Kozlov, R. Svetogorov, O. Sevryukov, Simulated thermal tests of a molybdenum/graphite X-ray target manufactured with a novel Ti-Zr-Nb-Be powder filler metal: an investigation of the brazed joint evolution under operating conditions, J. Manuf. Process. 69 (2021) 142–151. https://doi.org/10.1016/j.jmapro.2021.07.035.

[68] A.K. Ray, A. Kar, S.A. Kori, L.C. Pathak, A.N. Sonnad, Graphite-to-304SS braze joining by active metal-brazing technique: Improvement of mechanical properties, J. Mater. Eng. Perform. 22 (2013) 258–266. https://doi.org/10.1007/s11665-012-0225-0.

[69] R. Staffler, G. Kneringer, E. Kny, N. Reheis, Metal/Graphite Composites in Fusion Engineering, IEEE Thirteen. Symp. Fusion Eng. (1989) 955–958.

[70] K. Nagatsuka, Y. Sechi, Y. Miyamoto, K. Nakata, Characteristics of dissimilar laser-brazed joints of isotropic graphite to WC-Co alloy, Mater. Sci. Eng. B Solid-State Mater. Adv. Technol. 177 (2012) 520–523. https://doi.org/10.1016/j.mseb.2011.12.014.

[71] H. Ohmura, T. Yoshida, K. Kawashiri, O. Yoshimoto, Technique for brazing graphite/graphite and stainless steel/high-carbon steel joints, Weld. J. 73 (1994) 2495–2565.

[72] H.E. Pattee, R.M. Evans, R.E. Monroe, Joining Ceramics and Graphite To Other Materials, NASA SP-5052. (1968). www.dtic.mil/cgi-bin/GetTRDoc?AD=ADA306880.

[73] F.L. Tabares, J.M. Perlado, In-service experience feedback of the Tore Supra actively

cooled inner first wall, Fusion Eng. Des. 117 (1995) 123. https://doi.org/10.1016/j.fusengdes.2017.03.038.

[74] W.Y. Yu, S.H. Liu, X.Y. Liu, M.P. Liu, W.G. Shi, Interface reaction in ultrasonic vibration-assisted brazing of aluminum to graphite using Sn-Ag-Ti solder foil, J. Mater. Process. Technol. 221 (2015) 285–290. https://doi.org/10.1016/j.jmatprotec.2015.02.028.

[75] Y. Mao, S. Yu, Y. Zhang, B. Guo, Z. Ma, Q. Deng, Microstructure analysis of graphite/Cu joints brazed with (Cu-50TiH2) + B composite filler, Fusion Eng. Des. 100 (2015) 152–158. https://doi.org/10.1016/j.fusengdes.2015.05.011.

[76] L.O. Lindquist, R. Mah, Graphite-to-Metal Bonding Techniques, Los Alamos Sci. Lab. LA-6928-MS. (1977).

[77] Y. He, J. Yang, H. Shen, L. Wang, Z. Gao, Brazing graphite to hastelloy N superalloy using pure-Au filler metal: Bonding mechanism and joint properties, Mater. Des. 104 (2016) 1–9. https://doi.org/10.1016/j.matdes.2016.04.093.

[78] M. Tashiro, A. Kasahara, Method of bonding graphite to metal, U.S. Patent 5 904 287, 1999. https://patents.google.com/patent/US5904287.

[79] J.C. Han, X.D. He, Oxidation and Ablation of 3D Carbon-Carbon Composite at Up to 3000C, 33 (1995) 473–478.

[80] H.O. Pierson, Molded Graphite: Processing, Properties, and Applications, Handb. Carbon, Graph. Diamonds Fullerenes. (1993) 87–121. https://doi.org/10.1016/b978-0-8155-1339-1.50010-4.

[81] R. Acharya, K.K. Kuo, Effect of pressure and propellant composition on graphite rocket nozzle erosion rate, J. Propuls. Power. 23 (2007) 1242–1254. https://doi.org/10.2514/1.24011.

[82] A.K. Lakshminarayanan, V. Balasubramanian, K. Elangovan, Effect of welding processes on tensile properties of AA6061 aluminium alloy joints, Int. J. Adv. Manuf. Technol. 40 (2009) 286–296. https://doi.org/10.1007/s00170-007-1325-0.

[83] N. Rajesh Jesudoss Hynes, M. Vivek Prabhu, P. Shenbaga Velu, R. Kumar, R. Tharmaraj, M.U. Farooq, C.I. Pruncu, An experimental insight of friction stir welding of dissimilar AA 6061/Mg AZ 31 B joints, Proc. Inst. Mech. Eng. Part B J. Eng. Manuf. (2021). https://doi.org/10.1177/09544054211043474.

[84] M. Reza-E-Rabby, M.J. Olszta, N.R. Overman, M. McDonnell, S.A. Whalen, Friction stir

dovetailing of AA7099 to steel with AA6061 interlayer for reduced Zn embrittlement at dissimilar interface, J. Manuf. Process. 61 (2021) 25–34. https://doi.org/10.1016/j.jmapro.2020.10.084.

[85] D.O. Bokov, M.A. Jawad, W. Suksatan, M.E. Abdullah, A. Świerczyńska, D. Fydrych, H.A. Derazkola, Effect of pin shape on thermal history of aluminum-steel friction stir welded joint: Computational fluid dynamic modeling and validation, Materials (Basel). 14 (2021). https://doi.org/10.3390/ma14247883.

[86] D.G. Mohan, J. Tomków, S. Gopi, Induction Assisted Hybrid Friction Stir Welding of Dissimilar Materials AA5052 Aluminium Alloy and X12Cr13 Stainless Steel, Adv. Mater. Sci. 21 (2021) 17–30. https://doi.org/10.2478/adms-2021-0015.

[87] G. Zhang, W. Su, J. Zhang, Z. Wei, Friction stir brazing: A novel process for fabricating Al/steel layered composite and for dissimilar joining of Al to steel, Metall. Mater. Trans. A Phys. Metall. Mater. Sci. 42 (2011) 2850–2861. https://doi.org/10.1007/s11661-011-0677-0.

[88] J. Joudaki, M. Safari, M. Joodaki, Experimental investigation of friction stir spot welding of polymer-aluminum alloy weldments, Proc. Inst. Mech. Eng. Part B J. Eng. Manuf. (2022). https://doi.org/10.1177/09544054221076241.

[89] R. Conte, J. Buhl, G. Ambrogio, M. Bambach, Joining of aluminum sheet and glass fiber reinforced polymer using extruded pins, AIP Conf. Proc. 1960 (2018). https://doi.org/10.1063/1.5034881.

[90] T. Ohashi, T. Nishihara, H.M. Tabatabaei, Mechanical Joining Utilizing Friction Stir Forming, Mater. Sci. Forum. 1016 (2021) 1058–1064. https://doi.org/10.4028/www.scientific.net/msf.1016.1058.

[91] R. Conte, R. Filosa, V. Formoso, F. Gagliardi, R.G. Agostino, G. Ambrogio, Analysis of extruded pins manufactured by friction stir forming for multi-material joining purposes, AIP Conf. Proc. 2113 (2019) 2–8. https://doi.org/10.1063/1.5112590.

[92] P. Upadhyay, Y. Hovanski, S. Jana, L.S. Fifield, Joining dissimilar materials using friction stir scribe technique, J. Manuf. Sci. Eng. Trans. ASME. 139 (2017) 2016–2018. https://doi.org/10.1115/1.4034629.

[93] C. Strawn, A.M. Strauss, Friction stir extrusion of aluminum AA6061 into isostatically molded graphite, J. Manuf. Process. 69 (2021) 391–397.

https://doi.org/10.1016/j.jmapro.2021.07.052.

[94] P. Cavaliere, R. Nobile, F.W. Panella, A. Squillace, Mechanical and microstructural behaviour of 2024-7075 aluminium alloy sheets joined by friction stir welding, Int. J. Mach. Tools Manuf. 46 (2006) 588–594. https://doi.org/10.1016/j.ijmachtools.2005.07.010.

[95] K. ichiro Mori, Y. Abe, A review on mechanical joining of aluminium and high strength steel sheets by plastic deformation, Int. J. Light. Mater. Manuf. 1 (2018) 1–11. https://doi.org/10.1016/j.ijlmm.2018.02.002.

[96] T. Nishihara, A. Ito, Measurement of die temperature during friction stir forming, Weld. World. 49 (2005) 22–26. https://doi.org/10.1007/BF03266471.

[97] G.K. Padhy, C.S. Wu, S. Gao, Friction stir based welding and processing technologies - processes, parameters, microstructures and applications: A review, J. Mater. Sci. Technol. 34 (2018) 1–38. https://doi.org/10.1016/j.jmst.2017.11.029.

[98] J.S. Leon, V. Jayakumar, Investigation of Mechanical Properties of Aluminium 6061 Alloy Friction Stir Welding, Int. J. Students' Res. Technol. Manag. 2 (2015) 140–144.

[99] A.C. Muñoz, G. Rückert, B. Huneau, X. Sauvage, S. Marya, Comparison of TIG welded and friction stir welded Al-4.5Mg-0.26Sc alloy, J. Mater. Process. Technol. 197 (2008) 337–343. https://doi.org/10.1016/j.jmatprotec.2007.06.035.

[100] D. Bajaj, A.N. Siddiquee, N. Zaman Khan, A.K. Mukhopadhyay, S.M.A. Khan Mohammed, D. Chen, N. Gangil, Flow, process forces and strains during Friction Stir Welding: A comprehensive First principle approach, Proc. Inst. Mech. Eng. Part B J. Eng. Manuf. 235 (2021) 912–924. https://doi.org/10.1177/0954405420970087.

[101] B. Meyghani, M. Awang, A Comparison Between the Flat and the Curved Friction Stir Welding (FSW) Thermomechanical Behaviour, Arch. Comput. Methods Eng. 27 (2020) 563–576. https://doi.org/10.1007/s11831-019-09319-x.

[102] M. Akbari, P. Asadi, Optimization of microstructural and mechanical properties of friction stir welded A356 pipes using Taguchi method, Mater. Res. Express. 6 (2019) 066545. https://doi.org/10.1088/2053-1591/ab0d72.

[103] M.P. Iqbal, R. Jain, S.K. Pal, P. Mandal, Numerical modelling of friction stir welding of pipes: Effect of tool shoulder on mechanical property and metallurgical characterization, J. Manuf. Process. 79 (2022) 326–339. https://doi.org/10.1016/j.jmapro.2022.04.028.

[104] D.H. Lammlein, B.T. Gibson, D.R. Delapp, C. Cox, A.M. Strauss, G.E. Cook, The friction stir welding of small-diameter pipe: An experimental and numerical proof of concept for automation and manufacturing, Proc. Inst. Mech. Eng. Part B J. Eng. Manuf. 226 (2012) 383–398. https://doi.org/10.1177/0954405411402767.

[105] B. Meyghani, M.B. Awang, Prediction of the Temperature Distribution during Friction Stir Welding (Fsw) with A Complex Curved Welding Seam: Application in the Automotive Industry, MATEC Web Conf. 225 (2018) 0–7. https://doi.org/10.1051/matecconf/201822501001.

[106] D.H. Lammlein, D.R. DeLapp, P.A. Fleming, A.M. Strauss, G.E. Cook, The application of shoulderless conical tools in friction stir welding: An experimental and theoretical study, Mater. Des. 30 (2009) 4012–4022. https://doi.org/10.1016/j.matdes.2009.05.023.

[107] Y. Okawa, M. Taniguchi, H. Sugii, Y. Marutani, Development of 5-Axis Friction Stir Welding System, in: 2006 SICE-ICASE Int. Jt. Conf., 2006: pp. 1266–1269.

[108] F.F. Mustafa, A.H. Kadhym, H.H. Yahya, Tool geometries optimization for friction stir welding of AA6061-T6 aluminum alloy T-joint using taguchi method to improve the mechanical behavior, J. Manuf. Sci. Eng. Trans. ASME. 137 (2015) 1–8. https://doi.org/10.1115/1.4029921.

[109] C. Strawn, A.M. Strauss, Butted friction stir forming of AA6061-T6 to low carbon steel, Proc. Inst. Mech. Eng. Part B J. Eng. Manuf. (2022) 1–6. https://doi.org/10.1177/09544054221109085.

[110] D. Franke, M. Zinn, S. Rudraraju, F.E. Pfefferkorn, Influence of Tool Runout on Force Measurement During Internal Void Monitoring for Friction Stir Welding of 6061-T6 Aluminum, J. Manuf. Sci. Eng. Trans. ASME. 143 (2021) 1–12. https://doi.org/10.1115/1.4051009.

[111] K. Kumar, S. V. Kailas, The role of friction stir welding tool on material flow and weld formation, Mater. Sci. Eng. A. 485 (2008) 367–374. https://doi.org/10.1016/j.msea.2007.08.013.

[112] H.S. Lee, J.H. Yoon, J.T. Yoo, K. No, Friction stir welding process of aluminum-lithium alloy 2195, Procedia Eng. 149 (2016) 62–66. https://doi.org/10.1016/j.proeng.2016.06.639.

[113] E.I. Barker, P. Upadhyay, Y. Hovanski, X. Sun, Predicting Lap Shear Strength for Friction

Stir Scribe Joining of Dissimilar Materials, in: Frict. Stir Weld. Process. IX, 2017: pp. 261–267. https://doi.org/10.1007/978-3-319-52383-5_25.

[114] A. Ueno, J. Takahashi, Study of Friction Stir Welding Method in Vacuum Environment, Proc. JSME Annu. Meet. 2005.6 (2005) 323–324. https://doi.org/10.1299/jsmemecjo.2005.6.0_323.

[115] Y. Song, X. Wang, S. Bi, J. Wu, S. Huang, Effects of solar radiation, terrestrial radiation and lunar interior heat flow on surface temperature at the nearside of the Moon: Based on numerical calculation and data analysis, Adv. Sp. Res. 60 (2017) 938–947. https://doi.org/10.1016/j.asr.2017.05.013.

[116] R.B.C. Cayless, Alloy and Temper Designation Systems for Aluminum and Aluminum Alloys, in: ASM Handb., 1990: pp. 15–28. https://doi.org/10.31399/asm.hb.mhde2.a0003122.

[117] D.G. Andrade, C. Leitão, N. Dialami, M. Chiumenti, D.M. Rodrigues, Modelling torque and temperature in friction stir welding of aluminium alloys, Int. J. Mech. Sci. 182 (2020). https://doi.org/10.1016/j.ijmecsci.2020.105725.

[118] G. Kopp, J.L. Lean, A new, lower value of total solar irradiance: Evidence and climate significance, Geophys. Res. Lett. 38 (2011) 1–7. https://doi.org/10.1029/2010GL045777.

[119] F.P. Incropera, D.P. DeWitt, others, Fundamentals of heat and mass transfer, n.d.

[120] Y.J. Chao, X. Qi, W. Tang, Heat transfer in friction stir welding - Experimental and numerical studies, J. Manuf. Sci. Eng. 125 (2003) 138–145. https://doi.org/10.1115/1.1537741.

[121] P.A. Colegrove, H.R. Shercliff, Experimental and numerical analysis of aluminium alloy 7075-T7351 friction stir welds, Sci. Technol. Weld. Join. 8 (2003) 360–368. https://doi.org/10.1179/136217103225005534.

[122] K. Elangovan, V. Balasubramanian, Influences of post-weld heat treatment on tensile properties of friction stir-welded AA6061 aluminum alloy joints, Mater. Charact. 59 (2008) 1168–1177. https://doi.org/10.1016/j.matchar.2007.09.006.

[123] Heat Treating of Aluminum Alloys, in: ASM Handb., 1991: pp. 841–879. https://doi.org/10.1361/asmhba0001205.

[124] D. Maisonnette, M. Suery, D. Nelias, P. Chaudet, T. Epicier, Effects of heat treatments on the microstructure and mechanical properties of a 6061 aluminium alloy, Mater. Sci. Eng.

A. 528 (2011) 2718–2724. https://doi.org/10.1016/j.msea.2010.12.011.

[125] C. Hamilton, M. Kopyściański, A. Węglowska, S. Dymek, A. Pietras, A Numerical Simulation for Dissimilar Aluminum Alloys Joined by Friction Stir Welding, Metall. Mater. Trans. A Phys. Metall. Mater. Sci. 47 (2016) 4519–4529. https://doi.org/10.1007/s11661-016-3617-1.

[126] B. Meyghani, M.B. Awang, S. Emamian, E.T. Akinlabi, A comparison between temperature dependent and constant Young's modulus values in investigating the effect of the process parameters on thermal behaviour during friction stir welding, Materwiss. Werksttech. 49 (2018) 427–434. https://doi.org/10.1002/mawe.201700255.

[127] P.T. Summers, Y. Chen, C.M. Rippe, B. Allen, A.P. Mouritz, S.W. Case, B.Y. Lattimer, Overview of aluminum alloy mechanical properties during and after fires, Fire Sci. Rev. 4 (2015). https://doi.org/10.1186/s40038-015-0007-5.

[128] P.C. Sinclair, W.R. Longhurst, C.D. Cox, D.H. Lammlein, A.M. Strauss, G.E. Cook, Heated Friction Stir Welding: An Experimental and Theoretical Investigation into How Preheating Influences Process Forces, Mater. Manuf. Process. 25 (2010) 1283–1291. https://doi.org/10.1080/10426914.2010.496122.